

ISSN 2074-272X

науково-практичний
журнал

2020/2



EIE електротехніка і **EIE** електромеханіка

Electrical Engineering

& Electromechanics

Електротехніка. Визначні події. Славетні імена

Електричні машини та апарати

Електротехнічні комплекси та системи.

Силова електроніка

Теоретична електротехніка та електрофізика

Техніка сильних електричних та магнітних полів.

Кабельна техніка

Електричні станції, мережі і системи

Ювілеї

З 2015 р. журнал індексується у міжнародній

наукометричній базі Web of Science

Core Collection: Emerging Sources

Citation Index



«ELECTRICAL ENGINEERING & ELECTROMECHANICS»

SCIENTIFIC & PRACTICAL JOURNAL

Journal was founded in 2002

Founders:

National Technical University «Kharkiv Polytechnic Institute» (Kharkiv, Ukraine)

State Institution «Institute of Technical Problems of Magnetism of the NAS of Ukraine» (Kharkiv, Ukraine)

INTERNATIONAL EDITORIAL BOARD

Klymenko B.V.	Editor-in-Chief , Professor, National Technical University "Kharkiv Polytechnic Institute" (NTU "KhPI"), Ukraine
Sokol Ye.I.	Deputy Editor , Professor, Corresponding member of NAS of Ukraine, Rector of NTU "KhPI", Ukraine
Rozov V.Yu.	Deputy Editor , Professor, Corresponding member of NAS of Ukraine, Director of State Institution "Institute of Technical Problems of Magnetism of the NAS of Ukraine"(SI "ITPM NASU"), Kharkiv, Ukraine
Batygin Yu.V.	Professor, Kharkiv National Automobile and Highway University, Ukraine
Bíró O.	Professor, Institute for Fundamentals and Theory in Electrical Engineering, Graz, Austria
Bolyukh V.F.	Professor, NTU "KhPI", Ukraine
Colak I.	Professor, Nisantasi University, Istanbul, Turkey
Doležel I.	Professor, University of West Bohemia, Pilsen, Czech Republic
Féliachi M.	Professor, Technological Institute of Saint-Nazaire, University of Nantes, France
Gurevich V.I.	Ph.D., Honorable Professor, Central Electrical Laboratory of Israel Electric Corporation, Haifa, Israel
Ida N.	Professor, The University of Akron, Ohio, USA
Kildishev A.V.	Associate Research Professor, Purdue University, USA
Kuznetsov B.I.	Professor, SI "ITPM NASU", Ukraine
Kyrylenko O.V.	Professor, Member of NAS of Ukraine, Institute of Electrodynamics of NAS of Ukraine (IED of NASU), Kyiv, Ukraine
Nacke B.	Professor, Gottfried Wilhelm Leibniz Universität, Institute of Electrotechnology, Hannover, Germany
Podoltsev A.D.	Professor, IED of NASU, Kyiv, Ukraine
Rainin V.E.	Professor, Moscow Power Engineering Institute, Russia
Rezynkina M.M.	Professor, NTU "KhPI", Ukraine
Shkolnik A.A.	Ph.D., Central Electrical Laboratory of Israel Electric Corporation, member of CIGRE (SC A2 - Transformers), Haifa, Israel
Trichet D.	Professor, Institut de Recherche en Energie Electrique de Nantes Atlantique, Nantes, France
Yatchev I.	Professor, Technical University of Sofia, Sofia, Bulgaria
Yuferov V.B.	Professor, National Science Center "Kharkiv Institute of Physics and Technology", Ukraine
Zagirnyak M.V.	Professor, Member of NAES of Ukraine, rector of Kremenchuk M.Ostrohradskiy National University, Ukraine
Zgraja J.	Professor, Institute of Applied Computer Science, Lodz University of Technology, Poland

ISSUE 2 / 2020

TABLE OF CONTENTS

Electrical Engineering. Great Events. Famous Names

Baranov M.I. An anthology of the distinguished achievements in science and technique. Part 53: Nobel Prize Laureates in Physics for 2016-2019.....	3
---	---

Electrical Machines and Apparatus

Milykh V.I., Shilkova L.V. Characteristics of a cylindrical inductor of a rotating magnetic field for technological purposes when it is powered from the mains at a given voltage	13
Prakht V.A., Dmitrievskii V.A., Kazakbaev V.M., Oshurbekov S.Kh. Comparative analysis of two high-speed single-phase electrical machines with permanent magnets on the stator	20

Electrotechnical Complexes and Systems. Power Electronics

Kuznetsov B.I., Nikitina T.B., Bovdui I.V., Petrov S.V., Kolomiets V.V., Kobilyanskiy B.B. Active shielding of magnetic field with circular space-time characteristic	26
--	----

Theoretical Electrical Engineering and Electrophysics

Baranov M.I., Rudakov S.V. Calculation-experimental determination of the average number of quantized longitudinal electron de Broglie half waves in a cylindrical conductor with pulsed axial current	33
Tolmachev S.T., Il'chenko A.V. The reciprocity principle for a nonlinear anisotropic medium without hysteresis: theory and practice of application.....	40

High Electric and Magnetic Field Engineering. Cable Engineering

Batygin Yu.V., Chaplygin E.A., Shinderuk S.A. Experimental investigation of the current distribution on the sheet blank surface in linear tools of magnetic-pulsed attraction	46
Bezprozvannykh G.V., Kostiuikov I.A. A method of wavelet analysis of time series of parameters of dielectric absorption of electrical insulating structures	52
Palchykov O.O. Determination of the effective permittivity of a heterogeneous material	59

Power Stations, Grids and Systems

Romashko V.Ya., Batrak L.M., Abakumova O.O. Regulatory characteristics of the step-down switching regulator which charges the battery from the solar battery	64
Regad M., Helaimi M., Taleb R., Gabbar H., Othman A. Optimal frequency control in microgrid system using fractional order PID controller using Krill Herd algorithm.....	68

Editorial office address: Dept. of Electrical Apparatus, NTU «KhPI», Kyrpychova Str., 2, Kharkiv, 61002, Ukraine
phones: +380 57 7076281, +380 67 3594696, **e-mail:** a.m.grechko@gmail.com (**Grechko O.M.**)

ISSN (print) 2074-272X
ISSN (online) 2309-3404

© National Technical University «Kharkiv Polytechnic Institute», 2020

© State Institution «Institute of Technical Problems of Magnetism of the NAS of Ukraine», 2020

Printed 16 April 2020. Format 60 x 90 1/8. Paper – offset. Laser printing. Edition 200 copies.

Printed by Printing house «Madrid Ltd» (18, Gudanova Str., Kharkiv, 61024, Ukraine)

M.I. Baranov

AN ANTHOLOGY OF THE DISTINGUISHED ACHIEVEMENTS IN SCIENCE AND TECHNIQUE. PART 53: NOBEL PRIZE LAUREATES IN PHYSICS FOR 2016-2019

Purpose. Brief presentation of the distinguished achievements of Nobel Prize Laureates in physics for current time period of 2016-2019. Methodology. Scientific methods of collection, analysis and analytical treatment of scientific and technical information of world level in area of astronomy, astrophysics, physicists of the condensed environments, laser physics, modern theoretical and experimental physics. Results. The brief analytical review of the scientific discovery and distinguished achievements of scientists-physicists in area of modern physical and technical problems which were marked the Nobel Prizes in physics for the period 2016-2019 is presented. In the number of such discovery and achievements of the best representatives of world scientific association entered: theoretical discovery of topology phase transitions and topology phases of matter, experimental discovery of gravity waves, revolutionary inventions in area of laser physics, astronomic discovery and contribution to our understanding of evolution of Universe and place of Earth in space. Originality. Systematization and analytical exposition is executed in short concentrated and accessible to the wide reader to the form of the known scientific and technical materials, awarded with the Nobel Prizes in physics for current time period of 2016-2019 and devoted to: the theoretical openings of topology phase transitions and topology phases of matter, experimental opening of gravity waves, revolutionary inventions in area of laser physics, astronomic discovery and contribution to our understanding of evolution of Universe and place of Earth in space. Practical value. Popularization and deepening of scientific and technical knowledge for students, engineer and technical specialists and research workers in area of astronomy, astrophysics, physicists of the condensed environments, laser physics, modern theoretical and experimental physics, extending their scientific range of interests and further development of scientific and technical progress in human society. References 22, figures 14.

Key words: Nobel prize on physics, distinguished scientific and technical achievements, theoretical discovery of topology phase transitions and topology phases of matter, experimental discovery of gravity waves, revolutionary inventions in area of laser physics, astronomic discovery and contribution to our understanding of evolution of Universe and place of Earth in space.

Наведено короткий аналітичний огляд видатних науково-технічних досягнень вчених, які відмічені Нобелівською премією по фізиці за період 2016-2019 рр. У число таких досягнень представників світової наукової спільноти увійшли: теоретичні відкриття топологічних фазових переходів і топологічних фаз матерії, експериментальне відкриття гравітаційних хвиль, революційні винаходи в галузі лазерної фізики, астрономічні відкриття і внесок в наше розуміння еволюції Всесвіту і місця Землі в космосі. Бібл. 22, рис. 14.

Ключові слова: Нобелівська премія по фізиці, видатні науково-технічні досягнення, теоретичні відкриття топологічних фазових переходів і топологічних фаз матерії, експериментальне відкриття гравітаційних хвиль, революційні винаходи в галузі лазерної фізики, астрономічні відкриття і внесок в наше розуміння еволюції Всесвіту і місця Землі в космосі.

Приведен краткий аналитический обзор выдающихся научно-технических достижений ученых, отмеченных Нобелевской премией по физике за период 2016-2019 гг. В число таких достижений представителей мирового научного сообщества вошли: теоретические открытия топологических фазовых переходов и топологических фаз материи, экспериментальное открытие гравитационных волн, революционные изобретения в области лазерной физики, астрономические открытия и вклад в наше понимание эволюции Вселенной и места Земли в космосе. Библ. 22, рис. 14.

Ключевые слова: Нобелевская премия по физике, выдающиеся научно-технические достижения, теоретические открытия топологических фазовых переходов и топологических фаз материи, экспериментальное открытие гравитационных волн, революционные изобретения в области лазерной физики, астрономические открытия и вклад в наше понимание эволюции Вселенной и места Земли в космосе.

Introduction. As it is well known, the Nobel Prize in physics is awarded once a year by the Royal Swedish Academy of Sciences. This is one of the five Nobel Prizes (in the field of physics, chemistry, physiology, literature and the establishment of peace between peoples), which appeared in the scientific world by will (this fact was documented in 1895 [1]) by the famous Swedish engineer and inventor of chemical explosives Alfred Nobel (1833-1896), which has been awarded since 1901 to living physicists for their outstanding scientific and technical achievements [2] «tested» by time [2]. We point out that in monetary terms, this prestigious international award for

its more than a hundred years period underwent changes due to the financial condition of the Nobel Foundation and in 2017 amounted to 9 million Swedish kronor (about USD 1.12 million) [3]. The official ceremony of presenting this valuable award according to the established tradition takes place on December 10 of each year (on the day of A. Nobel's death) in the Swedish capital of Stockholm and the King of Sweden is solemnly awarded the prize to its laureates with no more than three people (the Nobel Prize on peace is an exception to this tradition, the ceremony of delivery of which is held

annually in the capital of Norway the city of Oslo at the above time).

Earlier, the author in [2, 4-8] described the main outstanding achievements in science and technology of Nobel Prize winners in physics for the modern time period 1990-2015. We try below to present briefly similar scientific and technological achievements of world physicists in recent years, limited by the time period of 2016-2019.

The goal of the paper is a summary of the outstanding achievements in science and technology of Nobel Prize winners in physics for the modern time period, covering 2016-2019.

1. Nobel Prize in physics for 2016. The Laureates of this prestigious prize for 2016 were American-British theoretical physicists *John Michael Kosterlitz* (born on June 22, 1943, Fig. 1) and *David James Thouless* (born on September 21, 1934, Fig. 2) and *Frederick Duncan Michael Haldane* (born on September 14, 1951, Fig. 3), working in the USA [1]. The Nobel Prize to these physicists was not awarded for one specific scientific discovery, but for a whole list of pioneering scientific works that during the period 1970-1980 stimulated the development of a new direction in condensed matter physics [1]. It should be noted that the corresponding decision of the Nobel Committee it is indicated that this Prize was awarded to M. Kosterlitz, D. Thouless and D. Haldane «... for the theoretical discoveries of topological phase transitions and topological phases of matter» [1].



Fig. 1. Outstanding American-British theoretical physicist John Michael Kosterlitz (born in 1943), Laureate of Nobel Prize in Physics for 2016 [1]



Fig. 2. Outstanding American-British theoretical physicist David James Thouless (born in 1934), Laureate of Nobel Prize in Physics for 2016 [1]

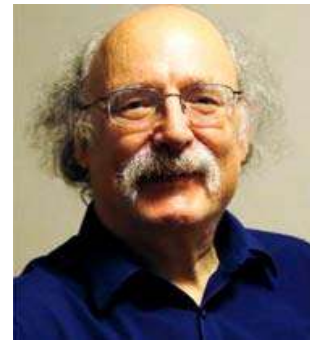


Fig. 3. Outstanding American-British theoretical physicist Frederick Duncan Michael Haldane (born in 1951), Laureate of Nobel Prize in Physics for 2016 [1]

In earthly nature, it so happened that condensed matter physics turned out to be the richest section of physics for various phenomena. For clarity of the complex scientific material presented below, we answer, first of all, the simple question: what is understood in physics as a condensed medium? A *condensed medium* is a set of particles of the same type of substance that come together and strongly affect each other [9]. To condense (comes from the Latin word «condensare» – «to condense» [10]) a substance means to turn it from a gaseous state into a liquid or solid crystalline one. Therefore, a rarefied gas is not a condensed medium. In a condensed medium, a wealth of physical phenomena arises spontaneously dynamically as a result of *collective effects* [1]. In this regard, the properties of a condensed medium are determined by the synchronous *collective movement* of its enormous number of particles, and not its individual particles. It turns out that in the medium under consideration of these collective movements there is a huge variety of these of these *collective movements*.

In the works of the foreign theoretical physicists mentioned above, it was found that a condensed medium can «speak» not only the «language» of *synchronous collective movements* of its particles, but also the «language» of *topologically nontrivial excitations* [1]. For the reader, this physical concept requires its explanation. The term «*topology*» comes from the Greek words «*topos*» – «*place*» and «*logos*» – «*word*» [10]. In this regard, topology, as a branch of mathematics, studies the general properties of geometric figures that do not change during any continuous transformations of these figures [10]. It follows from such a branch of mathematics as geometry that if one geometric figure can be reduced by smooth deformation to another, then such two figures are considered topologically equivalent. If two geometric figures are not transformed into each other by any smooth changes, then such figures are considered topologically different. Next, we dwell on the term «*excitation*». In condensed matter physics, *excitation* is any collective deviation from the «dead» stationary state of the medium and its particles, that is, from the state with the least energy [1]. The oscillating excitation of the crystalline structure of a substance, characterized by the presence of sound waves (phonons) in it, can be caused by both external causes (e.g., mechanical shock to the crystal) and

internal spontaneous causes (e.g., the presence of a nonzero temperature in the crystal). The usual thermal tremor of the crystal lattice of matter, which is widely known to us from the course of atomic physics, is due to the mutual overlapping of oscillating excitations (phonons) with different wavelengths [9]. In the case when the concentration of phonons in the crystal is high, a phase transition occurs in it and the crystal melts. From this we can conclude that as soon as theoretical physicists begin to understand in terms of what excitations one or another condensed medium should be described, they get the scientific «key» to its thermodynamic and other physical properties in their hands.

It is known that by controlling the amplitude of sound oscillations (phonons), one can smoothly change the strength (energy) of these vibrations: from their maximum to their minimum (zero). Therefore, phonons are *topologically trivial excitations* of matter. Just as the world around us is diverse, so are its condensed media. In some such media, there are excitations that cannot be smoothly reduced to zero. Moreover, it is not physically impossible, but fundamentally impossible (their form does not allow). In them, the excitations in their form are topologically different from the above phonons. In this case, there is no smooth operation that would translate a physical system (medium) with excitation into a similar system with the lowest energy. The properties of such physical media change stepwise. It was topology that allowed physicists to describe the properties of matter, which change stepwise.

A group of American theoretical physicists composed of M. Kosterlitz, D. Thouless and D. Haldane, who are British by origin, using topological methods of mathematics as a scientific tool, succeeded in the course of their many years of theoretical research in the period 1970-1980 to obtain a mathematical description of stepwise changing parameters in condensed matter [1]. They showed that in condensed systems such as two-dimensional superconductors, phase transitions are very specific and are really associated with topological features (excitations) – vortices that are generated by «vortex – antivortex» pairs [1]. These physicists have developed advanced mathematical methods to describe the unusual phases and properties of matter. For example, for such widely known materials as superconductors, superfluid liquids, and magnetic films. For objectivity in this complex and important scientific issue, it should be noted that in 1971 the Soviet theoretical physicist Vadim Berezinsky (1935-1980), who worked at the L.D. Landau Institute of Theoretical Physics of the Academy of Sciences of the USSE, for the first time in the world, put forward the idea that phase transitions in thin layers of superconductors and superfluid (quantum) liquids are based on topological excitations – vortices that spontaneously arise in matter in the form of coupled pairs «vortex – antivortex» (by the way, this a scientific idea formed the basis of his PhD Thesis) [1]. At the finite temperature of the substance, such pairs can be produced during a smooth local infrastructural change. It is they

(these vortex pairs) that destroy in the two-dimensional case the crystalline phase of matter at low temperatures. Therefore, it is not for nothing that this phase transition in a condensed medium began to be called the «Berezinsky-Kosterlitz-Thouless» phase transition [11]. In this regard, in the Nobel Prize considered there is also a certain Russian «trace». We also point out that the most important works of the Soviet physicist V. Berezinsky relate to the theory of phase transitions in two-dimensional systems and the theory of localization in disordered one-dimensional conductors. It was he who first theoretically showed that a thin (of the order of several Angstroms) film of liquid helium at low temperatures has the property of superfluidity [1].

In 1972, M. Kosterlitz and D. Thouless (a year later than our V. Berezinsky), realizing the important role of topological excitations, came to a similar conclusion about the determining effect of coupled «vortex – antivortex» pairs in phase transitions in matter [11]. They went further and found that as the temperature of a substance increases, so many coupled «vortex – antivortex» pairs accumulate in it that individual pairs become *untwisted*. In this case, in a condensed medium, the physical picture changes dramatically and its thermodynamic characteristics undergo stepwise changes: a phase transition occurs in the medium due to unraveling of topological excitations [1]. In a press release of the Nobel Committee in connection with the award of the indicated group of physicists of the corresponding Prize for 2016, it was said [12]: «... *Scientists have opened the door to an unknown world where matter can take on «strange states». They used advanced mathematical methods to study unusual phases or states of matter. The work of scientists can be further used in science and electronics.* They refuted the theories of superconductivity and superfluidity of matter that existed at that time, which argued that these phenomena can only occur in thin layers of matter. These physicists theoretically showed that in a substance the phenomenon of superconductivity can occur exclusively at low temperatures. They gave an accurate explanation of this physical mechanism based on phase transitions and found that this phenomenon disappears due to these transitions at higher temperatures [11]. Note that today the topological description of phase transitions in matter is used not only in the case of a thin layer, but also for ordinary three-dimensional materials. Further development of this field of physics led to the creation and study of a new class of substances – topological insulators that are popular today [11]. Over the past decade, this area of physics has been expanded by numerous studies aimed at finding unusual phases of matter. Now many researchers around the world are creating new topological materials that can be used in superconductors, new-generation electronics, and quantum computers [1, 11].

2. Nobel Prize in physics for 2017. The 2017 Nobel Laureates in Physics were distinguished experimental physicists who worked fruitfully in the United States,

Rainer Weiss (born on September 29, 1932, Fig. 4), Barry Clark Barish (born on January 27, 1936, Fig. 5) and Kip Stephen Thorne (born on June 1, 1940, Fig. 6) «... for the decisive contribution to the creation of the LIGO detector and the registration of gravitational waves» [13].



Fig. 4. Outstanding American experimental physicist Rainer Weiss (born in 1932), Laureate of Nobel Prize in Physics for 2017 [13]

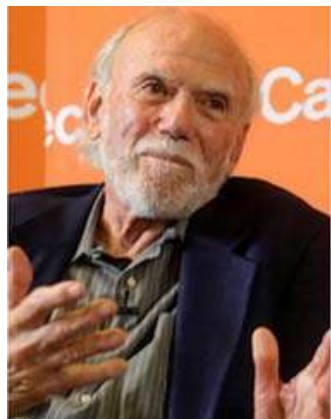


Fig. 5. Outstanding American experimental physicist Barry Clark Barish (born in 1936), Laureate of Nobel Prize in Physics for 2017 [13]



Fig. 6. Outstanding American experimental physicist Kip Stephen Thorne (born in 1940), Laureate of Nobel Prize in Physics for 2017 [13]

American scientists R. Weiss (Professor of physics at the Massachusetts Institute of Technology), as well as B. Barish and K. Thorne (Professor of physics at the

California Institute of Technology), who worked in the well-known scientific collaboration LIGO (Laser Interferometric Gravitational Observatory), on September 14, 2015 for the first time the world, using laser interferometers, discovered cosmic perturbations of «space-time» (gravitational waves) from the merger of a pair of «black holes» in our Universe [14].

To date, four signals (gravitational waves) have been recorded in observatories of the world from the confluence of «black holes» in the outer space surrounding planet Earth or the explosion of other massive objects [14, 15]. The last discovery of LIGO (USA) was made in conjunction with the European observatory VIRGO. The existence of gravitational waves is one of the predictions of the general theory of relativity (GTR). Their discovery confirms not only GTR itself, but is also considered one of the proofs of the existence of «black holes» in space [14].

The above complex physical concepts require their explanation. To begin with, we point out that gravitational waves are oscillations of the space-time geometric structure propagating in «space-time» that move at the speed of light [14]. Their existence was predicted more than a hundred years ago in GTR, developed in 1915 by the outstanding German theoretical physicist Albert Einstein (1879-1955 [16]). To this should be added that the idea that the curvature of space can move in the form of a wave was first expressed by the famous English mathematician William Clifford (1845-1879) in 1876, i.e. almost 39 years before the creation by A. Einstein of GTR [14]. An interesting circumstance is that at the beginning of the 20th century, after A. Einstein developed the special theory of relativity (STR) in 1905, some well-known scientists (including the prominent French mathematician and mechanic Henri Poincaré, 1854-1912 [16]) tried to include also gravity to STR. Note that A. Poincaré at one time interpreted gravity waves as waves moving in space similarly to electromagnetic waves [17]. However, only in 1915, A. Einstein in the framework of GTR was able to give a generally covariant description of gravity as a geometric effect. In such a way actually the modern theory of gravity was born. Nevertheless, the situation with the physical reality of gravitational waves in the scientific world still remained ambiguous. Here, scientific disputes revolved around the fundamental question: do gravitational waves even transfer energy or not? If they transfer it, then physicists have a chance to study them experimentally. If not, then they (gravitational waves) become a «thing in themselves» that is inaccessible to us for a physical experiment. For many years, a convincing answer to the above question in physical science did not exist. The final confirmation of the tangibility of gravitational waves came to modern physics only in the 1970s, when it became clear that a cosmic pulsar of the PSR B1913+16 type loses its energy due to gravitational radiation exactly as A. Einstein's GTR predicts by this physical phenomenon [17].

The LIGO laser-interferometric gravitational-wave observatory (USA), which now employs more than a

thousand employees, recorded a gravitational wave for the second time in February 2016, which came to us from vast space [18]. The Nobel Committee would not award a Prize for only one such event, set by the LIGO detector in September 2015 [14]. When this gravitational wave (oscillations of «space-time») reached planet Earth, it was barely perceptible. In order to «reach» the Earth, this wave took more than a billion years [18]. The energy of the gravitational wave at its origin is huge, but its amplitude is incredibly small. To register it, physicists needed fundamentally new supersensitive instruments – detectors of gravitational waves diverging in space from their origin at the speed of light in all directions. The place of their origin is, for example, distant cosmic places where very massive objects collide with each other – «black holes» [14, 15]. Far, far beyond the boundaries of our Milky Way galaxy, two «black holes» once crashed into each other and after 1.3 billion years the LIGO gravitational-wave observatory, located in the United States (Fig. 7), recorded this space event. The creation of these gravitational wave detectors required the work of thousands of people and the resources of 20 countries, first implemented in the USA in LIGO laser interferometers. To evaluate the scientific problems facing foreign experimental physicists and compare them with earthly problems that we understand, we note that in order to register a gravitational wave, scientists needed to achieve a sensitivity of their laser interferometers that was equivalent to the sensitivity of an instrument capable of measuring the distance to a distant star accurate to tenths of a millimeter [18].

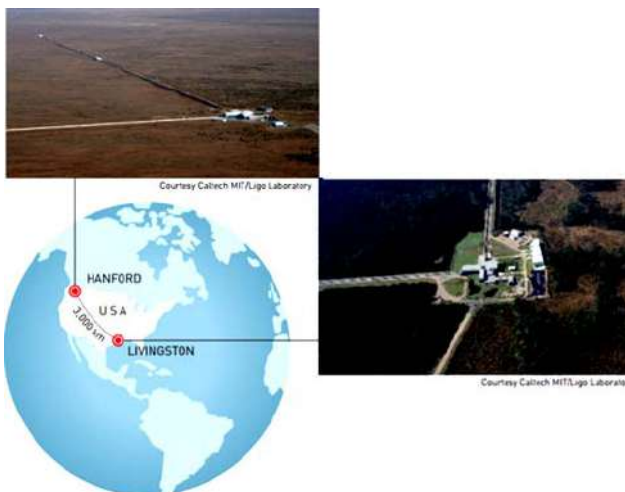


Fig. 7. Layout and general views of two American LIGO gravitational observatories in Livingston (Louisiana, USA) and in Hanford (Washington, USA) located at a distance of 3002 km from each other [18]

The reader may have simple questions: why do we even need earthlings and why spend huge sums of money on recording space disasters of the distant past? The answer may be adequate: for people to understand the world in which humanity exists. In the 1970s, R. Weiss developed the concept of creating the LIGO detector in the USA, which would include two gravitational-wave

observatories that are distant from each other at a distance of about 3002 km [18]. In it, he took into account those earthly phenomena that can distort the process of registration of a gravitational wave. In addition, he suggested ways to eliminate them and influence on the process of measuring this very weak wave amplitude. In a LIGO detector, a gravitational wave travels the distance between its two laser interferometers in 7 ms. Therefore, in this huge supersensitive device, two laser interferometers can refine each other's readings. B. Barish joined the LIGO team, with only 40 employees at that time, in 1994 and turned it over time into the huge international collaboration LIGO-VIRGO (the last one is the recently created European gravitational-wave observatory). Thanks to the coordinated work of the participants of this scientific collaboration, a fundamental breakthrough in the physical registration of gravitational waves and understanding of gravity became possible [18]. K. Thorne, as a leading world expert in the field of the theory of relativity, performed the theoretical calculations necessary for the operation of the LIGO detector [18]. It is interesting to note that the fourth gravitational wave recently detected by the LIGO detector was not the result of the merging of «black holes» in space, but the result of the explosion of a neutron star [18]. The studies conducted by R. Weiss, B. Barish, and K. Thorne expanded our knowledge about the Universe and led to the development of fundamentally new observation channels for distant space objects that develop multichannel astronomy, including gravitational wave astronomy [13].

3. Nobel Prize in physics for 2018. On October 2, 2018, the Royal Swedish Academy of Sciences announced the awarding of the next Nobel Prize in physics. Its winners «... for revolutionary inventions in the field of laser physics» became [19]: American physicist *Arthur Ashkin* (born on September 2, 1922, Fig. 8), American-French physicist *Gérard Albert Mourou* (born on June 22, 1944, Fig. 9) and Canadian physicist *Donna Strickland* (born on May 29, 1959, Fig. 10). This time, the Nobel Committee press release emphasized that D. Strickland became the third woman in history to be the winner of this prestigious physics Prize (after French-Polish radiochemist *Maria Skłodowska-Curie* (1867-1934) and American-German physicist *Maria Göppert-Mayer* (1906-1972) [16]).

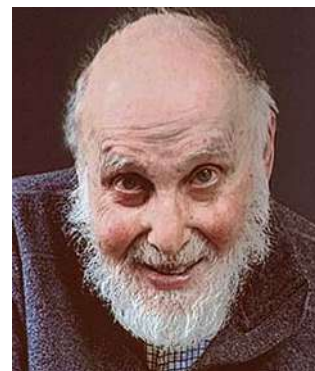


Fig. 8. Outstanding American physicist Arthur Ashkin (born in 1922), Laureate of Nobel Prize in Physics for 2018 [19]



Fig. 9. Outstanding American-French physicist Gérard Albert Mourou (born in 1944), Laureate of Nobel Prize in Physics for 2018 [19]



Fig. 10. Outstanding Canadian physicist Donna Strickland (born in 1959), Laureate of Nobel Prize in Physics for 2018 [19]

The winners of the 2018 Prize, named after A. Nobel, were awarded for their scientific work in the field of physical optics and laser technology, which they performed dozens of years ago. An interesting fact is that A. Ashkin was the oldest Nobel Prize winner in its entire history [19]. By the way, this scientist until 1992 headed the Department of Physical Optics and Electronics at Bell Labs, USA. Parents of A. Ashkin before the 1917 revolution in the Russian Empire left Odessa city for the United States. Remarkable inventions in the field of laser physics by A. Ashkin, G. Mourou and D. Strickland greatly expanded the practical application of light pressure (photons) in the world, which was made possible thanks to the tremendous progress of quantum optical generators – lasers («*Light Amplification by Stimulated Emission of Radiation*» [16]. Just from the official formulation of the Nobel Committee for the scientific merits of the above new physicist Laureates their applied orientation with obvious technological application follows. The last time a similar event in the history of the «Nobel» was observed in 2014, when three Japanese scientists were awarded the Nobel Prize in physics for the outstanding invention of blue LEDs [8, 19].

Note that in the period 2015-2017 the Nobel Prizes in physics (see Sections 1, 2 of this paper and [8]) were awarded to scientists for their outstanding results in the field of basic research. It is known that the pressure of the photon flux (ordinary light) is extremely small [9]. For example, the force with which sunlight pushes planet Earth in outer space is sixty trillion times less than the force of its attraction by the Sun [19]. Therefore, it was no coincidence that in 1905 the famous English physicist John Henry Poynting (1876-1943) in his presidential

address to the British Physical Society noted that experiments performed in the world (including Professor at Moscow University Peter Nikolaevich Lebedev, 1866-1912) to determine the value of light pressure demonstrated the extreme smallness of this physical effect, «... *excluding it from consideration in earthly affairs*» [19]. This conclusion in physical science remained almost right up to the invention of lasers in quantum electronics [9, 16].

It is known that laser radiation has such rare physical properties as: exceptional spectral purity (that is, the ability to generate almost perfect monochromatic electromagnetic radiation) and high spatial coherence [9, 19]. In this regard, the laser beam (light) can be focused into a microscopic spot with a diameter of only slightly more than one length of the corresponding electromagnetic wave. Therefore, with a laser emitter power of only a few watts, we can obtain such an intensity of the light flux of a given electromagnetic radiation that will be a thousand times higher than the total intensity of the visible spectrum of solar radiation, averaging about 1376 W/m^2 at the entrance to the Earth's atmosphere [2, 9, 19]. Note that in the 1960s, the laser radiation intensity was about 10^{10} W/cm^2 [19]. In the 1970s, it was already about 10^{15} W/cm^2 [19]. Until the mid-1980s, this increase in the intensity of the laser beam continued at a slow pace [19].

A. Ashkin quickly appreciated the unique capabilities of lasers almost immediately after their invention. Note that the world's first artificial ruby crystal laser containing aluminum oxide with a small admixture of chromium atoms was created in May 1960 by American physicist Theodore Harold Maiman (1927-2007), who worked in the research center of the Company Hughes Research Laboratories, USA [16]. As a result of a series of witty experiments conducted at Bell Labs, USA using such a laser, A. Ashkin in the 1960s invented a «*light trap*» that reliably holds the smallest objects of various nature [19]. These studies took him at least 25 years. In 1986, he, together with his collaborators, for the first time described in detail the experimental results obtained in the USA on optical «capture» using a «*light trap*» of dielectric particles ranging in size from tens of nanometers to tens of micrometers [19]. Over time, A. Ashkin's «*light traps*» were called «*optical tweezers*» or «*laser tweezers*». In subsequent years, this laser technology has been greatly improved and its capabilities have expanded significantly. As it turned out, «*laser tweezers*» can not only hold micro- and nano-objects, but can also move them, rotate and even cut them into pieces. Now they are widely used in molecular biology, genomics, virology, and in other fields of science and technology [19]. For example, laser cooling of neutral atoms to ultralow temperatures and their «trapping» has become the most important area of practical application of «*optical tweezers*». By the way, for his work in the field of low-temperature physics using laser technology, his former employee and US citizen Steven Chu with his compatriot William Daniel Phillips and French physicist

Claude Cohen-Tannoudji became Nobel Laureates in physics in 1997 [2, 5].

It can be seen from the above that A. Ashkin owed his Prize to the method of manipulating nano- and micro-objects using laser radiation with a relatively low energy. In contrast to A. Ashkin, his Laureate colleagues G. Mourou and D. Strickland worked in the field of laser physics with high energy indicators. By 1985, they had developed a very effective way to increase the power of laser pulses [19]. Thanks to this method, the power density of laser radiation again went into sharp growth, and now it has reached an index of up to 10^{23} W/cm² [19].

The essence of an effective method for amplifying laser pulses proposed by foreign experimental physicists G. Mourou and D. Strickland according to [19] is as follows. First, an ultrashort laser pulse of light radiation is passed through a pair of diffraction gratings, which stretch it over several orders of time. Note that in their first experiments, G. Mourou and D. Strickland used fiber optic cable for this purpose, but diffraction gratings proved to be more efficient. As a result, the peak energy of the electric field of the laser pulse drops so much that it passes through an optical radiation amplifier (a sapphire crystal doped with titanium ions is usually used for this) without disturbing (destroying) the crystal structure of the latter. Then, a repeatedly amplified laser pulse is passed through the next couple of diffraction gratings. These gratings compress it (laser pulse) to the original length (time duration). As a result, a very short laser pulse of extremely high intensity is obtained at the output of the described optical system. The first joint experiments by G. Mourou and D. Strickland, conducted by them at the Laser Energy Laboratory of the University of Rochester, USA, using this method of amplification of chirped laser pulses led to the creation of picosecond terawatt laser systems [19].

The field of practical application for today of ultrashort superpowerful laser pulses has proved to be extremely extensive, including various branches of science and technology. We point out that it extends from conducting many experiments in the field of fundamental and applied physics, utilization in military affairs (combat lasers), modifying (structuring) the surfaces of various parts, amplifying photoluminescence signals, performing hypersensitive chemical analysis of substances, creating new metamaterials, and then to surgical treatment of myopia and astigmatism in millions of people on our planet [16, 19].

4. Nobel Prize in physics for 2019. On October 8, 2019, the Royal Swedish Academy of Sciences published the names of Nobel Prize winners in physics for 2019 «... for their contribution to our understanding of the evolution of the Universe and the place of the Earth in space» They are famous astronomers and astrophysicists [20]: Canadian *Phillip James Edwin Peebles* (born on April 25, 1935, Fig. 11) and the Swiss *Michel Mayor* (born on January 12, 1942, Fig. 12) and *Didier Queloz* (born on February 23, 1966, Fig. 13). We point out more

specifically that J. Peebles was awarded this Prize «... for theoretical discoveries in physical cosmology», and M. Major and D. Queloz «... for the discovery of an exoplanet orbiting a solar-type star» [20]. In a press release from the Nobel Committee in connection with the award of this prestigious Prize, it was stated that these «... discoveries of scientists are revolutionary for astronomy» [20].



Fig. 11. Outstanding Canadian-American astrophysicist Phillip James Edwin Peebles (born in 1935), Laureate of Nobel Prize in Physics for 2019 [20]



Fig. 12. Outstanding Swiss astrophysicist Michel Mayor (born in 1942), Laureate of Nobel Prize in Physics for 2019 [20]



Fig. 13. Outstanding Swiss astrophysicist Didier Queloz (born in 1966), Laureate of Nobel Prize in Physics for 2019 [20]

J. Peebles (for many years he was a Professor at Princeton University, USA) turned out to be one of those prominent astrophysicists in the world who theoretically predicted the existence and described the properties of relict radiation that filled our Universe after the Big Bang in it [20]. In 1964, J. Peebles theoretically came to the conclusion that space is penetrated by isotropic microwave radiation with temperature of the order of 10 K [20]. He published the results of his calculations in 1965 in the authoritative American scientific Journal «*Astrophysical Journal*» [20], which simultaneously published the experimental work of young US scientists Arno Penzias and Robert Woodrow Wilson, then members of Bell Labs, USA. The latter succeeded in measuring the background radio emission of the Milky Way galaxy using a six-meter horn satellite dish antenna [15]. Their receiving radio equipment tuned to a 7.35 cm long electromagnetic wave registered a weak but very stable signal, which was independent of the position of the antenna in the Earth's atmosphere. In 1964, these American scientists came to the conclusion that this electromagnetic signal could not have an intragalactic origin. They realized that they were dealing with a signal whose spectral composition corresponded to the emission spectrum of an absolutely black body heated to 3.5 K according to their then estimate [20]. This electromagnetic radiation came from all sides of the earthly firmament and was, in their opinion, completely isotropic [20]. This experimental work by A. Penzias and R.W. Wilson famous world astronomers consider a landmark achievement in 20th-century astrophysics. Therefore, it was no accident that in 1978 it brought them the Nobel Prize in physics [20, 21]. According to modern data, cosmic microwave relict radiation discovered by these talented physicists arose 380 thousand years after the Big Bang, which occurred about 12 billion years ago [2]. Outer space was then filled with plasma, consisting of protons, electrons, and helium ions, which was in thermodynamic equilibrium with «hot» electromagnetic radiation. When, due to the expansion of space, this plasma cooled to about 4000 K, the formation of electroneutral atoms (first helium, and then hydrogen) began in it [20].

For greater clarity in the complex intergalactic problem under consideration, we note that the temperature of the relict radiation decreases inversely with the expansion of outer space. Since the linear dimensions of our Universe have increased by three orders of magnitude since the initial release of photons, the degree of its heating and, accordingly, the energy of the relict radiation have also decreased. According to current data, its temperature is 2.725 K [2, 7, 20]. Therefore, its initial assessment by A. Penzias and R.W. Wilson, although was somewhat overpriced, is still surprisingly close to the truth. The intensity of microwave relict radiation reaches a peak at waves 1 mm long, not able to penetrate the Earth's atmosphere. Therefore, the discoverers actually

recorded only its long-wave tail, and the full spectrum was determined much later using high-altitude balloons and spacecraft. However, these scientists determined the general form of this spectrum extremely accurately, although their instruments were far from perfect [20].

It should be noted that the predictions of J. Peebles are associated not with the fact of the existence of microwave relict radiation in the Universe, but with its properties [22]. Firstly, this Nobel Laureate on the basis of theoretical models developed by him showed that relict radiation plays an important role in the formation of galaxies of the Universe. Secondly, he calculated the spectrum of fluctuations of this relict radiation. He developed a new model of the Universe and with its help estimated how this radiation would look if you add in it (this model) «cold dark» matter to the ordinary matter of the Universe. Thirdly, he added «dark» energy with negative density to this model and again recalculated the spectrum of relict radiation. On a similar cosmological model, J. Peebles studied how the hypothetical entities introduced by him affect the evolution of the Universe as a whole and the formation of its galaxies in particular. Essentially, he laid the foundations of theoretical cosmology. Here, we should not forget about the great contribution to this science made by the famous Soviet theoretical physicist Yakov Borisovich Zeldovich (1914-1987) [16].

M. Mayor and D. Queloz, working at the Geneva Observatory, practically in 1994, jointly began a systematic search for exoplanets (earth-like planets) in the Milky Way galaxy, located near its «normal» (lying on the main astro sequence) stars and «red giants». Exoplanets previously discovered before them by other astronomers of the world, located near pulsars [15], did not present special prospects for science. Valuable to astrophysicists were only those exoplanets that were placed around stars of the solar type. In these astronomical observations, they used a unique high-resolution spectrometer ELODIE (it was commissioned at the end of 1993) mounted on a 193-cm telescope of the observatory [20]. In the fall of 1994, using the indicated equipment, these scientists discovered that one of the observed stars («51 Pegasus») showed fluctuations in its radial velocity with period of about four Earth days. It was for this (for observing peculiar «star swings» from Earth) that they needed an ultraprecise spectrometer that could sense the weak shifts of the emission spectrum of stars accompanying the rotation of exoplanets around them. On November 23, 1995, M. Mayor and D. Queloz published their paper in the Journal *Nature*, from which the world learned about the long-awaited discovery of the planet orbiting an ordinary star of the main astro sequence [20]. In such a way they discovered the first exoplanet (Fig. 14) from that family of planets, which they later called the «hot» Jupiters. The newly discovered exoplanet «51 Pegasus b» was nothing like the satellites of the Sun. She circled in a circular trajectory with radius of about 7.5 million kilometers, making one revolution around her star

in just 4.2 Earth days. At the same time, it had a very large mass – about 0.47 of the mass of Jupiter. Further in 1995, discoveries by other astronomers of two more exoplanets with mass of several Jupiters orbiting the stars «70 Virgo» and «47 Ursa Major» [20] followed. Since then, planetary astronomy once and for all went beyond the limits of the solar system. And then similar discoveries rained down one after another. We point out that after such discoveries in science, astronomers who believed in the technical capabilities of their high-precision measuring instruments have already discovered more than 4,100 exoplanets (new «worlds») scattered across our huge Milky Way galaxy [20, 22].



Fig. 14. General view of the exoplanet «51 Pegasus b» (left), discovered in 1995 in our Milky Way galaxy by prominent Swiss astrophysicists M. Mayor and D. Queloz [22]

The successful «pursuit» of exoplanets not only gave astronomy rich information, but also attracted public attention to this ancient science and increased its prestige. Therefore, it is not surprising that in the 21st century, the world scientific community made serious efforts to develop new astronomical devices of the next generations, designed for search of such exoplanets to be potentially inhabited by intelligent beings in space [20, 22]. The valuable results of astrophysical research by M. Major and D. Queloz brought astronomy to a new path of its further development. Summarizing, we can reasonably say that J. Peebles and M. Major with D. Queloz, through their outstanding scientific works in astronomy and astrophysics, have opened up a huge wealth of new ways in studying the space surrounding us.

Conclusions.

Winners of the Nobel Prize in Physics for the period 2016-2019 made a great contribution to the further development of world science and modern technology. Their outstanding scientific and technical achievements allow to expand and deepen people's knowledge about matter, about the evolution of our Universe, to understand the place occupied by planet Earth and its role in space, and to effectively direct advanced laser technologies developed in the world to serve humanity.

REFERENCES

1. Available at: https://elementy.ru/novosti_nauki/432847/Nobelevskaya_premiya_po_fizike_2016 (accessed 15 May 2018). (Rus).
2. Baranov M.I. *Antologija vydajushchih dostizhenij v nauke i tekhnike: Monografija v 4-h tomah. Tom 4* [An anthology of the distinguished achievements in science and technique: Monograph in 4 vols. Vol. 4]. Kharkiv, PhPB Panov A.N. Publ., 2016. 415 p. (Rus).
3. Available at: <https://lenta.ru/news/2017/10/03/nobelprizeinphysics> (accessed 23 June 2018). (Rus).
4. Baranov M.I. An anthology of the distinguished achievements in science and technique. Part 35: Nobel Prize Laureates in Physics for 1990-1994. *Electrical engineering & electromechanics*, 2016, no. 6, pp. 3-8. doi: 10.20998/2074-272X.2016.6.01.
5. Baranov M.I. An anthology of the distinguished achievements in science and technique. Part 36: Nobel Prize Laureates in Physics for 1995-1999. *Electrical engineering & electromechanics*, 2017, no. 1, pp. 3-9. doi: 10.20998/2074-272X.2017.1.01.
6. Baranov M.I. An anthology of the distinguished achievements in science and technique. Part 37: Nobel Prize Laureates in Physics for 2000-2004. *Electrical engineering & electromechanics*, 2017, no. 2, pp. 3-12. doi: 10.20998/2074-272X.2017.2.01.
7. Baranov M.I. An anthology of the distinguished achievements in science and technique. Part 38: Nobel Prize Laureates in Physics for 2005-2010. *Electrical engineering & electromechanics*, 2017, no. 3, pp. 3-15. doi: 10.20998/2074-272X.2017.3.01.
8. Baranov M.I. An anthology of the distinguished achievements in science and technique. Part 39: Nobel Prize Laureates in Physics for 2011-2015. *Electrical engineering & electromechanics*, 2017, no. 4, pp. 3-9. doi: 10.20998/2074-272X.2017.4.01.
9. Kuz'michev V.E. *Zakony i formuly fiziki* [Laws and formulas of physics]. Kiev, Naukova Dumka Publ., 1989. 864 p. (Rus).
10. *Bol'shoj illjustrirovannyj slovar' inostrannyh slov* [Large illustrated dictionary of foreign words]. Moscow, Russkie slovari Publ., 2004. 957 p. (Rus).
11. Available at: https://www.gazeta.ru/science/2016/10/04_a_10229453.shtml (accessed 15 May 2018). (Rus).
12. Available at: <https://www.nobelprize.org/prizes/physics/2016/summary> (accessed 16 June 2018). (Rus).
13. Available at: https://elementy.ru/novosti_nauki/433128/Nobelevskaya_premiya_po_fizike_2017 (accessed 26 June 2018). (Rus).
14. Available at: <https://lenta.ru/news/2017/10/03/nobelprizeinphysics> (accessed 25 April 2018). (Rus).
15. Baranov M.I. *Antologija vydaiushchih dostizhenij v nauke i tekhnike: Monografija v 4-kh tomakh. Tom 2*. [An anthology of outstanding achievements in science and technology: Monographs in 4 vols. Vol. 2]. Kharkov, NTMT Publ., 2013. 333 p. (Rus).
16. Baranov M.I. *Antologija vydaiushchih dostizhenij v nauke i tekhnike: Monografija v 4-h tomakh. Tom 1*. [An anthology of outstanding achievements in science and technology: Monographs in 4 vols. Vol. 1]. Kharkov, NTMT Publ., 2011. 311 p. (Rus).
17. Available at: <https://fakty.ua/246875-obvavleny-laureaty-nobelevskoj-premii-po-fizike-za-2017-god> (accessed 06 April 2018). (Rus).

18. Available at: <https://www.popmech.ru/science/390252-nobelevskaya-premiya-po-fizike-2017-gravitacionnye-volny> (accessed 16 October 2018). (Rus).

19. Available at: https://elementy.ru/novosti_nauki/433343/Nobelevskaya_premiya_po_fizike_2018 (accessed 20 September 2018). (Rus).

20. Available at: https://elementy.ru/novosti_nauki/433548/Nobelevskaya_premiya_po_fizike_2019 (accessed 10 November 2018). (Rus).

21. Cholakov V. *Nobelevskie premii. Uchenye i otkrytiia* [Nobel Prizes. Scientists and discovery]. Moscow, Mir Publ., 1986. 368 p.

22. Available at: <https://www.bbc.com/russian/news-49960797> (accessed 11 May 2018). (Rus).

Received 27.11.2019

M.I. Baranov, Doctor of Technical Science, Professor, Scientific-&-Research Planning-&-Design Institute «Molniya», National Technical University «Kharkiv Polytechnic Institute», 47, Shevchenko Str., Kharkiv, 61013, Ukraine, phone +380 57 7076841, e-mail: baranovmi@kpi.kharkov.ua.

How to cite this article:

Baranov M.I. An anthology of the distinguished achievements in science and technique. Part 53: Nobel Prize Laureates in Physics for 2016-2019. *Electrical engineering & electromechanics*, 2020, no.2, pp. 3-12. **doi: 10.20998/2074-272X.2020.2.01.**

V.I. Milykh, L.V. Shilkova

CHARACTERISTICS OF A CYLINDRICAL INDUCTOR OF A ROTATING MAGNETIC FIELD FOR TECHNOLOGICAL PURPOSES WHEN IT IS POWERED FROM THE MAINS AT A GIVEN VOLTAGE

Introduction. A computational analysis of the characteristics of an inductor of a rotating magnetic field for technological purposes is presented. The design of its stator is borrowed from a three-phase induction motor. The cylindrical cavity inside the stator is occupied by a working chamber into which a granular or liquid processed substance is loaded. The processing is carried out with elongated ferromagnetic elements moving with a magnetic field. Problem. The purpose of the article is a study of the electromagnetic, phase, and energy characteristics of an inductor at its operation under load mode with a given voltage of the stator winding. Methodology. The study is performed on the basis of numerical calculations of the magnetic field, taking into account the anisotropy of the low-magnetic medium in the working chamber. Its discrete medium is represented homogeneous with different magnetic permeabilities on mutually perpendicular axes. The technique of transition from the results of the magnetic field calculation to the electric, magnetic, phase and energy parameters of the inductor is given. This is facilitated by the electrical equivalent circuit of the stator phase winding, the equilibrium equation of its electrical quantities, vector diagrams and an iterative method for determining the current at a given voltage. Results. Mutual dependencies of a number of inductor parameters are formed into a family of characteristics exhibiting its properties in an operating mode with a changing load. Characteristics include such quantities as magnetic flux linkage of the stator winding, its current and EMF, phase shifts between them, electromagnetic torque, expended and useful power and its losses, power factor and efficiency. In this article, a feature of this mode is the stability of the stator winding voltage in the inductor. This complements the earlier studies of the inductor in the mode with stabilization of the winding current, which allows to compare these options. On the example of a test sample of an inductor, a number of its characteristics are shown, vector diagrams of its electric and magnetic quantities illustrating their mutual phase shifts are given. Practical value. The presented technique for determining the electric and magnetic quantities of the inductor and their phase relationships, and also the shown family of characteristics can contribute to increasing the design efficiency and improving the inductors of the considered type. The developed technique has the universality property, as it is capable of displaying their various circuit and constructional design parameters. References 9, figures 8.

Key words: three-phase cylindrical inductor, working chamber, ferromagnetic elements, rotating magnetic field, numerical calculations, load mode, stable voltage, electric, magnetic and energy parameters, phase shifts.

Надано розрахунковий аналіз характеристик індуктора обертового магнітного поля технологічного призначення. Конструкція його статора запозичена у трифазного асинхронного двигуна. Циліндрична порожнина усередині статора зайнята робочою камерою, в яку завантажується сипка або рідка оброблювана речовина. Обробка відбувається довгастими ферромагнітними елементами, що рухаються з магнітним полем. Викладена методика отримання електричних, магнітних і енергетичних величин індуктора, яка заснована на чисельно-польових розрахунках з урахуванням магнітної анізотропії середовища, що заповнює робочу камеру. Взаємні залежності низки величин сформовані в сім'ю характеристик, які проявляють його властивості в робочому режимі. У цій статті його особливістю є стабільність напруги обмотки статора індуктора. Це доповнює проведені раніше дослідження індуктора в режимі із стабілізацією струму обмотки, що дозволяє порівняти такі варіанти роботи. На прикладі тестового зразка індуктора показано ряд його характеристик, приведені векторні діаграми електричних і магнітних величин, що ілюструють їх взаємні фазові зміщення. Бібл. 9, рис. 8.

Ключові слова: трифазний циліндричний індуктор, робоча камера, ферромагнітні елементи, магнітне поле, що обертається, чисельні розрахунки, режим навантаження, стабільна напруга, електричні, магнітні і енергетичні параметри, фазові зсуви.

Представлен расчетный анализ характеристик индуктора вращающегося магнитного поля технологического назначения. Конструкция его статора заимствована у трехфазного асинхронного двигателя. Цилиндрическая полость внутри статора занята рабочей камерой, в которую загружается сыпучее или жидкое обрабатываемое вещество. Обработка происходит движущимися с магнитным полем продолговатыми ферромагнитными элементами. Изложена методика получения электрических, магнитных и энергетических величин индуктора, основанная на численно-полевых расчетах с учетом магнитной анизотропии среды, заполняющей рабочую камеру. Взаимные зависимости ряда величин сформированы в семейство характеристик, проявляющих его свойства в рабочем режиме. В данной статье его особенностью является стабильность напряжения обмотки статора индуктора. Это дополняет проведенные ранее исследования индуктора в режиме со стабилизацией тока обмотки, что позволяет сравнить такие варианты работы. На примере тестового образца индуктора показан ряд его характеристик, приведены векторные диаграммы электрических и магнитных величин, иллюстрирующие их взаимные фазовые смещения. Библ. 9, рис. 8.

Ключевые слова: трехфазный цилиндрический индуктор, рабочая камера, ферромагнитные элементы, вращающееся магнитное поле, численные расчеты, режим нагрузки, стабильное напряжение, электрические, магнитные и энергетические параметры, фазовые смещения.

Introduction. In a number of industries, the technological treatment of liquid or granular substances is done with magnetic stirrers, grinders and separators [1-5].

The magnetic fields that provide this are diverse in structure and character, and rotating fields have their

© V.I. Milykh, L.V. Shilkova

place here. They are created by an inductor, the design of which is borrowed from the stator of a three-phase induction motor [6].

A working chamber is placed in the cylindrical cavity of the stator, through which the processed substance is passed. Processing is done by ferromagnetic elements (FEs) in the form of elongated segments of steel wire, moving with a rotating field. They create the so-called «eddy layer» in the chamber [5-7]. The thin shell of the camera is made non-magnetic and therefore does not interact with the field.

From the analysis of scientific publications it follows that the study of the electromagnetic parameters of the inductor is carried out mainly on the basis of methods from the theory of magnetic circuits. However, with very large gaps and a discrete low-magnetic space inside the working chamber, the representation of the structure of the inductor in several homogeneous magnetic sections becomes problematic.

Clarification of electromagnetic calculations and improvement of the design of the inductor is possible through the use of numerical-field methods. And on this basis, in [7], studies of electromagnetic and energy parameters and the corresponding characteristics of the inductor during its operation in the load mode have already been carried out. The condition for this was the stability of the stator winding current of the inductor with appropriate regulation of its voltage. And it was also noted there that the mode of interest is a given constant voltage mode.

The goal of the paper is study of electromagnetic, phase and energy characteristics of the inductor during its operation in load mode with a given voltage of the stator winding. This is performed, as in [7], by means of numerical-field calculations taking into account the anisotropy of a low-magnetic medium in a working chamber filled with ferromagnetic elements.

Object of study. The electromagnetic system of the inductor is adopted as in [7], and here it is represented by its cross section (Fig. 1). In the calculations, the rectangular (x, y) and polar (r, α) coordinate systems are used, and α is counted from the y axis.

The inductor has the number of pairs of poles $p = 1$, phases $m_s = 3$, slots $Q_s = 42$ and turns of the phase winding $N_s = 28$. The technical conditions set the radius of the surface of the chamber $r_{re} = 0.15$ m, the axial length of the core $l_a = 0.3$ m, its inner radius $r_{si} = 0.175$ m. The stator winding is distributed, two-layer, its relative shortening is 18/21, the circuit is «star». The fill factor K_{Fe} of the core with electrical steel grade 2013 is 0.97.

The rated phase voltage of the stator winding $U_{sN} = 220$ V, frequency $f_s = 50$ Hz.

A fragment of an idealized structure of FEs uniformly distributed in the working chamber is shown in Fig. 2. In general, this corresponds to the data of experimental studies on the physical model of the inductor [6]. Although the actual distribution of elements is somewhat more chaotic, idealization is necessary for organizing available calculations.

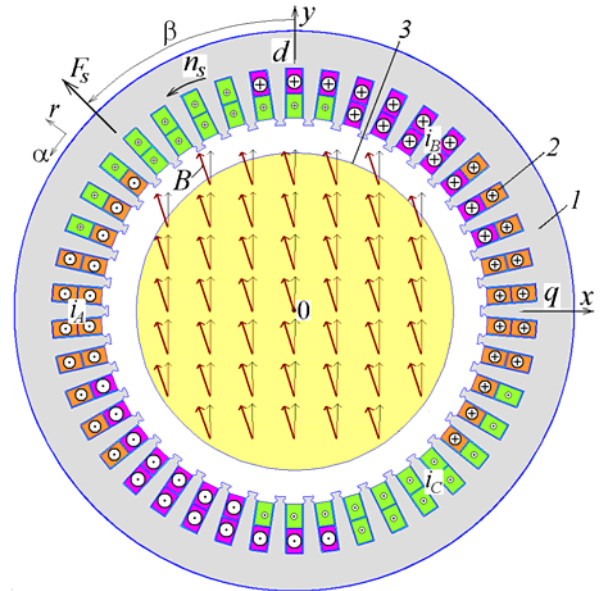


Fig. 1. The cross section of the electromagnetic system of the inductor: 1 – core; 2 – winding; 3 – surface of the working chamber

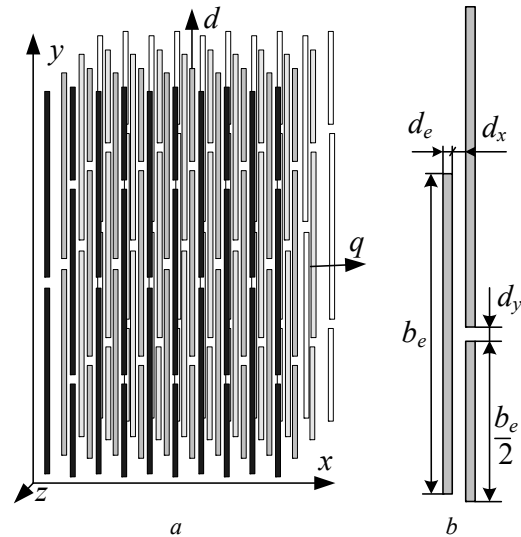


Fig. 2. Idealized structure of ferromagnetic elements (a), their sizes and gaps (b)

For the test case, according to the notation of the quantities (Fig. 2,b), their values are taken: $d_e = 1$ mm; $b_e = 23.8$ mm; $d_x = 1.43$ mm; $d_y = 1$ mm, the fill factor of the chamber with elements in the plane xy (Fig. 2,a) $K_{Fes} = 0.35$, by volume $K_{Fev} = 0.122$.

The essence of numerical field calculations. A rotating magnetic field in the inductor is excited by a symmetric three-phase system of stator winding currents (Fig. 1):

$$\begin{aligned} i_A &= I_m \cos(\omega_s t + \beta); & i_B &= I_m \cos(\omega_s t - 2\pi/3 + \beta); \\ i_C &= I_m \cos(\omega_s t + 2\pi/3 + \beta), \end{aligned} \quad (1)$$

where t is time; $I_m = \sqrt{2}I_s$ is the amplitude of the phase currents at their effective value I_s ; $\omega_s = 2\pi f_s$ is the angular frequency; β is the initial phase of the currents, which gives the angular displacement of the stator winding MMF vector F_s from the y axis, necessary for a particular calculation mode.

The instantaneous directions of currents (1) in the winding rods are shown in Fig. 1 for $t = 0$ and $\beta = 45^\circ$, the corresponding direction of the MMF vector F_s is also given.

In the cross section of the inductor (Fig. 1), a plane-parallel magnetic field is described by the well-known differential equation:

$$\text{rot}[\mu_a^{-1} \text{rot}(\vec{k}A_z)] = \vec{k}J_z, \quad (2)$$

where \vec{k} is the axial unit; J_z, A_z are the components of the vectors of current density and magnetic vector potential along the z axis; μ_a is the absolute magnetic permeability.

The propagation of the field is limited by the circle on the outer surface of the stator core by setting the boundary condition $A_z = 0$.

Numerical calculations of the magnetic field are performed by the FEMM program [8] by the Finite Element Method, which is controlled by the Lua script created by analogy with [9].

The magnetic permeability μ_a in the laminated core of the stator and nonmagnetic medium when calculating the field is taken into account in a known manner [8]. In the working chamber, a discrete magnetic-nonmagnetic medium (Fig. 2) is represented by a continuous homogeneous medium with different magnetic permeabilities μ_d and μ_q along the longitudinal d and perpendicular to it transverse q axes (Fig. 1, 2). Different magnetic properties in the chamber in different directions correspond, in fact, to the magnetic anisotropy of the medium. The justification of this transition and the principle of determining the values of μ_d и μ_q are given in [7], where the relative values of the magnetic permeability $\mu_{rd} = 10$ p.u.; $\mu_{rq} = 1.5$ p.u. were obtained which are also used in this paper.

Test calculation of the magnetic field and the principle of operation of the inductor. In Fig. 1, the longitudinal axis d coincides with the y axis. Here, a priori a «snapshot» of the vectors of the magnetic flux density \mathbf{B} and MMF F_s is shown.

When the inductor operates under load, the angle β is within the range $0 - 90^\circ$, and at extreme values 0 and 90° there is no electromagnetic torque, and this corresponds to idle mode [7].

As a «point» example, a test calculation of the inductor in the load mode with a rated voltage U_{sN} and at $\beta = 45^\circ$ was performed. The phase current I_s was 455 A, which was substantiated in [7].

In Fig. 1, the bold arrows show the calculated corresponding distribution of the magnetic flux density vectors \mathbf{B} in the conditioned mode (on one scale). They are rotated with respect to the d axis in the direction of rotation of the field indicated by the arrow n_s , but they lag behind the MMF vector F_s , which «leads» the vectors of the remaining quantities. Note that in the center of the working chamber, magnetic flux density is 0.36 T.

In idle mode, the vectors F_s and \mathbf{B} (thin arrows) in Fig. 1 are directed, naturally, along the longitudinal axis d . It can be seen that, under load and during idle, the magnetic field in the chamber is almost uniform.

It is known that elongated ferromagnetic elements tend to be located along the lines of force of the magnetic

field and, thus, parallel to the magnetic flux density vectors. The processed substance entering the working chamber cannot immediately «pick up» the rotation frequency corresponding to the rotation frequency of the magnetic field n_s , and therefore is penetrated by elements moving with the field.

Therefore, due to the braking effect of the medium being processed, between the direction of the magnetic flux density vectors \mathbf{B} of the magnetic field that rotates and the elements oriented along the d axis, an angle shift must be formed. This is a prerequisite for creating the electromagnetic torque (EMT) M_{em} acting on the elements, and this determines the intensity of processing heterogeneous mixtures according to a given technological process.

In fact, it is revealed that in the considered inductor the EMT is reactive, and, therefore, its principle of operation corresponds to a synchronous reluctance motor, which was already noted in [7]. That is why – like synchronous electric machines, the longitudinal axis d is assigned in the working chamber in the direction of orientation of the ferromagnetic elements, and the transverse axis q is directed perpendicularly. In the steady state load conditions, these axes rotate together with the magnetic field and FEs.

Determination of magnetic, electrical and energy quantities of the inductor. The setting or calculation of such quantities is an important and necessary problem in calculating the electromagnetic and energy parameters and characteristics of the inductor, which are presented below in the text.

One of the basic values of the analysis of a number of electromagnetic parameters of the inductor is the magnetic flux linkage (MFL) Ψ_a of the stator winding. In the FEMM program, it is determined using the Lua script [8, 9] with a special function.

After calculation, by scanning the phase winding with its «mask», the numerical angular function of the MFL is formed from the instantaneous structure of the magnetic field:

$$\Psi_k(\alpha_k), k = 1, 2, \dots, K, \quad (3)$$

where the required number of positions K is $Q_s / 2$.

This function is periodic, is represented by a harmonic Fourier series, and is transformed into the temporal function of the MFL, as shown in [7]. Of this series, the first harmonic is used, as is customary in electric machines:

$$\Psi_a = \Psi_m \cos(\omega_s t + \gamma_{\Psi a}). \quad (4)$$

By means of the law of electromagnetic induction, phase EMF of the winding is derived from (4):

$$e_a = \omega \Psi_m \cos(\omega_s t + \gamma_{\Psi a} - \pi / 2), \quad (5)$$

whence its effective value and initial phase:

$$E_a = \sqrt{2} \pi f_s \Psi_m; \gamma_{Ea} = \gamma_{\Psi a} - \pi / 2. \quad (6)$$

The set of processes in the phase winding of the stator in [7] is represented by an electrical equivalent circuit, as well as by the corresponding equation of equilibrium of voltages and EMF:

$$\underline{U}_s = -\underline{E}_a + jX_v I_s + (R_s + R_{mag}) I_s, \quad (7)$$

where, based on (1) and (6), the complexes of current and EMF of this winding are known:

$$\underline{I}_s = I_s e^{j\beta}; \quad \underline{E}_a = E_a e^{j\gamma_{Ea}}. \quad (8)$$

Formula (7) includes the active resistance R_s of the stator winding and the reactance of its frontal scattering X_v . They are calculated according to classical methods for calculating induction motors and amounted to: $R_s = 9.68 \text{ m}\Omega$ and $X_v = 22 \text{ m}\Omega$.

Active resistance, representing the power of magnetic losses P_{mag} in the stator core, is sought by the formula:

$$R_{mag} = P_{mag} / (m_s I_s^2), \quad (9)$$

and such a power, as in [7], is obtained in the course of numerical-field calculation.

According to (7), the voltage complex is found in exponential form $\underline{U}_s = U_s e^{j\gamma_{Us}}$, which gives its effective value U_s . The phase shifts of the EMF \underline{E}_a and voltage \underline{U}_s relative to the current \underline{I}_s are obtained through their initial phases γ_{Ea} and γ_{Us} already determined, namely: $\varphi_{Ea} = \gamma_{Ea} - \beta$ and $\varphi_s = \gamma_{Us} - \beta$.

In the load mode of the inductor, by the test calculation of the magnetic field and parameters we obtained: $\gamma_{\Psi_a} = 21.1^\circ$; $\Psi_m = 0.938 \text{ Wb}$; $E_a = 208 \text{ V}$; $\varphi_{Ea} = 66.1^\circ$; $P_{mag} = 1.906 \text{ kW}$; $R_{mag} = 3.04 \text{ m}\Omega$; $\varphi_s = 65.8^\circ$. At the same time, the image shown in Fig. 1 is an obtained vector picture of the magnetic flux density, and in addition Fig. 3 shows an obtained picture of field lines. Here, the direction of the vectors of magnetic quantities is given, and their position angles are shown, including the magnetic flux density vector \mathbf{B} in the center of the chamber. Its angle is determined by the coordinate components of the magnetic flux density B_x and B_y : $\alpha_B = \arctg(B_x / B_y) = 15.1^\circ$.

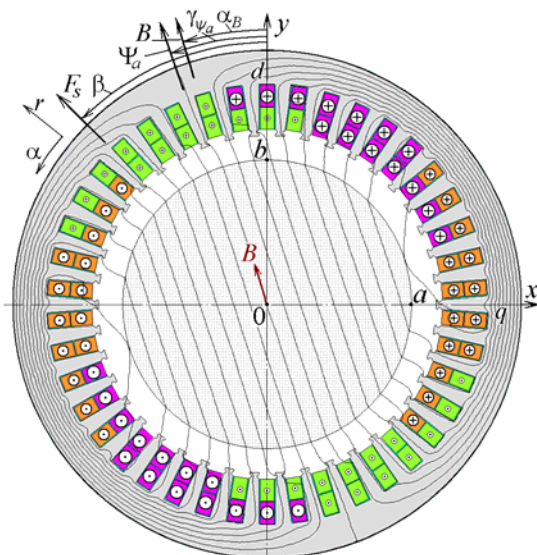


Fig. 3. Magnetic field lines and directions of vectors of magnetic quantities

An interesting fact is that the angle γ_{Ψ_a} turned out to be noticeably smaller than the angle β . In addition, it was found that for $\beta = 0$, the angle γ_{Ψ_a} also has a zero value, and this corresponds to the idle mode, because the EMT,

as shown below, is also equal to zero. The angle of displacement of the MFL vector $\underline{\Psi}_a$ during the transition from the idle to the load, according to the well-known theory of synchronous electric machines, is called the angle of load Θ . Therefore, the angle γ_{Ψ_a} marked in Fig. 3, is the angle of the load of the inductor, that is, we can assume: $\Theta = \gamma_{\Psi_a}$.

Based on the calculation of the magnetic field and the identification of phase (angular) and quantitative relations of electrical and magnetic quantities, we can proceed to determine the energy parameters of the inductor.

Directly by the distribution of the radial B_r and angular B_α components of the magnetic flux density using the FEMM software [8], through the Maxwell magnetic tension tensor, the rotating EMT is obtained, which is essentially reactive:

$$M_{em} = \frac{l_a}{\mu_0(r_{si} - r_{re}) S_\delta} \int r B_r B_\alpha dS, \quad (10)$$

where S_δ is the cross-sectional area of the gap bounded by the radii r_{re} and r_{si} ; μ_0 is the magnetic constant.

The output, i.e. useful inductor power is obtained in the mechanical relationship:

$$P_{out} = M_{em} \omega_s / p. \quad (11)$$

Through electrical quantities, electromagnetic power is obtained:

$$P_{em} = m_s E_a I_s \cos \varphi_{Ea}. \quad (12)$$

Power consumption from the mains – input power:

$$P_{in} = m_s U_s I_s \cos \varphi_s. \quad (13)$$

The power losses in the inductor are the sum of the aforementioned magnetic losses power P_{mag} and the electric losses power in the stator winding:

$$P_{el} = m_s R_s I_s^2. \quad (14)$$

By determined powers, the efficiency of the inductor is found:

$$\eta = P_{out} / P_{in}. \quad (15)$$

Variants of the inductor operation in load mode and the principles of their calculation. When the mode of operation of the inductor changes, concomitant changes in the quantitative-phase ratios of electric and magnetic quantities occur in it. To obtain the characteristics of the inductor, it is necessary to maintain the values of the basic quantities, vary one of the quantities accepted as an argument, and calculate other values– functions.

The initial (generalized) phase of currents β , which is included in (1), is accepted as a variable quantity, which, when the inductor operates, is automatically set depending on the level of its load.

Operation of the inductor is possible in two variants with the corresponding basic values:

- 1) when stabilizing the effective value of the current I_s , that is, $I_s = \text{const}$;
- 2) when stabilizing the similar voltage value U_s , that is, $U_s = \text{const}$.

In the first variant, by varying the angle β for each of its values, the **direct problem** is in fact solved: for a given current I_s , the magnetic field is calculated and the necessary parameters of the inductor including the voltage U_s are obtained from the sequence of formulas (1) – (9).

In the second variant, for a given voltage including the voltage U_s , for each angle β , the **inverse problem** is solved with the result of obtaining a number of parameters of the inductor, as well as the current I_s unknown in this case.

The solution of the inverse problem is more complicated and is obtained by the method of successive approximations with the solution of the direct problem at each iteration.

For such a solution, for each new value of the angle β , the initial approximation of the current $I_{s,1}$ is set (for example, it can be taken from the experience of previous calculations) and the magnetic field is calculated, and then the voltage value $U_{s,1}$ is obtained from (7).

After the first and each subsequent iterative steps, a new value of the stator current is determined by linear interpolation or extrapolation:

$$I_{s,ni+1} = I_{s,ni-1} + \frac{I_{s,ni} - I_{s,ni-1}}{U_{s,ni} - U_{s,ni-1}}(U_s - U_{s,ni-1}), \quad (16)$$

where ni , $ni - 1$, $ni + 1$ are the numbers of the current, previous and next iterations, respectively.

At the first iteration, the number of the previous iteration is $ni - 1 = 0$, for which $I_{s,0} = 0$ and $U_{s,0} = 0$ are accepted, and the values of $I_{s,1}$ and $U_{s,1}$ are already prepared.

At the subsequent iteration, the value $I_{fo,ni+1}$ obtained by (16) already plays the role of $I_{s,ni}$, and the previous value of $I_{s,ni}$ plays the role of $I_{s,ni-1}$. And again, for the updated current $I_{s,ni}$ the magnetic field and phase voltage $U_{s,ni}$ are calculated using formulas (1)-(9).

After the next iteration, the voltage mismatch with its specified value U_s is determined:

$$dU_s = \frac{\text{abs}(U_s - U_{s,ni+1})}{U_s}. \quad (17)$$

Iterations continue until the specified accuracy of the solution $dU_{s,max}$ is obtained, i.e.

$$dU_s < dU_{s,max}. \quad (18)$$

The last value $I_{s,ni+1}$ – this is the current I_s at which the value of U_s will be provided.

For example, at $\beta = 45^\circ$, after setting the initial value of the current $I_{s,1} = 500$ A, the values $I_s = 455$ A and $dU_s = 0.0005$ p.u. (for these calculations, this is even excessive accuracy) were obtained in four iterations.

To identify the quantitative-phase relationships of the values, calculations were performed for the two variants of operation of the inductor noted above in the text. This is done with four values of the angle β : 0° , 30° , 60° and 90° . The obtained currents, MFLs, and voltages are presented in vector form in Fig. 4 in compliance with the proportions for the same values.

When stabilizing the current, its value is taken as in the above calculation of the parameters of the inductor at $U_s = 220$ V and $\beta = 45^\circ$, i.e. $I_s = 455$ A.

When stabilizing the voltage, its value is assumed to be nominal, that is, $U_s = 220$ V.

It turned out that the vectors of the current and the MFL coincide in phase only at extreme values of β – at 0 and 90° . For all other angles (and not only those considered), the MFL vector $\underline{\Psi}_a$ substantially lags in

phase from the current vector \underline{I}_s , as was already shown in Fig. 3.

At $I_s = \text{const}$ (Fig. 4,a), with an increase in the angle β , the values of the MFL and the required voltage U_s significantly decrease. At $U_s = \text{const}$ (Fig. 4,b), with an increase in the angle β , the MFL values are also stable, but the required current I_s significantly increases.

Figure 4 shows the load angle of the inductor Θ , which is counted from the position of the MFL vector $\underline{\Psi}_{a,0}$, corresponding to idle, to the position $\underline{\Psi}_a$, corresponding to any load level. The essence of this angle was discussed above in relation to Fig. 3.

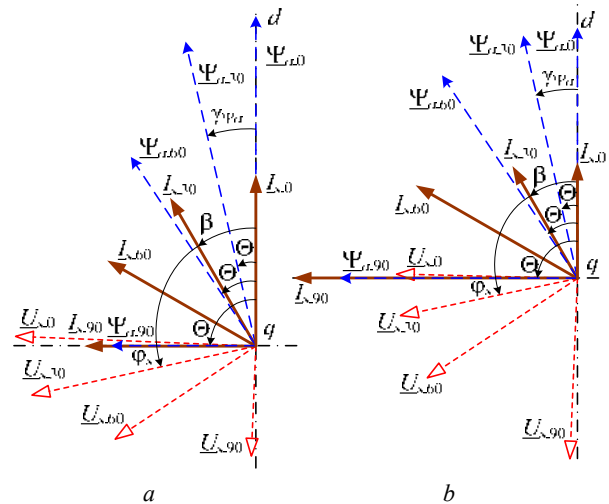


Fig. 4. System of vectors of current vectors, MFL, and voltage at angles $\beta = 0^\circ, 30^\circ, 60^\circ$ and 90° marked in the indices: $a - I_s = \text{const}$; $b - U_s = \text{const}$

Characteristics of the inductor. The above theoretical provisions allow to obtain a family of characteristics of the inductor, which connect its electrical, magnetic, energy and phase (angular) parameters when operating in load mode.

The characteristics of the inductor during operation with stabilization of the stator winding current are considered in [7]. In continuation of these studies, this paper further presents the characteristics of the operation of the inductor with a stable supply voltage. For this mode, you can do without a regulator, using the available mains. However, in this case, the stator winding current must be limited by one – the maximum allowable load. And in the possible range of operation of the inductor with a reduced load, the stator winding will operate with incomplete use of current.

In general, the characteristics show a change in a number of quantities describing the operation of the inductor when its load changes. They can occur with a change in the filling of the working chamber or for other reasons, accompanied by a change in the mechanical moment of resistance from the side of the processed substance. Due to the well-known self-regulation property inherent in electric motors, the corresponding EMT is automatically set. With a stable value of the stator winding voltage, this occurs due to a change in the winding current, load angle, and other phase ratios of electrical and magnetic quantities.

To form the characteristics of the inductor, as was noted, in the calculations, the angle of the initial phase of the currents β included in (1) was varied. And to obtain integral characteristics, the angle range from 0 to 90° was adopted, which was passed with a step of 5°, which gave sufficient «smoothness» of the graphs.

A whole set of characteristics calculated for $U_s = \text{const}$, which may be of interest to inductor developers, is shown in Fig. 5-8. The essence of the characteristics is manifested by specific values, which are indicated on the graphs.

The main input values for the inductor are the voltage of the stator winding and its current, the output value is the rotating EMT (10). Figure 5 summarizes the characteristics of such quantities, and, for comparison, the mode $I_s = \text{const}$ is added to the mode $U_s = \text{const}$, and the argument β is replaced by the load angle Θ – respectively, Fig. 6.

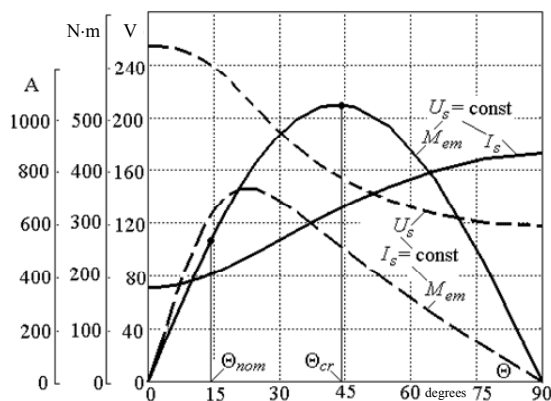


Fig. 5. Angular characteristics for calculation variants $U_s = \text{const}$ and $I_s = \text{const}$ and related changes in I_s and U_s

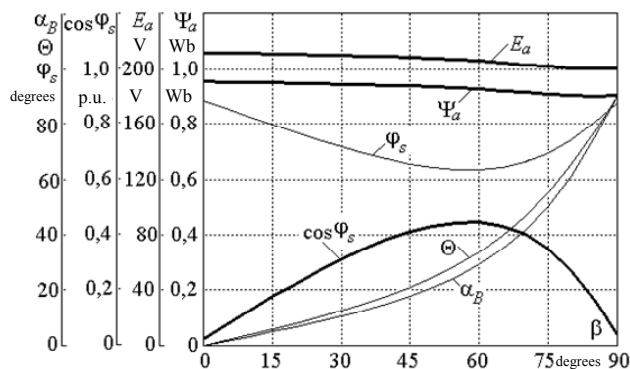


Fig. 6. Characteristics of magnetic flux linkage, EMF, phase relationships and power factor

In this way, the angular characteristic $M_{em}(\Theta)$, known in the theory of synchronous machines, was obtained for the inductor. And in this case, such a characteristic for the mode $U_s = \text{const}$ has a classical form – a half-wave of a sine wave of double frequency, which is typical for synchronous reluctance motors.

It can be noted that the mode $U_s = \text{const}$ is more effective from the point of view of obtaining EMT, which should ensure the implementation of the technological process of processing substances. This reinforces the mentioned advantage of this mode – the absence of a voltage regulator, and the necessary current will be set

based on the self-regulation property of the inductor inherent in electric motors.

Note that in Fig. 5 at the initial ($\beta = 0$) and final ($\beta = 90^\circ$) points, the EMT is zero, i.e., here the idle mode imagined earlier a priori takes place. The values of angles β and Θ coincide only at these points (Fig. 6), and within the range, the angle Θ is smaller than β .

The maximum EMT (Fig. 5) was obtained at a critical load angle Θ_{cr} equal to 44.5°, and this in Fig. 6 corresponds to the angle $\beta = 67^\circ$. In the range of the angle Θ from 0 to Θ_{cr} , according to the theory of synchronous electric machines, the operation of the inductor is stable. For a twofold margin in torque, it can be taken from Fig. 5 as a nominal load angle Θ_{nom} equal to 14°, and it in Fig. 6 corresponds to the angle $\beta = 33^\circ$.

In Fig. 5, 6 it is revealed that from $\beta = 0$ (idle mode) to the angle $\beta = 33^\circ$ current, MFL, EMF are quite stable. Further, an increase in load leads to a significant increase in current, which is accompanied by a corresponding increase in EMT and a certain decrease in EMF and MFL included in (6) and (7). Due to the stability of the MFL, the magnetic losses are stable, and the electric losses (14) increase along with the current (Fig. 7).

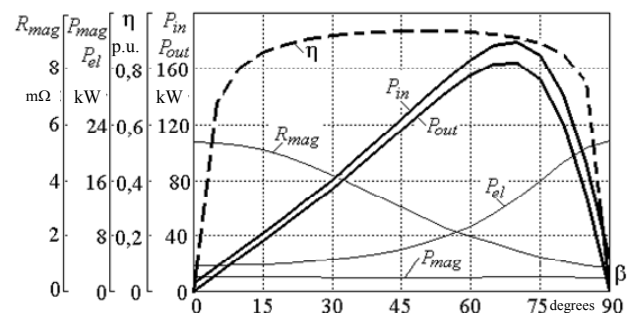


Fig. 7. Characteristics of the input and output powers of the inductor and its power losses, efficiency and active resistance taking into account magnetic losses

The powers in the mechanical (11) P_{out} (Fig. 7) and electrical (12) expressions were identical. This can be considered a check of the adequacy of the phase relationships of the considered electrical quantities. Note that the graph of the EMT function $M_{em}(\beta)$ is similar in shape to the graph of these powers in Fig. 5, which is natural in view of their connection according to (11).

The graphs of the characteristics of the efficiency (Fig. 7) η and the power factor $\cos \phi_s$ (Fig. 6) show their increase with increasing load of the inductor. In the range of stable operation, the efficiency level corresponds to electric machines of small and medium power. At the same time, the level of $\cos \phi_s$ values is very low, and this is explained by the increased magnetizing component of the stator winding current due to the low-magnetic medium of the working chamber and significant air gap.

Figure 8 shows the functions of changing the magnetic flux density at points 0, a and b, marked in Fig. 3. Firstly, the proximity of the values of magnetic flux density in different places of the chamber is visible, and secondly, their stability in the operating range of the load of the inductor.

By comparing the characteristics of the inductor in the operation mode calculated here at $U_s = \text{const}$, and the mode presented in [7] at $I_s = \text{const}$, one can identify certain advantages and disadvantages of each of them.

From the point of view of such important characteristics as power factor and efficiency, the operation modes of the inductor $U_s = \text{const}$ and $I_s = \text{const}$ turned out to be almost equivalent.

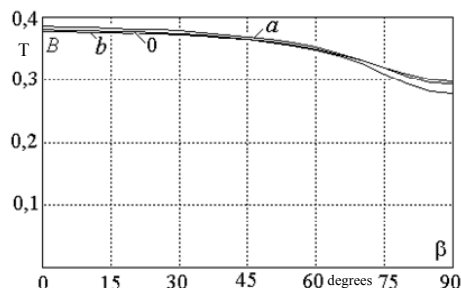


Fig. 8. Magnetic flux density B characteristics at certain points of the working chamber of the inductor

Another important requirement for «processors» of various substances is the uniformity and stability of magnetic flux density in the working area, while working in the mode $U_s = \text{const}$ it is provided much better.

Conclusions.

1. The developed technique based on numerical calculations of magnetic fields allows to organize an iterative process for the calculation analysis of the characteristics of an inductor operating with a changing load with a stable supply voltage of its winding.

2. For a test sample of the inductor, when operating in the load mode with the condition of stabilizing the voltage of its winding, the electric, magnetic and energy parameters, as well as phase (angular) relationships of the operation quantities are calculated and presented. Their interconnections made it possible to form a family of characteristics with an argument – a phase shift of the MMF of the stator winding in relation to the longitudinal axis of its working chamber.

3. In view of the simultaneous calculation of a number of parameters of the inductor, one can also obtain a variety of its characteristics by choosing any of these parameters instead of the argument β .

4. A comparison is made of the angular characteristics of the inductor, calculated by methods that provide stabilization of the voltage or current of the stator winding. More rational for the operation of the inductor is the voltage stabilization mode, which in the desired operating

range of the load angle up to 25° provides its best and electrical, magnetic, force and energy parameters.

REFERENCES

1. Chen L., Yang R., Zeng J., Shao Y., Xiao Q., Guo S. A wet belt permanent high gradient magnetic separator for purification of non-metallic ores. *International Journal of Mineral Processing*, 2016, vol. 153, pp. 66-70. doi: 10.1016/j.minpro.2016.06.004.
2. Ge W., Encinas A., Araujo E., Song S. Magnetic matrices used in high gradient magnetic separation (HGMS): A review. *Results in Physics*, 2017, vol. 7, pp. 4278-4286. doi: 10.1016/j.rinp.2017.10.055.
3. Wang Y., Gao D., Zheng X., Lu D., Li X. Rapid determination of the magnetization state of elliptic cross-section matrices for high gradient magnetic separation. *Powder Technology*, 2018, vol. 339, pp. 139-148. doi: 10.1016/j.powtec.2018.08.012.
4. Altun G., Inal S., Ibrahim A.L.P. Recovery of chromite from processing plant tailing by vertical ring and pulsating high gradient magnetic separation. *MT Bilimsel*, 2018, vol. 13, pp. 23-35.
5. Gerasimov M.D., Loktionov I.O. Dual-use technological solutions. Application prospects. *Vektor GeoNauk*, 2019, vol. 2, no. 1, pp. 19-26. doi: 10.24411/2619-0761-2019-10003.
6. Milykh V.I., Shilkova L.V. Experimental research of the three-phase physical model of the magnetic field inductor in the working mode when processing bulk material. *Bulletin of NTU «KhPI». Series: «Electric machines and electromechanical energy conversion»*, 2020, no.3(1357), pp. 3-7. (Ukr). doi: 10.20998/2409-9295.2020.3.01.
7. Milykh V.I., Shilkova L.V. Numerical-field analysis of the characteristics of a three-phase magnetic field inductor for the treatment of various substances with current stabilization. *Electrical engineering & electromechanics*, 2019, no. 6, pp. 21-28. doi: 10.20998/2074-272X.2019.6.03.
8. *Finite Element Method Magnetics: OldVersions*. FEMM 4.2 11Oct2010 Self-Installing Executable. Available at: <http://www.femm.info/wiki/OldVersions> (accessed 15.06.2017).
9. Milykh V.I. The system of automated formation of electrical machines computational models for the FEMM software environment. *Technical Electrodynamics*, 2018, no.4, pp. 74-78. (Ukr.) doi: 10.15407/techned2018.04.074.

Received 02.01.2020

V.I. Milykh¹, Doctor of Technical Science, Professor,
L.V. Shilkova¹, Postgraduate Student,
¹National Technical University «Kharkiv Polytechnic Institute»,
2, Kyrpychova Str., Kharkiv, 61002, Ukraine,
e-mail: mvikemkpi@gmail.com, larisa_lv@ukr.net

How to cite this article:

Milykh V.I., Shilkova L.V. Characteristics of a cylindrical inductor of a rotating magnetic field for technological purposes when it is powered from the mains at a given voltage. *Electrical engineering & electromechanics*, 2020, no.2, pp. 13-19. doi: 10.20998/2074-272X.2020.2.02.

V.A. Prakht, V.A. Dmitrievskii, V.M. Kazakbaev, S.Kh. Oshurbekov

COMPARATIVE ANALYSIS OF TWO HIGH-SPEED SINGLE-PHASE ELECTRICAL MACHINES WITH PERMANENT MAGNETS ON THE STATOR

Purpose. Single-phase machines with permanent magnets on the rotor are widely used in a variety of applications of a low rated power. When these machines are applied in high-speed applications, a retaining ring on the rotor core must be often used. However, it makes the assembly more complex and the high-speed machines become more expensive. On the other hand, machines with magnets on the stator still can be a valuable alternative due to their simple and reliable rotor design. In this paper the comparative study of performances of two single-phase electrical machines with magnets on the stator (flux reversal electrical machine and hybrid switched reluctance machine) is presented. The following performances have been compared: efficiency, weight, active materials cost, value of rated current of switches of the frequency converter. *Methodology.* Calculation of electrical machines performances using solving two-dimension boundary magnetostatics problems. *Results.* The theoretical comparison of the flux reversal electrical machine and the hybrid switched reluctance machine has been carried out; the comparison on specific torque and efficiency of the two aforementioned machines have been obtained. The flux reversal machine has a significantly higher efficiency and a fewer weight. In addition, it has a lower value of rated current. On the contrary, the cost of active materials of the hybrid switched reluctance one is much less. *Originality.* The presented results can assist in selecting the best design alternative of electrical machines in the following applications: electrical blowers, household appliances, fans, pumps and compressors of a low rated power etc. *Practical value.* The comparisons results of the flux reversal electrical machine and the hybrid switched reluctance machine has been obtained for the first time. References 15, tables 2, figures 13.

Key words: high speed machines, hybrid switched reluctance machine, flux reversal electrical machine, permanent magnet machine, single-phase electrical machine, special electrical machine.

Мета. Дослідження характеристик двох високошвидкісних однофазних електричних машин з магнітами на статорі (електрична машина зі змінним напрямом потоку і гібридна вентиляльно-індукторна реактивна машина): порівнюються такі характеристики як ККД, вага, вартість активних матеріалів, номінальний струм елементів перетворювача частоти. *Методика.* Розрахунок характеристик електричної машини за допомогою рішення двовірних крайових магнітостатичних завдань. *Результати.* Проведено порівняння двох типів однофазних машин з магнітами на статорі; отримано розрахункове порівняння характеристик однофазної електричної машини зі змінним напрямом потоку і однофазної гібридної вентиляльно-індукторної реактивної машини; отримані результати порівняння маси, розмірів і ККД двох машин. *Наукова новизна.* Уперше отримані результати порівняння однофазної електричної машини зі змінним напрямом потоку і однофазної гібридної вентиляльно-індукторної реактивної машини. *Практичне значення.* Отримані результати можуть допомогти при виборі кращої конструкції електродвигуна в даних застосуваннях: електричне турбонаддування, побутові прилади, вентилятори, насоси і компресори малої потужності і т.д. Бібл. 15, табл. 2, рис. 13.

Ключові слова: високошвидкісні машини, гібридна вентиляльно-індукторна реактивна машина, машина зі змінним напрямом магнітного потоку, машина з постійними магнітами, однофазні електричні машини, спеціальні електричні машини.

Цель. Исследование характеристик двух высокоскоростных однофазных электрических машин с магнитами на статоре (электрическая машина с переменным направлением потока и гибридная вентиляльно-индукторная реактивная машина): сравниваются такие характеристики как КПД, вес, стоимость активных материалов, номинальный ток элементов преобразователя частоты. *Методика.* Расчет характеристик электрической машины с помощью решения двумерных крайовых магнитостатических задач. *Результаты.* Произведено сопоставление двух типов однофазных машин с магнитами на статоре; получено расчетное сравнение характеристик однофазной электрической машины с переменным направлением потока и однофазной гибридной вентиляльно-индукторной реактивной машины; получены результаты сравнения массы и размеров КПД двух машин. *Научная новизна.* Впервые получены результаты сравнения однофазной электрической машины с переменным направлением потока и однофазной гибридной вентиляльно-индукторной реактивной машины. *Практическое значение.* Полученные результаты могут помочь при выборе лучшей конструкцией электродвигателя в рассматриваемых приложениях: электрический турбонаддув, бытовые приборы, вентиляторы, насосы и компрессоры малой мощности и т.д. Библ. 15, табл. 2, рис. 13.

Ключевые слова: высокоскоростные машины, гибридная вентиляльно-индукторная реактивная машина, машина с переменным направлением магнитного потока, машина с постоянными магнитами, однофазные электрические машины, специальные электрические машины.

Introduction. Single-phase synchronous machines with magnets on the rotor [1] and brushless machines with permanent magnets on the stator [2-9] are used in high-speed low power applications where speed control and low cost are required.

The main advantage of machines with magnets on the rotor compared to a synchronous machine with magnets on the rotor is a simple toothed rotor, which is a

laminated steel package mounted on a shaft. This improves reliability, simplifies rotor manufacturing technology, and reduces rotor cost in high-speed applications.

In [2, 3], a single-phase hybrid switched reluctance machine (HSRM) is described (Fig. 1). Adding permanent magnets to the stator solves the problem of initial

© V.A. Prakht, V.A. Dmitrievskii, V.M. Kazakbaev, S.Kh. Oshurbekov

positioning of the rotor. Therefore, starting the motor is possible, even in a single-phase version. In addition, the presence of magnets on the stator reduces the mass of HSRM, compared with HSRM without magnets. The size and diameter of the HSRM rotor are reduced, which is especially important for high-speed applications. Compared to a single-phase synchronous machine with magnets on the rotor, HSRM has the following advantages:

- 1) structurally simple and reliable gear rotor;
- 2) cheap ferrites can be used in the HSRM design, and expensive rare-earth magnets should be used in a traditional synchronous machine;
- 3) fewer transistors in the inverter.

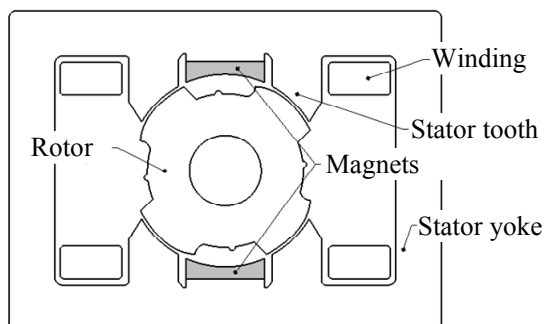


Fig. 1. A single-phase hybrid switched reluctance machine [2]

Despite the advantages of HSRM noted above, this machine has the following disadvantage compared to a single-phase synchronous machine with magnets on the rotor: HSRM is powered by unipolar DC pulses. A synchronous machine with magnets on the rotor is an AC machine. Therefore, in order to achieve a current with the same amplitude (half-span) in the case of HSRM, it is required that the current has a significantly higher modulus value. Thus, the effective and maximum currents in the HSRM phase are much larger than that of a similar single-phase synchronous machine with magnets on the rotor. In this regard, the cost and dimensions of the frequency converter for HSRM increase, as well as the losses in the frequency converter increase.

A good alternative to HSRM and a traditional single-phase synchronous machine with magnets on the rotor can be a flux reversal machine (FRM). A single-phase FRM with three teeth on the rotor and four magnetic poles on the stator (Fig. 2) was first described in [4].

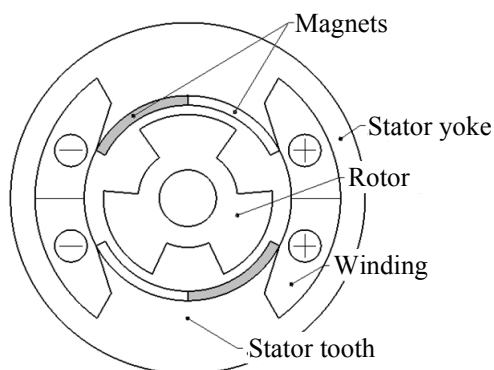


Fig. 2. FRM design according to [4]

A single-phase FRM has a simple and toothed rotor, like HSRM. The placement of permanent magnets on the FRM stator provides simplicity of design and reliability, as well as low weight and dimensions. At the same time, FRM is an AC machine, like a synchronous machine with magnets on the rotor. Current pulses of different polarity in FRM can occupy a significant part of the period. Therefore, the effective and maximum currents in the FRM phase are less than for HSRM. This makes it possible to use a frequency converter for FRM, in which the main power elements have lower value of the effective and maximum currents. Also, in the frequency converter for FRM, there are less energy losses than for HSRM, and, therefore, the dimensions of the radiator and the overall dimensions are smaller.

However, the FRM design described in [4] has the following disadvantages: 1) a decrease in specific power and efficiency, since a third of the inner surface of the stator is not used; 2) the lack of symmetry of the machine at a rotation interval of 180° causes uncompensated radial forces acting on the rotor; 3) these uncompensated radial forces reduce the service life of the bearings. To overcome the above disadvantages of FRM described in [4], in the patent [5] and papers [6, 7], a single-phase FRM presented in Fig. 3 is proposed.

In FRM (Fig. 3) the entire stator surface is used due to the use of half-closed slots. The HSRM has open stator slots, which reduces the specific torque and efficiency in comparison with FRM.

Despite the drawbacks of HSRM noted above, compared with FRM, cheap ferrite magnets can be used in the design of HSRM [3], while only rare-earth magnets can be used for FRM. This advantage of HSRM can be especially important when designing low-cost drives for household appliances, electrical tools, the automotive industry, blowers, etc.

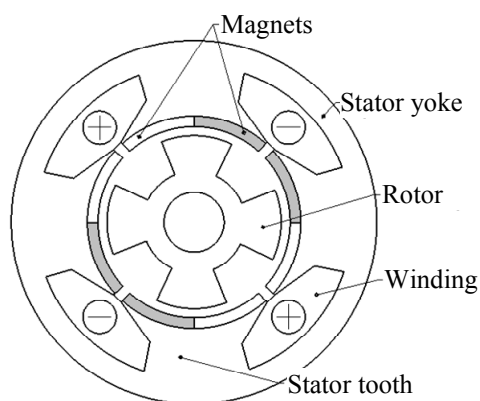


Fig. 3. FRM design according to [5, 6]

Comparison of different types of electric machines by weight and cost of active materials, efficiency is of great importance when choosing the type of drive for various applications, as shown in the example of three-phase machines [10-12]. As a review of the literature shows, a comparison of high-speed FRM and HSRM is not described in the literature, therefore, such a comparison is relevant and new when choosing the type of drive for single-phase high-speed applications.

The goal of the work is study of the characteristics of two types of single-phase high-speed electric machines with magnets on the stator – FRM and HSRM. Both machines are designed for low-power drives of household appliances (rated mechanical power 754 W, rated speed 18000 rpm, rated torque 0.4 N·m). The main characteristics and data for the HSRM are taken from [2]. The FRM was designed based on the technique described in [8]. For both machines, a comparison is made according to the efficiency and the mass of active materials. The advantages and disadvantages of single-phase FRM and HSRM are analyzed.

Modelling and calculation of FRM characteristics.

The modelling and calculation of the characteristics of the FRM was performed using the Finite Element Method based on the technique described in [9]. The technique is based on the solution of magnetostatic boundary value problems, with different positions of the rotor corresponding to different times. All these boundary value problems have the same computational domain, divided into two subdomains in the middle of the air gap. The rotation is taken into account by the boundary condition stitching these subdomains in accordance with the rotation of the rotor [6]. The diameter of the FRM stator package was chosen significantly less than that of the HSRM and equal to 51 mm. The length of the package was chosen equal to 30 mm, as in HSRM. Rare-earth magnets with magnetic flux density of 1.2 T were selected for FRM. The frequency of supply of the fundamental harmonic of the FRM current is equal to 1200 Hz, as for HSRM.

Figure 4 shows the distribution of the magnetic flux density module for FRM. The rotor tooth is located above the middle of the stator slot.

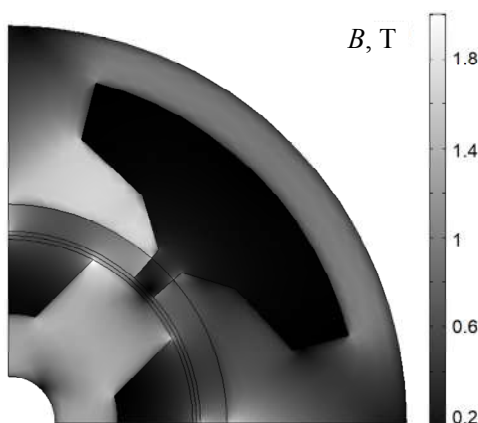


Fig. 4. Magnetic flux density module for FRM at torque of 0.4 N·m

In Fig. 5,a, the calculated losses in copper P_{cu} , magnetic cores of the stator P_{st} and rotor P_{rt} , as well as in magnets P_{magn} are shown for FRM for the rated speed (18000 rpm) at different values of the load torque:

- 1) mechanical power 188.5 W, torque 0.1 N·m;
- 2) mechanical power 377 W, torque 0.2 N·m;
- 3) mechanical power 565 W, torque 0.3 N·m;
- 4) mechanical power 754 W, torque 0.4 N·m (nominal mode).

Other losses (in bearings and ventilation) were assumed to be 15 W at rated speed. The largest losses of FRM in all modes are concentrated in the winding.

Figure 5,b shows the instantaneous values of FRM currents for different values of the torque. The moments of the beginning and end of a positive voltage pulse are indicated by «on+» and «off+», respectively. The moments of the beginning and end of a negative voltage pulse are indicated by «on-» and «off-», respectively. The graphs show that the current is piecewise smooth with kinks at the moments of switching.

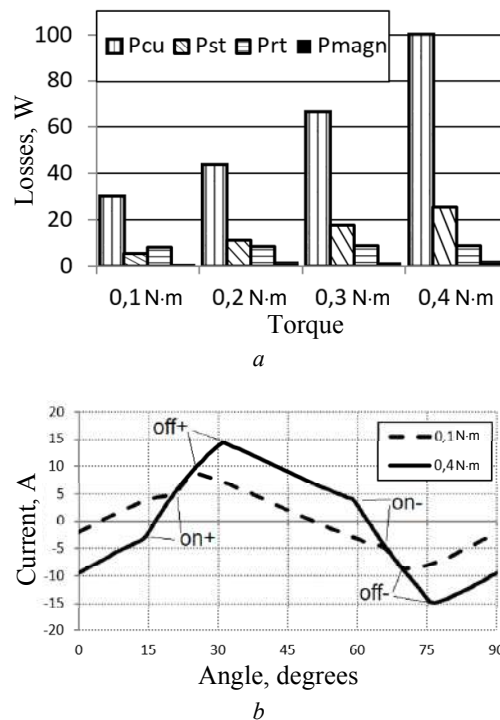


Fig. 5. Losses of FRM at the rated speed at various load torques (a) and the dependence of the current on the position of the rotor (b)

Figure 6,a shows the dependence of the fill factor of the supply voltage pulses (the fraction of the electric period occupied by voltage pulses of one or another polarity) on the average value of the FRM torque. With an increase in the required torque value, the fill factor increases linearly. The dependence of the effective current value on the average torque of the FRM is shown in Fig. 6,b. The effective value of the current increases nonlinearly with increasing torque. The remaining characteristics for FRM are presented in the next section, in comparison with HSRM.

Comparison of the characteristics of FRM and HSRM. Tables 1, 2 show the main characteristics of single-phase FRM and HSRM (rated mechanical power 754 W, rated speed 18000 rpm).

The price per 1 kg of permanent magnets depends not only on the material, but also on the size of the blocks used [13, 14]. The price of NeFeB-magnets of the required size for FRM is 137.78 USD/kg [13]. The price of ferrite magnets of the required size for HSRM is 67.20 USD/kg [14].

As can be seen from Table 2, the cost of active materials for HSRM is 1.9 times less than for FRM. However, FRM is 1.8 times less in mass than HSRM. Therefore, in devices that the user holds in his/her hands (for example, in an angle grinder, in a circular saw, in a

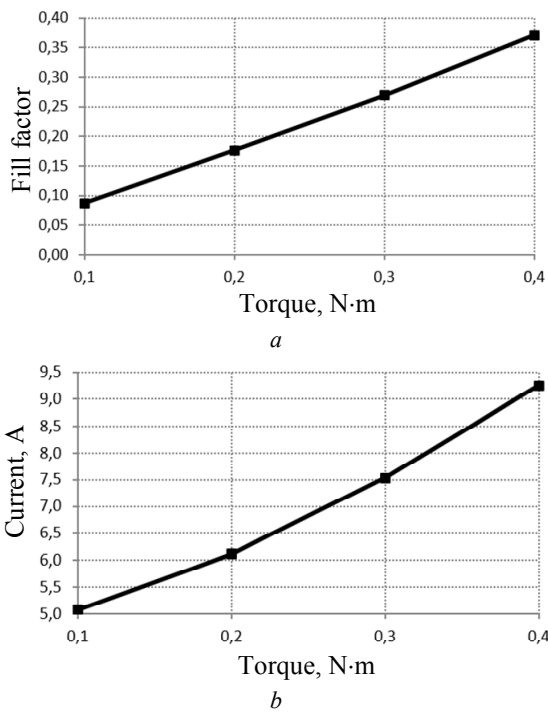


Fig. 6. Dependence of the fill factor (a) and the effective current value (b) on the torque of FRM

cordless power tool, in a garden blower, in a handheld vacuum cleaner), as well as in other applications where it is important to reduce the dimensions, it is advisable to use FRM. In applications where weight reduction is not so important, but it is important to reduce the cost of the machine, for example, in hand dryers, in a blender, in a miter saw, it is advisable to use HSRM.

Table 1

Rated parameters of electrical machines

Parameter	FRM	HSRM [2]
Load torque, N·m	0.4	0.4
Fundamental harmonic frequency, Hz	1200	1200
DC link voltage, V	320	320
Effective value of current in phase, A	9.25	17.8
Maximum value of current in phase, A	14.8	34.8
Efficiency, %	83	72

The size of the FRM rotor is significantly smaller than that of the HSRM: 1) the diameter of the rotor is 1.4 times smaller; 2) the mass of the rotor is 2.3 times less; 3) the moment of inertia of the rotor is 5 times less. This advantage of FRM is especially important for all high-speed applications, since it allows to significantly reduce the centrifugal forces acting on the rotor, as well as reduce the load on the rotor bearing assembly and extend the service life. Also, the small moment of inertia of the rotor is very important in applications such as electric turbocharging [15], since it allows increasing the reaction speed to the reference signal and significantly improving the dynamic characteristics of turbocharging systems of gasoline and diesel internal combustion engines.

Table 2

Cost of active materials, weight and size of electrical machines

Parameter	FRM	HSRM [2]
External dimension of stator magnetic circuit, mm	Ø 51	78×58
Active part length, mm	30	30
Air gap, mm	0.5	0.5 – 1.2
Rotor outer diameter, mm	23.6	≈ 34
Rotor moment of inertia, kg·cm ²	0.041	0.205
Permanent magnet type	Rare-earth	Ferrite*
Permanent magnet thickness, mm	1.7	2.4
Mass of permanent magnets, g	28	17
Mass of stator steel, g	214	494
Mass of rotor steel, g	61	138
Mass of copper, g	100	99
Total mass of active materials, g	403	731
Cost of active materials, USD	4.83	2.47

* Note to Table 2: in the paper [5] there is no data on the type of magnets in the HSRM, however, in [3] it is noted that ferrite magnets are used for the HSRM. When calculating the cost of active materials, the following prices were taken: 1 USD/kg for steel, 7 USD/kg for copper [10].

Figure 7 presents the values of the efficiency of FRM and HSRM for rotation speed of 18000 rpm. The FRM has a higher value of efficiency, which means less losses, less heating of the winding and a longer mode of operation during overloads in torque and power.

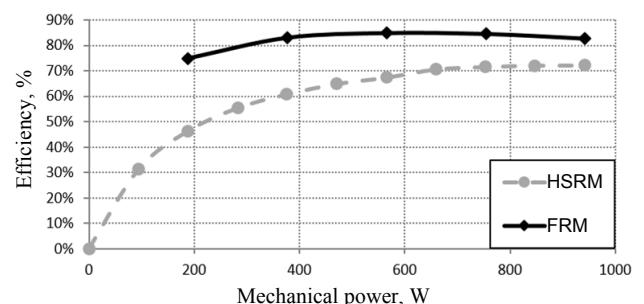


Fig. 7. Comparison of the FRM and HSRM efficiency

Figure 8 shows the torque values of the FRM and HSRM depending on the angle of rotation of the machine. The torque of FRM has a region of negative values and a higher value of torque pulsations, in comparison with HSRM. However, the pulsations of the FRM torque can be significantly reduced as a result of optimizing the geometry of the machine and can be comparable with HSRM.

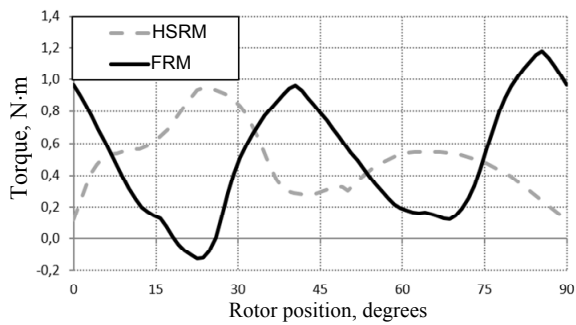


Fig. 8. Comparison of the graphs of the torque of the considered machines

Figures 9-11 show instantaneous values of voltage, currents, and power of FRM and HSRM for torque of 0.4 N·m and rotation speed of 18000 rpm.

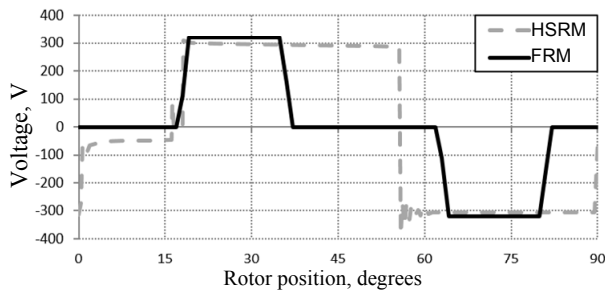


Fig. 9. Comparison of machine voltage graphs at torque of 0.4 N·m

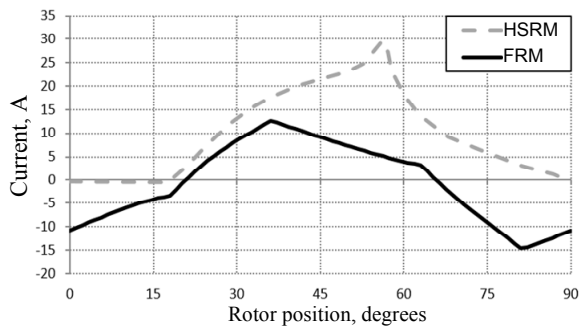


Fig. 10. Comparison of machine current graphs at torque of 0.4 N·m

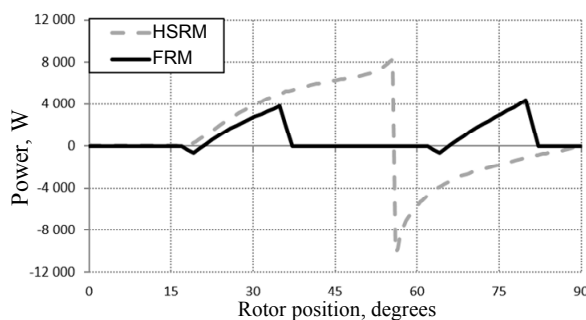


Fig. 11. Comparison of machine electrical power at torque of 0.4 N·m

As can be seen from Fig. 9-11, the maximum current value in the FRM phase is 14.8 A, and for HSRM – 34.8 A. The effective current value in the FRM phase is 9.25 A, and for HSRM – 17.8 A. The maximum value of instantaneous power consumption of the FRM from the frequency converter is 4.4 kW, and for HSRM – 9.8 kW.

The average value of the instantaneous power consumption of the FRM from the frequency converter is 908 W, and for HSRM – 1047 W. The frequency converter for the HSRM (Fig. 12) has a smaller number of transistors than for FRM (Fig. 13).

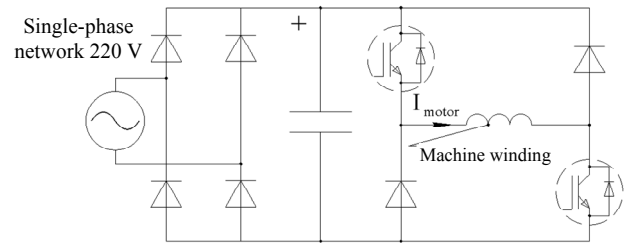


Fig. 12. Frequency converters for HSRM

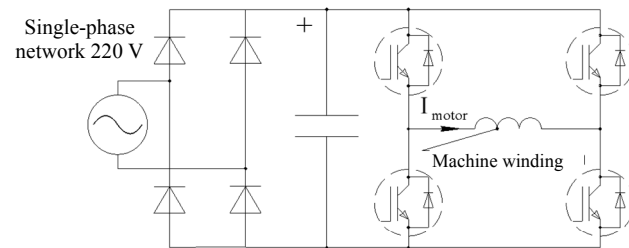


Fig. 13. Frequency converters for FRM

However, FRM requires power elements with a lower maximum current value and a smaller cooling radiator. Also, for HSRM, a capacitor of a larger capacity in the DC link is required, since the maximum value of the instantaneous power consumed by the inverter from the DC link is several times larger than for FRM. Therefore, it is of interest to compare the power losses, cost, mass, and size of frequency converters for FRM and HSRM. The design and comparison of frequency converters for FRM and HSRM will be performed in the further works.

Conclusions.

1. The paper compares two types of single-phase machines with magnets on the stator. The FRM has a significantly higher value of efficiency than HSRM, and, consequently, less heating of the winding.

2. The cost of active materials for the HSRM is 1.9 times less than for FRM. However, the FRM is 1.8 times less in mass than HSRM. Therefore, in devices that are held in hands, for example, in an electric tool, as well as in other applications where it is important to reduce the size, it is advisable to use FRM. In applications where weight reduction is not so important, but it is important to reduce the cost of the machine, it is advisable to use HSRM.

The effective current value in the FRM phase is 9.25 A, while the effective current value in the HSRM phase is 17.8 A. Therefore, the FRM needs power elements with a lower maximum current value and a smaller cooling radiator. The HSRM also requires a larger radiator and a larger capacitor in the DC link. Despite the simpler circuit of the frequency converter for HSRM, its mass will be greater than for FRM.

Acknowledgment.

The research was conducted as part of theme no. 8.9549.2017/8.9. within the frame of the government task

of the Ministry of Education and Science of the Russian Federation regarding R&D.

REFERENCES

1. Bentouati S., Zhu Z., Howe D. Permanent magnet brushless DC motors for consumer products. *Proceedings of the 9th International Conference on Electrical Machines and Drives* (Conf. Publ. No. 468), pp. 118-122, Canterbury, UK, 1-3 September 1999.
2. Jeong K., Ahn J. Design and characteristics analysis of a novel single-phase hybrid SRM for blender application. *Journal of Electrical Engineering and Technology*, 2018, vol. 13, no. 5, pp. 1996-2003. doi: **10.5370/JEET.2018.13.5.1996**.
3. Torok V., Loreth K. The world's simplest motor for variable speed control? The Cyrano motor, a PM-biased SR-motor of high torque density. *Proceedings of the 1993 5th European Conference on Power Electronics and Applications*, Brighton, UK, 13-16 Sept. 1993.
4. Deodhar R.P., Andersson S., Boldea I., Miller T.J.E. The flux-reversal machine: a new brushless doubly-salient permanent-magnet machine. *IEEE Transactions on Industry Applications*, 1997, vol. 33, no. 4, pp. 925-934. doi: **10.1109/28.605734**.
5. Dmitrievskii V.A., Prakht V.A. *Odnofaznaia elektricheskaya mashina* [Single-phase electrical machine]. Patent Russian Federation, no. 2524144, 2014. (Rus).
6. Dmitrievskii V., Prakht V., Pozdeev A., Klimarev V., Mikhailitsyn A. Angular grinder with new flux reversal motor. *Proceedings of the 18th International Conference on Electrical Machines and Systems (ICEMS)*, pp. 1366-1371, Pattaya, Thailand, 25-28 October 2015.
7. Dmitrievskii V.A., Prakht V.A. Mathematical simulation of a high-speed single-phase machine with alternating current direction. *Russian Electrical Engineering*, 2016, vol. 87, no. 6, pp. 327-332. doi: **10.3103/s1068371216060043**.
8. Dmitrievskii V., Prakht V., Kazakbaev V., Sarapulov S. Steady-state model of a single-phase flux reversal motor. *Proceedings of 58th International Scientific Conference on Power and Electrical Engineering of Riga Technical University (RTUCON 2017)*, pp. 1-5, Riga, Latvia, 12-13 October 2017.
9. Dmitrievskii V., Prakht V., Kazakbaev V., Sarapulov S. Optimal design of a high-speed single-phase flux reversal motor for vacuum cleaners. *Energies*, 2018, vol. 11, no. 12, p. 3334. doi: **10.3390/en11123334**.
10. Goss J., Popescu M., Staton D. A comparison of an interior permanent magnet and copper rotor induction motor in a hybrid electric vehicle application. *Electric Machines & Drives Conference (IEMDC)*, 2013 IEEE International, pp. 220-225, Chicago, IL, USA, 12-15 May 2013. doi: **10.1109/iemdc.2013.6556256**.
11. Rahman T., Mohammadi M.H., Humphries K., Lowther D.A. Comparison of fractional-slot concentrated winding and PM-assisted synchronous reluctance motors for class IV electric vehicles. *Proceedings of IEEE Int. Electrical Machines and Drives Conf. (IEMDC 2017)*, Miami, pp. 1-7, USA, May 2017. doi: **10.1109/iemdc.2017.8002173**.
12. Calvo E., Potoradi D. Synchronous reluctance motors with and without permanent magnets for high performance low cost electrical drives. *Proceedings of 5th International Electric Drives Production Conference (EDPC 2015)*, pp. 1-7, Nuremberg, Germany, 15-16 September 2015. doi: **10.1109/edpc.2015.7323220**.
13. ChenYang NdFeB Magnets. Price List of Standard Block Magnets. Available at: <http://www.ndfebmagets.de/CY-PriceList-NdFeB-Block.pdf> (accessed 05 July 2019).
14. IBSMagnet. Hard ferrite magnets. Available at: <https://ibsmagnet.com/products/dauermagnete/hartferrit.php> (accessed 05 July 2019).
15. Lee W., Kim J.H., Choi W., Sarlioglu B. Torque Ripple Minimization Control Technique of High-Speed Single-Phase Brushless DC Motor for Electric Turbocharger. *IEEE Transactions on Vehicular Technology*, 2018, vol. 67, no. 11, pp. 10357-10365. doi: **10.1109/tvt.2018.2866779**.

Received 24.09.2019

V.A. Prakht¹, Candidate of Technical Science,
V.A. Dmitrievskii¹, Candidate of Technical Science,
V.M. Kazakbaev¹, Candidate of Technical Science,
S.Kh. Oshurbekov¹,
¹Ural Federal University,
19, Mira Str., Ekaterinburg, 620002, Russia,
e-mail: va.prakht@urfu.ru, vladimir.dmitrievsky@urfu.ru,
vadim.kazakbaev@urfu.ru, s.oshurbekov@mail.ru

How to cite this article:

Prakht V.A., Dmitrievskii V.A., Kazakbaev V.M., Oshurbekov S.Kh. Comparative analysis of two high-speed single-phase electrical machines with permanent magnets on the stator. *Electrical engineering & electromechanics*, 2020, no.2, pp. 20-25. doi: **10.20998/2074-272X.2020.2.03**.

B.I. Kuznetsov, T.B. Nikitina, I.V. Bovdvi, S.V. Petrov, V.V. Kolomiets, B.B. Kobilyanskiy

ACTIVE SHIELDING OF MAGNETIC FIELD WITH CIRCULAR SPACE-TIME CHARACTERISTIC

Aim. The synthesis of two degree of freedom robust two circuit system of active shielding of magnetic field with circular space-time characteristic, generated by overhead power lines with «triangle» type of phase conductors arrangements for reducing the magnetic flux density to the sanitary standards level and to reducing the sensitivity of the system to plant parameters uncertainty. *Methodology.* The synthesis is based on the multi-criteria game decision, in which the payoff vector is calculated on the basis of the Maxwell equations quasi-stationary approximation solutions. The game decision is based on the stochastic particles multiswarm optimization algorithms. The initial parameters for the synthesis by system of active shielding are the location of the overhead power lines with respect to the shielding space, geometry and number of shielding coils, operating currents, as well as the size of the shielding space and magnetic flux density normative value, which should be achieved as a result of shielding. The objective of the synthesis is to determine their number, configuration, spatial arrangement and shielding coils currents, setting algorithm of the control systems as well as the resulting of the magnetic flux density value at the shielding space. *Results.* Computer simulation and field experimental research results of two degree of freedom robust two circuit system of active shielding of magnetic field, generated by overhead power lines with «triangle» type of phase conductors arrangements are given. The possibility of initial magnetic flux density level reducing and system sensitivity reducing to the plant parameters uncertainty is shown. *Originality.* For the first time the synthesis, theoretical and experimental research of two degree of freedom robust two-circuit system of active shielding of magnetic field generated by single-circuit overhead power line with phase conductors triangular arrangements carried out. *Practical value.* Practical recommendations from the point of view of the practical implementation on reasonable choice of the spatial arrangement of two shielding coils of robust two-circuit system of active shielding of the magnetic field with circular space-time characteristic generated by single-circuit overhead power line with phase conductors triangular arrangements are given. References 32, figures 17.

Key words: overhead power lines with «triangle» type of phase conductors arrangements, magnetic field, system of active shielding, Computer simulation, field experimental research.

Цель. Синтез комбинированной робастной двухконтурной системы активного экранирования магнитного поля с круговой пространственно-временной характеристикой, генерируемого одноконтурной воздушной линией электропередачи с треугольным подвесом проводов для снижения индукции магнитного поля до уровня санитарных норм и для снижения чувствительности системы к неопределенности параметров объекта управления. *Методология.* Синтез основан на решении многокритериальной стохастической игры, в которой векторный выигрыш вычисляется на основании решений уравнений Максвелла в квазистационарном приближении. Решение игры находится на основе алгоритмов стохастической мультиагентной оптимизации мультироем частиц. *Исходными параметрами* для синтеза системы активного экранирования являются расположение высоковольтной линии электропередачи по отношению к экранируемому пространству, геометрические размеры, количество проводов и рабочие токи линии электропередачи, а также размеры экранируемого пространства и нормативное значение индукции магнитного поля, которое должно быть достигнуто в результате экранирования. *Задачей синтеза* является определение количества, конфигурации, пространственного расположения и токов экранирующих обмоток, алгоритма работы системы управления, а также результирующего значения индукции магнитного поля в экранируемом пространстве. *Результаты.* Приводятся результаты теоретических и полевых экспериментальных исследований комбинированной робастной двухконтурной системы активного экранирования магнитного поля, генерируемого воздушной линией электропередачи с треугольным подвесом проводов. Показана возможность снижения уровня индукции исходного магнитного поля внутри экранируемого пространства и снижения чувствительности системы к неопределенностям параметров объекта управления. *Оригинальность.* Впервые проведены синтез, теоретические и экспериментальные исследования комбинированной робастной двухконтурной системы активного экранирования магнитного поля, генерируемого одноконтурной воздушной линией электропередачи с треугольным подвесом проводов. *Практическая ценность.* Приводятся практические рекомендации по обоснованному выбору с точки зрения практической реализации пространственного расположения двух экранирующих обмоток двухконтурной робастной системы активного экранирования магнитного поля с круговой пространственно-временной характеристикой, создаваемого одноконтурной воздушной линией электропередачи с треугольным подвесом проводов. Библи. 32, рис. 17.

Ключевые слова: воздушная линия электропередачи, подвес проводов типа «треугольник», магнитное поле, система активного экранирования, компьютерное моделирование, полевые экспериментальные исследования.

Introduction. Overhead power lines (OPL) are one of the most dangerous for people sources of technogenic power frequency (PF) of 50-60 Hz magnetic field (MF) [1, 2]. World Health Organization experts have identified the carcinogenic properties of the power frequency MF. Therefore, in the world over the past 15 years, sanitary standards are constantly tightening at the maximum permissible level of MF induction of 50-60 Hz. And

intensive research is being conducted on the development of methods for MF normalization [3-5].

Active contour shielding of PF MF generated by OPL [3, 4] is the most acceptable and economically feasible for ensuring the sanitary norms of Ukraine in the PF MF [1, 2]. The methods of synthesis of systems of active shielding (SAS) for MF, generate by OPL, developed in [6-11]. The initial data for the synthesis of

the system are the parameters of the transmission lines (working currents, geometry and number of wires, location of the transmission lines relative to the protected space) and the dimensions of the shielding space and magnetic flux density sanitary standards level, which should be achieved as a result of screening [12-22]. In the process of synthesis, it is necessary to determine the parameters of the shielding coils (SC) (their number, configuration, and spatial arrangement), currents and the resulting magnetic flux density level. To shielding factor improvement two degree of freedom SAS are used in which simultaneously used feed back regulator for closed loop control and feed forward regulator for open loop control [23-27].

Single-circuit OPL with horizontal and vertical bus arrangement, double-circuit OPL such as «barrel», «tree» and «inverted tree» [28], and groups of OPL generates a MF with a weak polarization. The space-time characteristics (STC) of such MF is a very elongated ellipse whose ellipse coefficient (ratio of the smaller axis to the larger axis) is seeks to zero. Single SC of single-circuit OPL generates MF, whose STC is a straight line. With such a single-circuit SAS with single SC, the major axis of the STS ellipse of the initial MF is compensated, so that the STS of the total MP with SAS is on is significantly smaller than the STS of the initial MF, which determines the high shielding factor of such single-circuit SAS. That is why using single-circuit SAS containing single SC can effectively shielded by MF with a small polarization. Exactly for such power lines, single-circuit SAS with single SC is most widely used in world practice [3].

However the single-circuit OPL with phase conductor's triangular arrangements generated most polarized MF. The STC of such MF is practically a circle. Therefore, for effective shielding of such MF it is necessary to have two SC at least [12]. Note that the vast majority of single-circuit OPL in Ukraine has just such phase conductors triangular arrangements.

As an example consider shielding of MF with circular STC generated by 110 kV OPL with phase conductors triangular arrangements in a single-story building located at a distance of 10 m from OPL. In Fig. 1 are shown location OPL, shielding space and shielding coils. The SAS contains two square shapes SC the spatial arrangement of which determine intuitively without SAS synthesis. In Fig. 1 also are shown this both SC. SC upper parts are coordinates (4.0, 4.0) and (8.0, 4.0). SC lower parts are coordinates (4.0, 0.0) and (8.0, 0.0). Figure 2 shows the picture of such shielding coils, the spatial arrangement of which was chosen without system synthesis. SC upper parts of both SC located at heights of 4.0 m from the ground, and the SC lower parts located at ground level.

It was assumed that, since both SC are orthogonal to each other and so such SC generate MF with STC, which also orthogonal to each other. Using such both SC you can get a high factor. However, with such SC spatial arrangement it is not possible to obtain high shielding factor. For shielding such MF with high shielding factor it is need to synthesize SAS.

The goal of this work is the synthesis of two degree of freedom robust two circuit system of active shielding of magnetic field with circular space-time characteristic, generated by overhead power lines with «triangle» type of phase conductors arrangements for reducing the magnetic flux density to the sanitary standards level and to reducing the sensitivity of the system to plant parameters uncertainty.

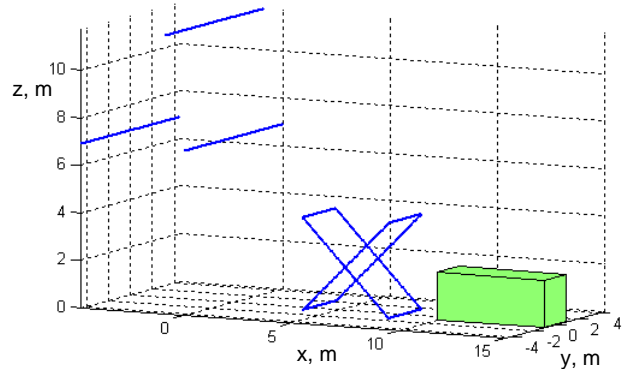


Fig. 1. The location of 110 kV overhead power line with phase conductors triangular arrangements, both shielding coils and shielding space



Fig. 2. Picture of the both shielding coil, the spatial arrangement of which were chosen without system synthesis

Problem statement. Two degree of freedom robust SAS synthesizing problem reduced [29] to the determination of such SC spatial arrangement and geometric sizes, as well as parameters of the regulator vector X and uncertainty parameters vector δ , which the maximum value of the magnetic flux density at points P_j of the shielding space P assumes a minimum value for the vector X but the maximum value for the vector δ . This technique corresponds to the standard worst-case robust systems synthesis approach [27, 29], when uncertainty parameters vector δ lead to the greatest deterioration in initial MF shielding created by OPL.

Parameters of the regulator vector of two degree of freedom robust SAS includes the parameters of the feed forward regulator in form amplitude and the phase vectors of the open loop control and the parameters of the feed back regulator in form gain vectors of the closed loop control.

This two degree of freedom robust SAS synthesizing problem formulated in multi-criteria game form [30-32] with vector payoff

$$B(X, \delta) = [B(X, \delta, P_1), B(X, \delta, P_2), \dots, B(X, \delta, P_m)]^T. \quad (1)$$

Components $B(X, \delta, P_i)$ are magnetic flux density in shielding space m points P_i . These components are nonlinear functions of the vectors X and δ calculated on basis of Maxwell equations quasi-stationary approximation solutions [5].

First player is vector X and its strategy vector payoff minimization. Second player is vector δ and this strategy is same vector payoff maximization [27, 29].

To find multi-criterion game solution from Pareto-optimal set solutions taking into account binary preference relations [30] used particle multi swarm optimization (PSO) algorithm [31], in which swarms number equal number of vector payoff components.

Computer simulation results. Consider the result of robust SAS synthesis of MF with circular space-time characteristic created by 110 kV OPL with phase conductors triangular arrangements in a single-story building located at a distance of 10 m from OPL. In Fig. 3 are shown location OPL, shielding coils and shielding space in which magnetic flux density level must mitigated to the Ukraine sanitary norms level.

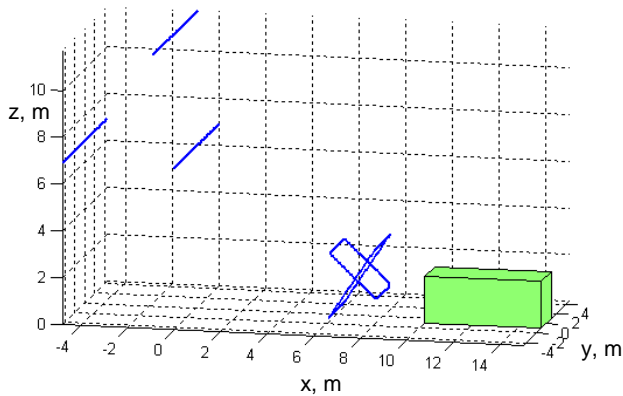


Fig. 3. The location of 110 kV overhead power line with phase conductors triangular arrangements, shielding coils and shielding space

For SAS synthesis in addition OPL geometric dimensions and shielding space the OPL bus currents values are necessary. Field experimental research of magnetic flux density level both in shielding space and near OPL carried out. In Fig. 4 are shown the isolines of the initial magnetic flux density generated by OPL with phase conductors triangular arrangements and with current of 250 A. The initial induction of the MF in shielding space is $0.8 \mu\text{T}$, which is 1.6 times higher than the sanitary norms.

Based on the obtained experimental data, the problem of OPL phase conductor's current identification solved. MF SAS synthesis results are two square shapes SC spatial arrangement.

In Fig. 3 also are shown this both SC. SC upper parts are coordinates (3.0416, 3.4965) and (7.1943, 3.6818). SC lower parts are coordinates (6.3707, 0.6637) and (2.8478, 2.4522).

So this both SC spatial arrangement obtained MF SAS synthesis results different from SC spatial arrangement obtained intuitively which shows in Fig. 1.

In Fig. 5 are shown the isolines of the resultant magnetic flux density with SAS is on.

As can be seen from this Fig. 5, minimum magnetic flux density value in the shielding space is $0.2 \mu\text{T}$. Initial magnetic flux density value generated by OPL in the shielding space is $0.75 \mu\text{T}$. Therefore, the SAS shielding factor maximum is more than 3.75 when the active shielding system is on, as can be seen from Fig. 3, magnetic flux density level in all shielding space does not exceed $0.3 \mu\text{T}$.

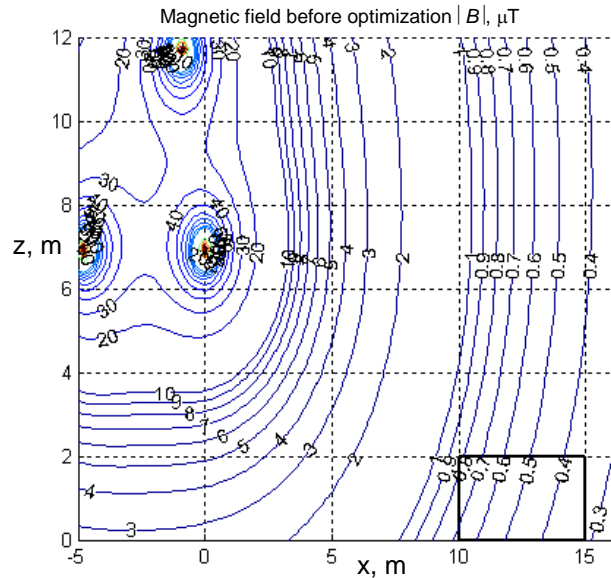


Fig. 4. Isolines of initial magnetic flux density generated by overhead power lines with phase conductors triangular arrangements

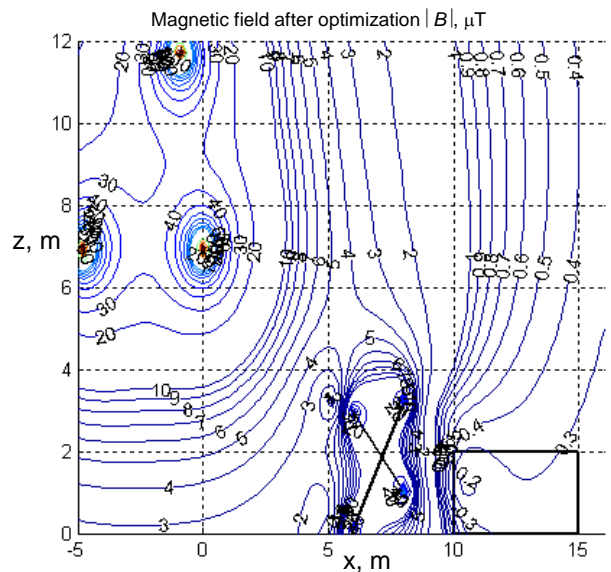


Fig. 5. Isolines of the resultant magnetic flux density with the system of active shielding is on

In Fig. 6 are shown the MF STC, generated by OPL (1); both SC (2) and total MF with SAS is on (3).

The STC of initial MF generated by OPL with phase conductors triangular arrangements close to the circle. STC of MF generated by both SC is also close to the circle of the STC of initial MF, which ensures high shielding factor.

However, STC of MF generated separately by only single first SC or only single second SC are straight lines. In Fig. 7 are shown comparison between MF STC

generated separately by only single first SC (1) and only single second SC (2).

Naturally, the STC of the resulting MF generated by OPL and only single SC is an ellipse, which will be shielded by another SC. In Fig. 8 are shown the STC of the initial MF generated by OPL, shielding MF generated by only single first SC and the resulting MF when only single first SC is used.

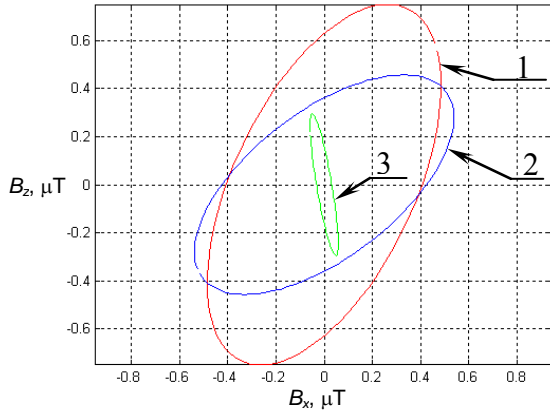


Fig. 6. Comparison of space-time characteristics of magnetic flux density between with and without system of active shielding and shielding coils

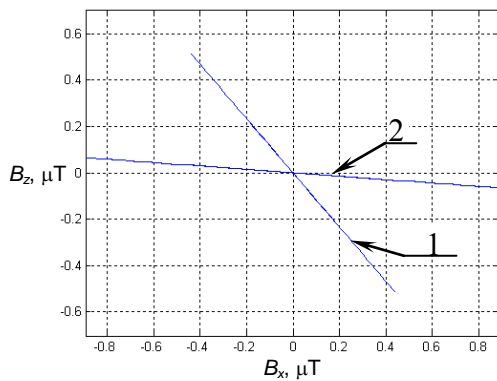


Fig. 7. Comparison between space-time characteristics of magnetic flux density generated separately by only single first (1) and by only single second (2) shielding coils

As can be seen from Fig. 8, the STC of the resulting MF is a strongly elongated ellipse, the semi-major axis of which is almost two times larger than the STC of the initial MF, and therefore, due to only single first SC work, initial MF is almost twice re compensated. However, then after second SC switching resulting MF STC becomes significantly less than the STC of initial MF, which ensures high shielding factor. Note that the STC of the resulting MF, left after the operation of only single first SC, practically parallel with the STC generated by the MF using only single second SC.

In Fig. 9 are shown the STC of the initial MF generated by OPL, shielding MF generated by only single second SC and the resulting MF when only single second SC is used.

Experimental research. Consider the experimental research of SAS model with two SC. Figure 10 shows picture of such two SC spatial arrangement. SC upper parts of SC located at heights of 3.5 m and 3.7 m from the ground, and the SC lower parts located at heights of 0.66 m and 2.5 m from the ground.

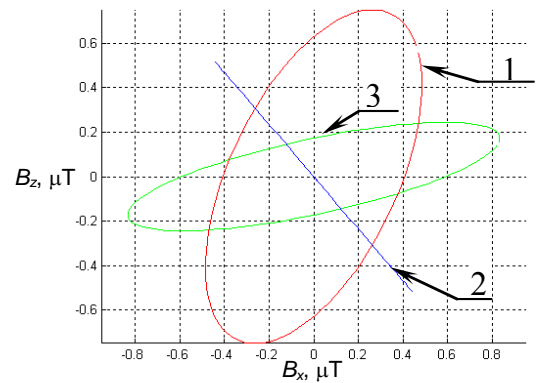


Fig. 8. Comparison between space-time characteristics of magnetic flux density without and with system of active shielding with only single first shielding coil and only single first shielding coil

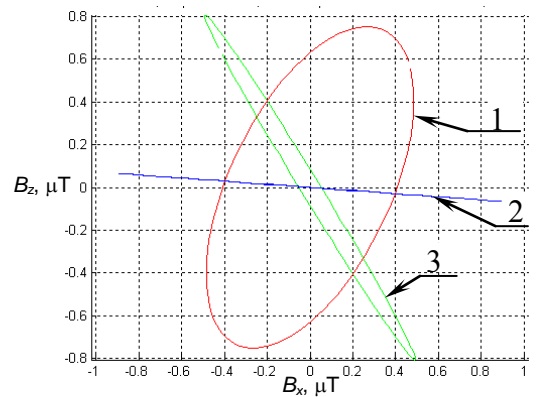


Fig. 9. Comparison between space-time characteristics of magnetic flux density without and with system of active shielding with only single second shielding coil and only single second shielding coil



Fig. 10. Picture of both shielding coil spatial arrangement of system of active shielding model

An important issue when setting up the two degree of freedom robust SAS is determining of spatial arrangement location points and spatial orientation of the MF sensors. For implementing of two degree of freedom robust SAS, two MF sensors must be placed in shielding space point with coordinates (10.6, 1.25), at which the calculated magnetic flux density value takes a minimum value. The MF both sensors axis must be parallel to the appropriate both SC MF STC lines. With this spatial orientation, both MF sensors measure the total MF generated by power lines and appropriate only single first

SC and only single second SC. In Fig. 11 are shown both MF sensors spatial arrangement in shielding space point for closed loop control by two degree of freedom robust SAS model.



Fig. 11. Picture of both magnetic field sensors spatial arrangement in shielding space point for closed loop control by system of active shielding model

For implementing of feed forward regulator for open loop control by two degree of freedom robust SAS, only single MF sensors must be placed outside shielding space point. In Fig. 12 is shown picture of such MF sensor spatial arrangement outside the shielding space for open loop control by SAS model.



Fig. 12. Picture of magnetic field sensor spatial arrangement outside the shielding space for open loop control by system of active shielding model

Both SC of the SAS model are square shape, contains 20 winds and powered by amplifiers TDA7294. The SAS contains an external magnetic flux density controller and an internal current controller. An inductive sensor used as an magnetic flux density sensor, and the magnetic flux density measurement is performed by magnetometer type EMF-828 of the firm LUTRON. In Fig. 13 are shown picture of system of active shielding model. SAS powered by autonomous generator. In Fig. 14 is shown picture of such autonomous generator.

In Fig. 15 are shown experimental isolines of the resultant magnetic flux density with SAS with only single first SC is on. In Fig. 16 are shown experimental isolines of the resultant magnetic flux density with SAS with only single second SC is on. Note that in spite of that MF STC with only the first and only the second SC is on are very different, as are shown in Fig. 8 and Fig. 9. But experimental isolines of the resultant magnetic flux density with only first and only second SC are very different, as are shown in Fig. 15 and Fig. 16 differ slightly.



Fig. 13. Picture of system of active shielding model



Fig. 14. Picture of autonomous generator powered by system of active shielding model

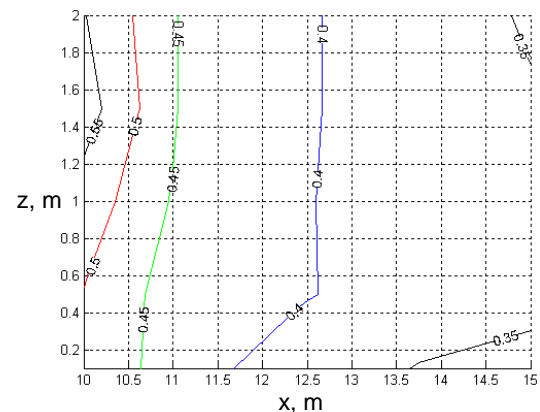


Fig. 15 Experimental isolines of the resultant magnetic flux density with SAS with only single first shielding coil is on

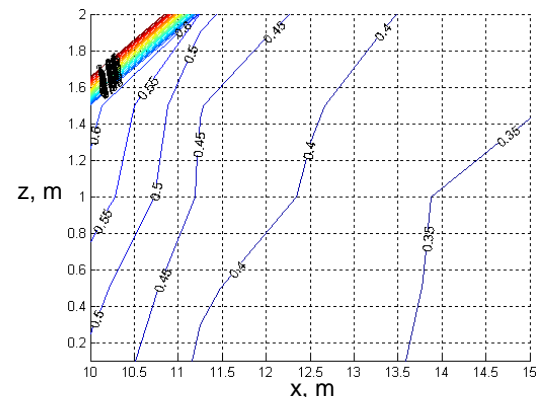


Fig. 16. Experimental isolines of the resultant magnetic flux density with SAS with only single second shielding coil is on

In Fig. 17 are shown comparison between magnetic flux density measurements and simulations with and without

SAS. Comparison between experimental and calculated results of magnetic flux density values in shielding zone shows that their spread does not exceed 20 %. The experimental shielding factor of SAS is also more than 2.5 units.

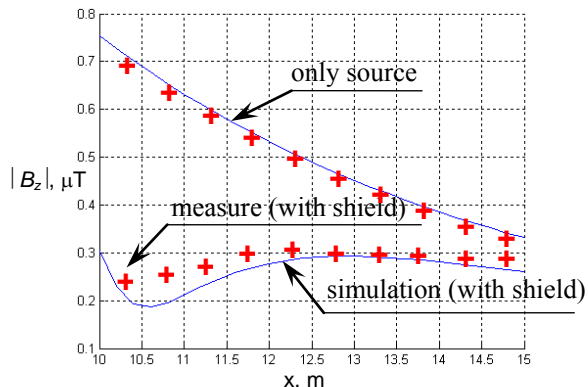


Fig. 17. Comparison of magnetic flux density between measurements and simulations with and without system of active shielding

Actually, the single-circuit 110 kV OPL with phase conductors triangular arrangements current are 200-500 A. SAS synthesis, computer simulation and field experimental given for OPL 250 A current. At this OPL current magnetic flux density level in all shielding space does not exceed 0.3 μT . Therefore such SAS provides Ukraine sanitary standards level 0.5 μT for OPL current up to 416 A. At this OPL current initial magnetic flux density level in shielding space is 1.25 μT , which is 2.5 times higher than Ukraine sanitary norms.

Conclusions.

1. For the first time the synthesis and field experimental research of two degree of freedom robust two-circuit system of active shielding of magnetic field with circular space-time characteristic, generated by overhead power lines with «triangle» type of phase conductors arrangements for reducing the initial magnetic flux density up to the sanitary standards level and reducing the sensitivity of the system to plant parameters uncertainty are given.

2. The synthesis is based on multi-criteria stochastic game decision, which is based on multiswarm stochastic multi-agent optimization from Pareto-optimal solutions. As a result the spatial position of two shielding coils and the parameters of the regulator are determined.

3. System reduce the the magnetic flux density in shielding space more than 2.5 times and has less to 20 % sensitivity to plant parameters uncertainty in comparison with the known systems.

4. Based on field experimental research of two degree of freedom robust two-circuit system of active shielding are shown that experimental and calculated magnetic flux density values in the shielding space spread does not exceed 20 %.

REFERENCES

1. Rozov V., Grinchenko V. Simulation and analysis of power frequency electromagnetic field in buildings closed to overhead lines. *2017 IEEE First Ukraine Conference on Electrical and Computer Engineering (UKRCON)*. Kyiv, Ukraine, pp. 500-503. doi: 10.1109/UKRCON.2017.8100538.

2. Rozov V.Yu., Grinchenko V.S., Yerisov A.V., Dobrodeyev P.N. Efficient shielding of three-phase cable line magnetic field by passive loop under limited thermal effect on power cables. *Electrical engineering & electromechanics*, 2019, no.6, pp. 50-54. doi: 10.20998/2074-272X.2019.6.07.

3. Active Magnetic Shielding (Field Cancellation). Available at: <http://www.emfservices.com/afcs.html> (accessed 10 September 2012).

4. Rozov V.Yu., Reutsky S.Yu., Pelevin D.Ye., Pylugina O.Yu. The magnetic field of transmission lines and the methods of its mitigation to a safe level. *Technical Electrodynamics*, 2013, no. 2, pp. 3-9. (Rus).

5. Rozov V.Yu., Reutsky S.Yu., Pylugina O.Yu. The method of calculation of the magnetic field of three-phase power lines. *Technical electrodynamics*, 2014, no.5, pp. 11-13. (Rus).

6. Salceanu A., Paulet M., Alistar B.D., Asiminesei O. Upon the contribution of image currents on the magnetic fields generated by overhead power lines. *2019 International Conference on Electromechanical and Energy Systems (SIELMEN)*. 2019. doi: 10.1109/sielmen.2019.8905880.

7. Bravo-Rodríguez J., Del-Pino-López J., Cruz-Romero P. A Survey on Optimization Techniques Applied to Magnetic Field Mitigation in Power Systems. *Energies*, 2019, vol.12, no.7, p. 1332. doi: 10.3390/en12071332.

8. Canova A., Giaccone L., Cirimele V. Active and passive shield for aerial power lines. *25th International Conference on Electricity Distribution Madrid*, 3-6 June 2019. Paper no. 1096, pp. 1-5.

9. Chorna O., Chorny O., Tytiuk V. Identification of changes in the parameters of induction motors during monitoring by measuring the induction of a magnetic field on the stator surface. *2019 IEEE International Conference on Modern Electrical and Energy Systems (MEES)*. Kremenchuk, 2019. doi: 10.1109/MEES.2019.8896554.

10. Chystiakov P., Chorny O., Zhautikov B., Sivyakova G. Remote control of electromechanical systems based on computer simulators. *2017 International Conference on Modern Electrical and Energy Systems (MEES)*. Nov. 2017. doi: 10.1109/mees.2017.8248934.

11. Shenkman A., Sonkin N., Kamensky V. Active protection from electromagnetic field hazards of a high voltage power line. *HAIIT Journal of Science and Engineering. Series B: Applied Sciences and Engineering*, Vol. 2, Issues 1-2, pp. 254-265.

12. Korol S., Buryan S., Pushkar M., Ostroverkhov M. Investigation the maximal values of flux and stator current of autonomous induction generator. *2017 IEEE First Ukraine Conference on Electrical and Computer Engineering (UKRCON)*, May 2017. doi: 10.1109/ukrcon.2017.8100302.

13. Ostroverkhov M., Buryk M. Control of permanent magnet synchronous motor under conditions of parametric uncertainty. *2019 IEEE International Conference on Modern Electrical and Energy Systems (MEES)*, Sep. 2019. doi: 10.1109/mees.2019.8896635.

14. Ostroverkhov M., Pyzhov V., Korol S. Control of the electric drive under conditions of parametric uncertainty and coordinates' interrelation. *2017 International Conference on Modern Electrical and Energy Systems (MEES)*, Nov 2017. doi: 10.1109/mees.2017.8248953.

15. Panchenko V.V., Maslii A.S., Pomazan D.P., Buriakovskiy S.G. Determination of pulsation factors of the system of suppression of interfering harmonics of a semiconductor converter. *Electrical engineering & electromechanics*, 2018, no.4, pp. 24-28. doi: 10.20998/2074-272X.2018.4.04.

16. Buriakovskiy S.G., Maslii A.S., Panchenko V.V., Pomazan D.P., Denis I.V. The research of the operation modes of the diesel locomotive CHME3 on the imitation model. *Electrical engineering & electromechanics*, 2018, no.2, pp. 59-62. doi: 10.20998/2074-272X.2018.2.10.

17. Buriakovskiy S., Maslii A., Maslii A. Determining parameters of electric drive of a sleeper-type turnout based on electromagnet and linear inductor electric motor. *Eastern-European Journal of Enterprise Technologies*, 2016, vol.4, no.1(82), pp. 32-41. (Rus). doi: **10.15587/1729-4061.2016.75860**.
18. Shchur I., Klymko V. Comparison of different types of electromechanical systems for creating of counter-rotating VAWT. *2017 IEEE First Ukraine Conf. on Electrical and Computer Engineering (UKRCON-2017)*, pp. 373-378. doi: **10.1109/ukrcon.2017.8100513**.
19. Shchur I. Impact of nonsinusoidalness on efficiency of alternative electricity generation systems. *2010 International School on Nonsinusoidal Currents and Compensation*, Lagow, 2010, pp. 218-223. doi: **10.1109/isncc.2010.5524483**.
20. Zagirnyak M., Bisikalo O., Chorna O., Chorny O. A model of the assessment of an induction motor condition and operation life, based on the measurement of the external magnetic field. *2018 IEEE 3rd International Conference on Intelligent Energy and Power Systems (IEPS)*. 2018. pp. 316-321. doi: **10.1109/ieps.2018.8559564**.
21. Zagirnyak M., Chorny O., Nykyforov V., Sakun O., Panchenko K. Experimental research of electromechanical and biological systems compatibility. *Przegląd Elektrotechniczny*, 2016, vol.1, no.1, pp. 130-133. doi: **10.15199/48.2016.01.31**.
22. Zagirnyak M., Serhienko S., Chorny O. Innovative technologies in laboratory workshop for students of technical specialties. *2017 IEEE First Ukraine Conference on Electrical and Computer Engineering (UKRCON)*, May 2017. doi: **10.1109/ukrcon.2017.8100446**.
23. Sushchenko O.A., Tunik A.A. Robust optimization of the inertially stabilized platforms. *2012 2nd International Conference «Methods and Systems of Navigation and Motion Control» (MSNMC)*, Kiev, 2012, pp. 101-105. doi: **10.1109/msnmc.2012.6475102**.
24. Sushchenko O.A. Robust control of angular motion of platform with payload based on H_∞ -synthesis. *Journal of Automation and Information Sciences*, 2016, vol. 48, no. 12, pp. 13-26. doi: **10.1615/jautomatinfscien.v48.i12.20**.
25. Sushchenko O.A. Robust control of platforms with instrumentation. *2019 IEEE 2nd Ukraine Conference on Electrical and Computer Engineering (UKRCON)*, Lviv, Ukraine, 2019, pp. 518-521. doi: **10.1109/ukrcon.2019.8879969**.
26. Zhiteckii L.S., Azarskov V.N., Solovchuk K.Y., Sushchenko O.A. Discrete-time robust steady-state control of nonlinear multivariable systems: a unified approach. *IFAC Proceedings Volumes*, 2014, vol. 47, no. 3, pp. 8140-8145. doi: **10.3182/20140824-6-za-1003.01985**.
27. Zhiteckii L.S., Solovchuk K.Y. Robust adaptive pseudoinverse model-based control of an uncertain SIMO memoryless system with bounded disturbances. *2019 IEEE 2nd Ukraine Conference on Electrical and Computer Engineering (UKRCON)*, Lviv, Ukraine, 2019, pp. 621-627. doi: **10.1109/ukrcon.2019.8879824**.
28. *Electrical installation regulations. 5th ed.* The Ministry of Energy and Coal Mining of Ukraine, 2014. 277 p. (Ukr).
29. Ren Z., Pham M.-T., Koh C.S. Robust Global Optimization of Electromagnetic Devices With Uncertain Design Parameters: Comparison of the Worst Case Optimization Methods and Multiobjective Optimization Approach Using Gradient Index. *IEEE Transactions on Magnetics*, 2013, vol.49, no.2, pp. 851-859. doi: **10.1109/tmag.2012.2212713**.
30. Galchenko V.Y., Yakimov A.N. A turmitobionic method for the solution of magnetic defectometry problems in structural-parametric optimization formulation. *Russian Journal of Nondestructive Testing*, 2014, vol.50, no.2, pp. 59-71. doi: **10.1134/s106183091402003x**.
31. Gal'chenko V.Y., Yakimov A.N., Ostapushchenko D.L. Pareto-optimal parametric synthesis of axisymmetric magnetic systems with allowance for nonlinear properties of the ferromagnet. *Technical Physics*, 2012, vol.57, no.7, pp. 893-899. doi: **10.1134/s1063784212070110**.
32. Ummels M. *Stochastic Multiplayer Games Theory and Algorithms*. Amsterdam University Press, 2010. 174 p.

Received 23.12.2019

B.I. Kuznetsov¹, Doctor of Technical Science, Professor,
T.B. Nikitina², Doctor of Technical Science, Professor,
I.V. Bovdii¹, Candidate of Technical Science,
S.V. Petrov¹,

V.V. Kolomiets², Candidate of Technical Sciences,
B.B. Kobilyanskiy², Candidate of Technical Sciences,

¹ State Institution «Institute of Technical Problems
of Magnetism of the NAS of Ukraine»,

19, Industrialna Str., Kharkiv, 61106, Ukraine,
phone +380 50 5766900,

e-mail: kuznetsov.boris.i@gmail.com

² Kharkov National Automobile and Highway University,
25, Yaroslava Mudroho Str., Kharkov, 61002, Ukraine,
e-mail: tatjana55555@gmail.com

How to cite this article:

Kuznetsov B.I., Nikitina T.B., Bovdii I.V., Petrov S.V., Kolomiets V.V., Kobilyanskiy B.B. Active shielding of magnetic field with circular space-time characteristic. *Electrical engineering & electromechanics*, 2020, no.2, pp. 26-32. doi: **10.20998/2074-272X.2020.2.04**.

M.I. Baranov, S.V. Rudakov

CALCULATION-EXPERIMENTAL DETERMINATION OF THE AVERAGE NUMBER OF QUANTIZED LONGITUDINAL ELECTRON DE BROGLIE HALF WAVES IN A CYLINDRICAL CONDUCTOR WITH PULSED AXIAL CURRENT

Purpose. Implementation of calculation-experimental determination of average number n_{0m} of the quantized longitudinal electron de Broglie half waves of length $\lambda_{e2m}/2$ in the metal cylindrical conductor with the pulsed axial current of high density. *Methodology.* Scientific bases of theoretical electrophysics and quantum physics, theoretical bases of the electrical engineering, electrophysics bases of technique of high-voltage and high pulsed currents. *Results.* The results of calculation-experimental estimations of average number n_{0m} of the quantized longitudinal electron de Broglie half waves in the round continuous zincked steel wire of radius 0.8mm and of length 320 mm with aperiodic pulsed axial current $i_0(t)$ of temporal shape 9 ms/160 ms of high density (at its amplitude of $\delta_{0m}=0.37$ kA/mm²). It is shown that in examined case the numeral value of the average quantized number from data of calculation and experiment makes $n_{0m}=9$, and test average length of quantized longitudinal electron de Broglie half waves in the indicated steel wire appears approximately equal to $\lambda_{e2m}/2 \approx 34$ mm. Electrophysical results are confirmed during the high current high temperature experiment conducted by a powerful high-voltage equipment calculation information on the choice of average value of quantized number n_{0m} for longitudinal «hot» areas of the width Δz of the wire, different anomalous enhanceable concentration of drifting lone electrons and accordingly temperature of Joule heating. *Originality.* On the basis of the known conformities to the law of atomic and quantum physics new quantum-mechanical calculation correlation is obtained for determination in a metallic conductor with axial current of conductivity $i_0(t)$ of different type (direct, alternating and pulsed) of average number n_{0m} of the quantized longitudinal electron de Broglie half waves and accordingly longitudinal «hot» areas of the width Δz of periodic localization along the conductor of drifting lone electrons. *Practical value.* Obtained results allow to make an evaluation prognosis on finding of possible places of longitudinal periodic localization of drifting lone electrons on narrow areas of the width Δz of current-carrying parts of power wires and cables of objects of electrical power energy, production and dwellings apartments, showing up most strongly (expressed) in malfunctions of operation of cable-conductor products with the currents of short-circuit and high current density. References 26, figures 4.

Key words: metal conductor, pulsed current, calculation-experimental determination of the average number of quantized longitudinal electron de Broglie half waves and electron localization zones in a conductor.

Представлені результати теоретичних і експериментальних досліджень, які пов'язані з визначенням усередненого числа n_{0m} квантованих подовжніх електронних півхвиль де Бройля в металевому провіднику з імпульсним аксіальним струмом провідності великої щільності. Отримані результати вказують на квантово-хвильовий характер протікання імпульсного струму провідності в цьому провіднику, що приводить до виникнення в його структурі квантованої подовжньої періодичної локалізації вільних електронів, що дрейфують, на ділянках шириною Δz . Дані зони локалізації електронів відрізняються підвищеною температурою нагріву. Бібл. 26, рис. 4.

Ключові слова: металевий провідник, імпульсний струм, розрахунково-експериментальне визначення усередненого числа квантованих подовжніх електронних півхвиль де Бройля і зон локалізації електронів в провіднику.

Представлены результаты теоретических и экспериментальных исследований, связанных с определением усредненного числа n_{0m} квантованных продольных электронных полуволи де Бройля в металлическом проводнике с импульсным аксиальным током проводимости большой плотности. Полученные результаты указывают на квантово-волновой характер протекания импульсного тока проводимости в этом проводнике, приводящий к возникновению в его структуре квантованной продольной периодической локализации дрейфующих свободных электронов на участках шириной Δz . Данные зоны локализации электронов отличаются повышенной температурой нагрева. Библ. 26, рис. 4.

Ключевые слова: металлический проводник, импульсный ток, расчетно-экспериментальное определение усредненного числа квантованных продольных электронных полуволи де Бройля и зон локализации электронов в проводнике.

Introduction. A number of scientific publications in recognized domestic and foreign Journals and monographs have been devoted to theoretical and experimental studies of the quantum-wave nature of the electric conduction current in cylindrical metal conductors [1-11]. The results of these studies are fundamental in nature and allow to take a fresh look at the quantum mechanical processes of propagation and localization in the crystal structure of the metal of the indicated conductors of their drifting collectivized free electrons, which possess wave properties and are characterized by

their de Broglie wavelengths λ_e [12, 13]. As is known, for the wavelengths λ_e of electron waves propagating in a metal of a cylindrical conductor with current in its longitudinal and radial directions, the fundamental relation from the field of wave mechanics (quantum physics) holds, obtained in 1924 by the outstanding French theoretical physicist Louis de Broglie and having the following classic form [12, 13]:

$$\lambda_e = h / (m_e v_e), \quad (1)$$

where $h = 6.626 \cdot 10^{-34}$ J·s is the Planck constant;

© M.I. Baranov, S.V. Rudakov

$m_e = 9.109 \cdot 10^{-31}$ kg is the rest mass of the electron; v_e is the velocity of motion (drift) of free electrons in the crystalline structure of the material of the conductor.

According to [1–13], the behavior of free electrons in a metal conductor of a cylindrical shape is described by the corresponding Schrödinger wave ψ -functions (they were first proposed and obtained in an analytical form at the beginning for coupled electrons of hydrogen-like atoms when solving the corresponding wave equation (it entered the history of modern physics as Schrödinger equation) by the outstanding Austrian theoretical physicist Erwin Schrödinger in 1926 [14]), varying in space and time according to the harmonic law and square whose module determines the probability density of their (electrons) being in a particular place in the cylindrical volume of the conductor. In this regard, the most probable places of drift of free electrons under the action of applied to the opposite ends of the conductor constant, alternating, or pulsed electric voltage of free electrons in the conductor metal will be those that correspond to the amplitudes of the Schrödinger wave ψ -functions and, accordingly, the amplitudes of the electron waves of length λ_e , spatio-temporal changes of which also occur in harmonic law. In addition, the wave distributions of drifting free electrons in the metal structure of any conductor obey the fundamental principle of quantum mechanics – the Heisenberg uncertainty relation [12, 13], formulated by the outstanding German theoretical physicist Werner Heisenberg in 1927 [14] and having for longitudinal z and radial r coordinates of a cylindrical conductor with current the following canonical form:

$$m_e \Delta v_{ez} \Delta z \geq h / 4\pi ; \quad (2)$$

$$m_e \Delta v_{er} \Delta r \geq h / 4\pi , \quad (3)$$

where Δz , Δr are, respectively, the uncertainties of the longitudinal and radial coordinates of free electrons drifting in the structure of the material of the conductor; Δv_{ez} , Δv_{er} are the uncertainties of the longitudinal and radial components of the drift velocity v_e of the electrons in the conductor material, respectively.

It follows from (2) and (3) that even for known (numerically specified) values of the velocities Δv_{ez} and Δv_{er} of drifting free electrons, their spatial location in the cylindrical volume of the material of the conductor with current remains undefined and quantitatively determined by the quantities Δz and Δr , respectively. Taking into account the above physical (statistical) interpretation of Schrödinger wave ψ -functions, proposed in 1926 by the outstanding German theoretical physicist Max Born [14], the midpoints of the indicated Δz and Δr values for drifting free electrons will correspond to the amplitudes of electron waves of length λ_e .

With the numerical value of the longitudinal velocity v_{ez} of the drift of free electrons in the copper conductor (respectively, and the numerical value of its uncertainty Δv_{ez}), in the limit of, for example, for the short circuit (SC) mode in the electric circuit (with a longitudinal current density δ_{ez} of about 1 kA/mm² [15]), about 37 mm/s, it follows from (1) and (2) that the length $\lambda_{ez}/2$ of

the de Broglie electron half wave in this metal of the conductor will be numerically about 9.8 mm, and the Δz value of the longitudinal localization of drifting free electrons in a conductor – about 1.56 mm. It can be seen that in the case under consideration (in the SC mode), the quantities $\lambda_{ez}/2$ and Δz take macro-sizes commensurate with the transverse dimensions of the real conductors used in electrical engineering and the electric power industry. In this regard, for this case, wave manifestations in the conductor metal of drifting free electrons, leading to local periodic overheating of the conductor metal in sections of width Δz , can be physically detected and recorded using measuring equipment (for example, a thermal imager or camera). As for the random (thermal) motion of free electrons in a copper conductor without conduction current (before applying an electric voltage to it), then in this case their highest speed, determined according to the Fermi-Dirac quantum statistics by the Fermi energy W_F [12, 13], takes numerical value of about $1.6 \cdot 10^6$ m/s. Substituting this value of the electron velocity in (1) and (2), we find that for this case (the initial state of the «electron cloud» of the conductor), the desired values of $\lambda_e/2$ and Δz take nano-sizes, respectively, equal to approximately 0.23 nm and 0.036 nm. Therefore, it is not possible for the researcher to identify local manifestations of the wave properties of free electrons randomly moving in its interatomic space and their influence on macroscopic electrophysical processes (for example, on the contact potential difference of metals, thermoelectricity [12], etc.) that occur in conductors.

The above quantitative estimates indicate that, due to the relatively small values of the drift velocities v_e of free electrons in the crystalline structure of the metal of the conductor (for electric power industry, not more than 1 m/s), their wave properties will significantly affect the processes of their spatial distribution in metal conductors and, accordingly, on the processes of Joule heat release in their material.

When studying the behavior of drifting free electrons in conductor metal with conduction current, it is imperative that the quantum nature of all processes occurring in the microworld of matter be taken into account. Therefore, solutions of partial differential equations describing the wave distributions of these electrons in a conductor will be characterized by eigenvalues integers $n_0 = 1, 2, 3, \dots$ which are called quantum numbers in quantum physics [12–14].

When studying the processes of formation and propagation of drifting free electrons in a metal conductor, one should also take into account the fundamental «principle of prohibition» formulated in 1925 by the outstanding Austrian theoretical physicist Wolfgang Pauli [14] regarding the properties of bound electrons in an atom of any substance. According to the «Pauli principle of prohibition», only one bound electron can be on the electron shells of an atom of matter, having a corresponding and characteristic quantitative set of four quantum numbers [12, 13]: the main quantum number n , the orbital quantum number l , the magnetic quantum

number m_l and the spin quantum number m_s . Therefore, bound electrons even in the same atom of matter differ from each other in energy, the shape of the electron orbital, the position of the electron orbital in atomic space, and the direction of its rotation around its own axis [12, 13]. Having left its atom due to its ionization processes, these bound electrons of various properties become free, forming in the interatomic space an «electron cloud» with an averaged volumetric density (concentration) n_{em} , numerically equal for the main conductive materials (copper, aluminum, etc.) to a value of about 10^{29} m^{-3} [12].

At present, in experimental physics, a number of experimentally discovered new electrophysical effects (for example, the presence of longitudinal and radial microstrata in a «metal plasma» during the electric explosion of thin metal wires in a gas medium and vacuum by pulsed current of high density [16, 17], the presence on the axis a high-current plasma channel during a high-voltage spark discharge in a gaseous medium of cylindrical zones with significantly higher volumetric density of free electrons (a thousand or more times) compared with its peripheral zones [18] and others) did not find their theoretical justification based on the laws of classical physics. In this regard, further deepening on the basis of the laws of quantum physics of our ideas about the nature of the longitudinal-radial flow of wave processes in metal conductors of a cylindrical configuration with electric conduction current of various types (DC, AC and pulsed) and amplitude-temporal parameters (ATPs) used in modern electrical engineering, electric power industry and high pulsed current technology, is an urgent scientific and technical task. One of the steps in solving this problem is to find the number of quantized de Broglie electron half waves of average length $\lambda_{ezm}/2$ located along the indicated conductors with pulsed current and determining in them the corresponding average number of zones of width Δz that differ in their increased volumetric density according to the laws of quantum physics of free electrons and correspondingly elevated temperature.

The goal of the paper is quantitative determination by calculation and experimentally of the average number n_{0m} of quantized longitudinal de Broglie electron half waves of length $\lambda_{ezm}/2$ in a metal conductor of a cylindrical shape with pulsed axial current of high density.

1. Problem definition. Let us consider the case when axial pulsed current $i_0(t)$ of arbitrary ATPs with a large density $\delta_0(t)=i_0(t)/S_0$ averaged over its cross section S_0 flows through a thin rectilinear round continuous cylindrical conductor of radius r_0 and length $l_0 \gg r_0$. We use the Hartree-Fock single electron approximation [12, 13], which does not take into account electron-ion interactions in the internal crystalline structure of the conductor. We assume that the spatio-temporal distributions along the longitudinal coordinate z and in time t of drifting free electrons in the material of the investigated conductor with pulsed current $i_0(t)$ will

approximately obey the corresponding one-dimensional Schrödinger wave equation [12, 13]. On the basis of the quantum-mechanical approach, it is required to carry out an approximate calculation of the averaged number n_{0m} of quantized longitudinal de Broglie electron half waves of length $\lambda_{ezm}/2$ in the considered metal conductor of a cylindrical shape with pulsed axial current $i_0(t)$, and also to perform using a high-power high-voltage generator of aperiodic current pulses experimental verification of the results of calculating the number n_{0m} of quantized longitudinal electron de Broglie half waves of length $\lambda_{ezm}/2$ in this conductor.

2. Calculation estimation of the average number of quantized longitudinal de Broglie electron half waves in a metal conductor. To begin with, it was shown in [1, 4, 6-9] for the first time in the field of theoretical electrophysics that on the length l_0 of a metal conductor with conductivity current $i_0(t)$ of any kind (DC, AC, or pulsed) an integer quantum number n_0 of longitudinal de Broglie electron half waves, satisfying the following relation always fits:

$$n_0 = 2l_0 / \lambda_{ez} . \quad (4)$$

Then from (4) for the desired value of the averaged number n_{0m} of quantized longitudinal electron de Broglie half waves in the metal of the conductor it follows:

$$n_{0m} = 2l_0 / \lambda_{ezm} , \quad (5)$$

where λ_{ezm} is the average length of the quantized longitudinal de Broglie electron wave in the metal structure of a conductor with conduction current.

From (1) we find that for the quantity λ_{ezm} in a first approximation, an expression of the form is valid:

$$\lambda_{ezm} = h / (m_e v_{em}) , \quad (6)$$

where v_{em} is the average drift velocity of free electrons in a homogeneous conductor material.

It is known from atomic physics that, in the general case, v_{em} can be determined by the formula [12]:

$$v_{em} = \delta_{0m} / (\sqrt{2} e_0 n_{em}) , \quad (7)$$

where $\delta_{0m}/(2)^{1/2}$ is the root mean square value of the current pulse density $i_0(t)$ in the conductor with its amplitude δ_{0m} ; $e_0=1.602 \cdot 10^{-19} \text{ C}$ is the modulus of the electric charge of an electron; n_{em} is the averaged volumetric density of drifting free electrons in a conductor.

As a result, from (5)-(7) for the average number n_{0m} of quantized longitudinal electron de Broglie half waves in a metal conductor with pulsed axial current $i_0(t)$ of various ATPs, we have:

$$n_{0m} = \sqrt{2} m_e \delta_{0m} l_0 / (e_0 n_{em} h) . \quad (8)$$

We point out that the value of the averaged volumetric density n_{em} of drifting free electrons in the conductor metal, included in (8), is equal to the concentration N_0 of metal atoms multiplied by its valency, determined by the number of unpaired electrons on the valence electron subshells of the conductor metal atoms (for example, for copper, zinc and iron valency is equal to two [12, 19]). The concentration N_0 (m^{-3}) of atoms in the metal of the conductor with its mass density d_0 (kg/m^3)

before the pulsed current $i_0(t)$ flows through it is determined by the formula [12]:

$$N_0 = d_0(M_a \cdot 1,6606 \cdot 10^{-27})^{-1}, \quad (9)$$

where M_a is the atomic mass of the conductor material included in the D.I. Mendeleev periodic system of chemical elements and almost equal to the mass number of the nucleus of the atom of the metal of the conductor, calculated in atomic units of mass (in this case, one atomic unit of mass is numerically equal to $1.6606 \cdot 10^{-27}$ kg [13]).

In formula (8), the quantities m_e , e_0 and h are world constants [12, 13], while the values l_0 and δ_{0m} characteristic of a particular conductor can be numerically specified or determined experimentally.

It should be noted that the computational relation (8), which is simple in form of writing, was obtained in a rather rigorous way based on the known quantum-mechanical laws characteristic of the wave distribution of drifting free electrons in the metal of a conductor with current $i_0(t)$ [10].

The calculation estimation by (8) of the average number n_{0m} of quantized longitudinal de Broglie electron half waves in a steel wire ($r_0=0.8$ mm; $l_0=320$ mm; $N_0=8.43 \cdot 10^{28}$ m⁻³; $n_{em}=16.86 \cdot 10^{28}$ m⁻³ [10]), which is directly affected by axial aperiodic current pulse of a temporary shape 9 ms/160 ms ($\delta_{0m}=0.37$ kA/mm²), shows that in this case the value of n_{0m} turns out to be numerically equal to about 9.

It is important to note that a similar quantitative result for the value of the quantum number n_{0m} in a steel wire ($n=4$) with current $i_0(t)$ was previously obtained on the basis of a calculated relation of the form [10]:

$$n_{0m} = n_m / \ln n_m, \quad (10)$$

where $n_m=2n^2$ is the maximum value of the quantum number n_0 for Schrödinger wave ψ -functions describing the wave distributions of drifting free electrons in a metal conductor.

In obtaining analytical relation (10), it was assumed that the maximum number of varieties of free electrons (in their orbital l , magnetic m_l , and spin m_s quantum numbers) in a conductor metal is equal to the maximum number $2n^2$ of bound electrons in its atoms with the same principal quantum number n .

3. Experimental estimation of the average number of quantized longitudinal de Broglie electronic half waves in a metal conductor. For experimental verification of the obtained data on the choice of the averaged number n_{0m} of quantized longitudinal de Broglie electronic half waves in the conductor metal with pulsed axial current $i_0(t)$, we used a high-power PCG-C high-voltage generator that generates on the RL -load an aperiodic current pulse with amplitude of I_{0m} up to 1 kA of temporal shape $t_m/\tau_p=9$ ms/160 ms (t_m is the time corresponding to the current amplitude I_{0m} ; τ_p is the pulse duration at the level of $0.5 I_{0m}$) and the total duration t_0 of the flow through the load (conductor) is up to 1000 ms (Fig. 1) [20]].

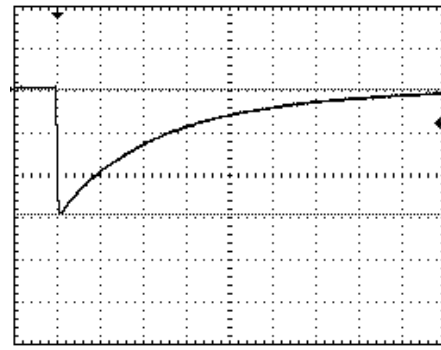


Fig. 1. Oscillogram of an aperiodic current pulse $i_0(t)$ of negative polarity of the temporal shape $t_m/\tau_p=9$ ms/160 ms flowing in the PCG-C discharge circuit with the equivalent of the electric load in the form of a square 2 mm thick aluminum sheet and plan size 500 mm \times 500 mm ($W_C \approx 400$ kJ; $U_C \approx -4.2$ kV; $I_{0m} \approx -835$ A; $t_m \approx 9$ ms; $\tau_p \approx 160$ ms; $t_0 \approx 1000$ ms; vertical scale – 282 A/cell; horizontal scale – 100 ms/cell) [22]

A straight round solid steel wire ($r_0=0.8$ mm; $l_0=320$ mm) with a thin zinc coating $\Delta_0=5$ μ m thick outside was chosen as a prototype of a metal conductor (Fig. 2). The presence of a zinc coating on the indicated wire was due to the authors' assumption related to visualization of the features of the process of intense Joule heating of the wire in quantized sections of width Δz having a refractory steel base (with a melting point of up to 1536 $^\circ$ C [21]) and a relatively low-melting zinc coating (with its melting point up to 419 $^\circ$ C and boiling point up to 907 $^\circ$ C [21]).

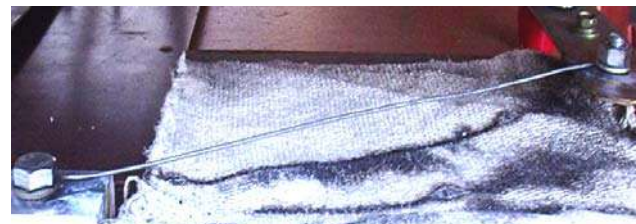


Fig. 2. General view of a round galvanized steel wire ($r_0=0.8$ mm; $l_0=320$ mm; $\Delta_0=5$ μ m; $S_0=2.01$ mm²) placed in air above a heat-shielding asbestos cloth and rigidly fixed in the discharge circuit of the PCG-C generator ($W_C \approx 310$ kJ; $U_C \approx -3.7$ kV before an aperiodic current pulse of high density flows through it [9])

In the case of Joule heating with the indicated current pulse in the discharge circuit of the PCG-C type generator (with stored electric energy W_C up to 570 kJ and charging voltage U_C of its pulse capacitors ИМ2-5-140 up to ± 5 kV) of the test wire up to temperature of about 1500 $^\circ$ C and higher along the wire in quantized sections of width Δz , it is possible to boil the zinc coating and melt the steel base of the indicated wire. In this case, visualization of periodic formation along the wire in areas of width Δz of expanded spheres consisting of products of boiling of a zinc coating and melting of the steel base of the wire becomes real. Running a little ahead, it can be noted that it was precisely this electrophysical phenomenon that was observed by electrophysicists on the desktop of the PCG-C type generator with a selected thin galvanized steel wire (Fig. 3).



Fig. 3. External view of the desktop of a powerful high-voltage generator PCG-C and the thermal state of a galvanized steel wire ($r_0=0.8$ mm; $l_0=320$ mm; $\Delta_0=5$ μ m; $S_0=2.01$ mm²) with four «hot» quantized zones with a width $\Delta z = 7$ mm and two «cold» longitudinal sections (isthmuses) about 27 mm wide after exposure to the aperiodic wire under study of the current pulse $i_0(t)$ of the temporary shape $t_m/\tau_p=9$ ms/160 ms of high density ($I_{0m}=-745$ A; $|\delta_{0m}|=0.37$ kA/mm²; $n_{0m}=9$) [9]

Figure 4 shows the oscillogram of the current pulse $t_m/\tau_p=9$ ms/160 ms, used in the study of the quantum-wave nature of the current $i_0(t)$ in the wire.

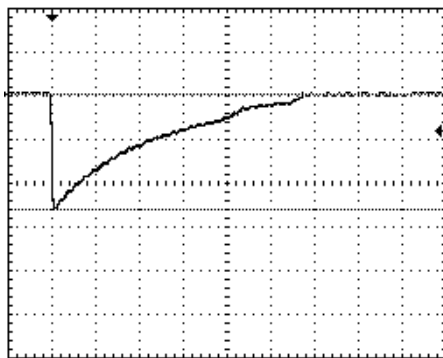


Fig. 4. Oscillogram of an aperiodic current pulse $i_0(t)$ of negative polarity of the temporal shape $t_m/\tau_p = 9$ ms/160 ms of high density ($I_{0m}=-745$ A; $|\delta_{0m}|=0.37$ kA/mm²) which destroys the galvanized steel wire ($r_0=0.8$ mm; $l_0=320$ mm; $\Delta_0=5$ μ m; $S_0=2.01$ mm²; vertical scale – 282 A/cell; horizontal scale – 100 ms/cell) [22]

According to [1-11], the longitudinal sections with a width Δz of the wire under consideration are called relatively «hot», and the longitudinal sections (isthmuses) periodically located between its zones of width Δz are called «cold». We point out that in [7, 9] it was shown that the Joule heating temperatures of these longitudinal sections of a round metal wire with the conductivity current $i_0(t)$ can differ up to 3.5 times. This is precisely the main danger of the thermal effect of large emergency SC currents on cable-conductor products (CCP) of electric power facilities, industrial and residential premises. Due to the localization of drifting free electrons in the current-carrying parts of the CCP in their narrow longitudinal sections of width Δz , which is not more than (3-10) mm in SC [10], they can quickly be intensively heated by emergency current to the ignition temperature of the CCP insulation (up to 450 °C and higher) [23]. In our opinion, this circumstance may be the main cause of

many fires due to the onset of fire during sudden SCs of a power CCP not only at electric power facilities, but also in the everyday life of citizens using AC (DC) electric networks. In this regard, not only purely scientific, but also applied interests can motivate electrophysicists in solving the quantum-mechanical problem formulated above and, accordingly, achieving the previously set goals.

The main construction schemes, technical characteristics and principles of operation of a high-voltage generator of the PCG-C type were described in [20, 24-26]. The means of high-current measuring equipment (shunts, oscilloscopes, etc.) regularly verified in the State Metrological Service that are used as part of the PCG-C generator for the experimental determination of the ATPs of the current pulse $i_0(t)$ flowing through the tested wire were also described there. From the experimental results obtained using the indicated PCG-C generator and from data of Fig. 3 it follows that when flowing along a bimetallic wire ($r_0=0.8$ mm; $l_0=320$ mm) with a thin external zinc coating ($\Delta_0=5$ μ m) and the steel base of a powerful aperiodic current pulse of negative polarity ($|\delta_{0m}|\approx|I_{0m}|/S_0\approx 0.37$ kA/mm²), such a wave longitudinal distribution of drifting free electrons in the wire metal is observed, which potentially leads to the periodic appearance of nine brightly glowing «hot» longitudinal zones along the wire with a width of approximately $\Delta z = 7$ mm, which take a spherical shape. Since the midpoints of each of these «hot» longitudinal zones of the wire correspond to the amplitudes of the quantized Schrödinger wave ψ -function ($n_0=9$) [8], their own quantized de Broglie electron half waves, characterized by quantum number $n_{0m}=9$ will correspond to them (to the middle of zones of width Δz).

It should be noted that due to different conditions of longitudinal heat removal from periodically arising along the studied thin cylindrical steel wire of relatively «hot» and «cold» longitudinal sections with a geometric step approximately equal to $\lambda_{ezm}/2 \approx 34$ mm without taking into account the two extreme «cold» and directly adjacent to the bolted joints of the sections (see Fig. 3), in the experiment performed five «hot» and eight «cold» longitudinal sections of galvanized steel wire were completely sublimated [21]. Violation of the metallic conductivity of the tested wire, caused by intense Joule heating of its current-carrying part, begins at a point in time corresponding to approximately 380 ms (see Fig. 4). Data in Fig. 4 shows that at a time from the beginning of the flow through the wire of the considered pulsed current $i_0(t)$ of about 570 ms, the metal structure of the wire is completely destroyed and the conduction current stops flowing through the wire.

The results obtained during a high-current and high-temperature experiment using a high-power PCG-C high-voltage generator and the indicated galvanized steel wire unambiguously indicate the operability of the recommended quantum-mechanical relation (8) with an approximate choice of the average number n_{0m} of quantized longitudinal de Broglie electron half waves in a

cylindrical conductor with pulsed axial current $i_0(t)$ of various ATPs.

Conclusions.

1. For the estimated forecasting of possible places of the onset of longitudinal localization of drifting free electrons in narrow sections of width Δz of current-carrying parts of power wires and cables of electric power facilities, industrial and residential premises, which is manifested most strongly in emergency operation of CCP with SC currents and high current densities, a new quantum-mechanical calculation relation (8) is proposed.

2. Experimental verification using powerful high-current high-voltage equipment and a prototype of bare galvanized steel wire with diameter of 1.6 mm and length of 320 mm (with density amplitude module of flowing for up to 570 ms through the wire an aperiodic current pulse of about $\delta_{0m}=0.37$ kA/mm² and widths Δz of each of the longitudinal localization regions of drifting free electrons in it up to 7 mm) of the proposed relation (8), which determines, for the indicated numerical value δ_{0m} , the average number $n_{0m}=9$ of quantized longitudinal electron de Broglie half wave length $\lambda_{ezm}/2 \approx 34$ mm in the metal wire, has confirmed its operability.

3. To ensure the fire safety of the power CCP in emergency operation modes, accompanied by the flow in current-carrying parts of wires and cables of alternating currents of SC with their high densities (200 A/mm² or more), it is necessary in the relevant regulatory documents that determine the conditions for reliable operation of the CCP in industrial and home conditions, to take into account the peculiarities of the influence of the wave nature of the distribution along the metal cores (shells) of the CCP of free electrons drifting in them on the possibility of occurrence in current-carrying parts of the CCP of short longitudinal zones of width Δz with abnormally increased concentration of such electrons and accordingly the temperature of indicated CCP operation modes.

REFERENCES

1. Baranov M.I. Wave distribution of free electrons in conductor with electric current of the conductivities. *Russian Electrical engineering*, 2005, no.7, pp. 25-33. (Rus).
2. Baranov M.I. Energy and frequency specters of the free electrons conductor with electric current conduction. *Russian Electrical engineering*, 2006, no.7, pp. 29-34. (Rus).
3. Baranov M.I. Wave electronic package of a conductor with electric conduction current. *Electrical engineering & electromechanics*, 2006, no.3, pp. 49-53. (Rus).
4. Baranov M.I. New physical mechanisms and approaches in the study of the formation and distribution of the electric conduction current in the conductor. *Technical Electrodynamics*, 2007, no.1, pp.13-19. (Rus).
5. Baranov M.I. Characteristic radial distribution of free electrons in a cylindrical conductor with varying electric current. *Technical Electrodynamics*, 2009, no.1, pp. 6-11. (Rus).
6. Baranov M.I. Theoretical and experimental results of research into explanation of de Broglie half-wave existence in the microstructure of an active metallic conductor. *Electrical*

- engineering & electromechanics*, 2014, no.3, pp. 45-49. (Rus). doi: 10.20998/2074-272X.2014.3.09.
7. Baranov M.I. Features heating thin bimetallic conductor large pulse current. *Elektrichestvo*, 2014, no.4, pp. 34-42. (Rus).
8. Baranov M.I. Quantum-wave nature of electric current in a metallic conductor and some of its electrophysical macro-phenomena. *Electrical engineering & electromechanics*, 2014, no.4, pp. 25-33. doi: 10.20998/2074-272X.2014.4.05.
9. Baranov M.I. The main characteristics of the wave distribution of free electrons in a thin metallic conductor with a pulse current of high density. *Elektrichestvo*, 2015, no.10, pp. 20-32. (Rus).
10. Baranov M.I. *Izbrannye voprosy elektrofiziki: Monografiya v 2-h tomah. Tom 2, Kn. 1: Teoriya elektrofizicheskikh effektov i zadach* [Selected topics of Electrophysics: Monograph in 2 vols. Vol. 2, book. 1: Theory of electrophysics effects and tasks]. Kharkov, NTU «KhPI» Publ., 2009. 384 p. (Rus).
11. Baranov M.I. *Izbrannye voprosy elektrofiziki. Monografiya v 3kh tomakh. Tom 2, Kn. 2: Teoriya elektrofizicheskikh effektov i zadach* [Selected topics of Electrophysics. Monograph in 3 Vols. Vol.2, Book 2. A theory of electrophysical effects and tasks]. Kharkiv, Tochka Publ., 2010. 407 p. (Rus).
12. Kuz'michev V.E. *Zakony i formuly fiziki* [Laws and formulas of physics]. Kiev, Naukova Dumka Publ., 1989. 864 p. (Rus).
13. Javorskij B.M., Detlaf A.A. *Spravochnik po fizike* [Handbook of physics]. Moscow, Nauka Publ., 1990. 624 p. (Rus).
14. Baranov M.I. *Antologija vydajushhihsja dostizhenij v nauke i tehnike: Monografiya v 3-h tomah. Tom 3* [An anthology of the distinguished achievements in science and technique: Monograph in 3 volumes. Volume 3]. Kharkiv, PhPB Panov A.N. Publ., 2016. 415 p. (Rus).
15. Baranov M.I. Refined selection of allowable cross-sections of electrical conductors and cables in the power circuits of industrial electrical equipment taking into account emergency operating modes. *Electrical engineering & electromechanics*, 2019, no.3, pp. 37-43. doi: 10.20998/2074-272X.2019.3.06.
16. Stolovich N.N. *Elektrovzryvnye preobrazovateli energii* [Electroexplosion energy converters]. Minsk, Nauka & Tehnika Publ., 1983. 151 p. (Rus).
17. Sobolev N.N. The study of electrical explosion of thin wires. *Journal of experimental and theoretical physics*, 1947, Vol.17, no.11, pp. 986-997. (Rus).
18. Ivanovskii A.V., Spirov G.M., Dudai P.V., Volkov A.A., Luk'yanov N.B., Solov'ev A.A., Volkova T.I., Lysenko V.P.. A test bench for studying the mechanisms of breakdowns of insulating gaps by short voltage pulses. *Instruments and Experimental Techniques*, 2003, vol. 46, no. 4, pp. 494-501. doi: 10.1023/A:1025182031922.
19. Solymar L., Walsh D. *Lekcii po elektricheskim svoystvam materialov* [Lectures on the electrical properties of materials]. Moscow, Mir Publ., 1991. 504 p. (Rus).
20. Baranov M.I., Koliushko G.M., Kravchenko V.I., Nedzel'skii O.S., Dnyshchenko V.N. A current generator of the artificial lightning for full-scale tests of engineering objects. *Instruments and Experimental Technique*, 2008, no.3, pp. 401-405. doi: 10.1134/s0020441208030123.
21. Kuhling H. *Spravochnik po fizike. Per. s nem.* [Dictionary on Physics. Translated from German]. Moscow, Mir Publ., 1982. 520 p. (Rus).
22. Baranov M.I., Rudakov S.V. Calculation-experimental method of research in a metallic conductor with the pulse current of electronic wavepackages and de Broglie electronic half-waves. *Electrical engineering & electromechanics*, 2016, no.6, pp. 45-53. doi: 10.20998/2074-272X.2016.6.08.

23. Belorussov N.I., Saakjan A.E., Jakovleva A.I. *Elektricheskie kabeli, provoda i shnury. Spravochnik* [Electrical cables, wires and cords. Directory]. Moscow, Energoatomizdat Publ., 1988. 536 p. (Rus).

24. Baranov M.I., Buriakovskiy S.G., Rudakov S.V. The tooling in Ukraine of model tests of objects of energy, aviation and space-rocket engineering on resistibility to action of pulsed current of artificial lightning. *Electrical engineering & electromechanics*, 2018, no.4, pp. 45-53. doi: **10.20998/2074-272X.2018.4.08**.

25. Baranov M.I., Kniaziev V.V., Rudakov S.V. The coaxial shunt for measurement of current pulses of artificial lightning with the amplitude up to ± 220 kA. *Instruments and Experimental Technique*, 2018, vol.61, no.4, pp. 501-505. doi: **10.1134/S0020441218030156**.

26. Baranov M.I., Buriakovskiy S.G., Rudakov S.V. The metrology support in Ukraine of tests of objects of energy, aviation and space-rocket engineering on resistibility to action of pulses of current (voltage) of artificial lightning and commutation pulses of voltage. *Electrical engineering &*

electromechanics, 2018, no.5, pp. 44-53. doi: **10.20998/2074-272X.2018.5.08**.

Received 19.11.2019

M.I. Baranov¹, Doctor of Technical Science, Professor,
S.V. Rudakov², Candidate of Technical Science, Associate
Professor,

¹ Scientific-&-Research Planning-&-Design Institute «Molniya»,
National Technical University «Kharkiv Polytechnic Institute»,
47, Shevchenko Str., Kharkiv, 61013, Ukraine,
phone +380 57 7076841,

e-mail: baranovmi@kpi.kharkov.ua

² National University of Civil Protection of Ukraine,
94, Chernyshevska Str., Kharkiv, 61023, Ukraine,
phone +380 57 7073438,

e-mail: serg_73@i.ua

How to cite this article:

Baranov M.I., Rudakov S.V. Calculation-experimental determination of the average number of quantized longitudinal electron de Broglie half waves in a cylindrical conductor with pulsed axial current. *Electrical engineering & electromechanics*, 2020, no.2, pp. 33-39. doi: **10.20998/2074-272X.2020.2.05**.

S.T. Tolmachev, A.V. Il'chenko

THE RECIPROCITY PRINCIPLE FOR A NONLINEAR ANISOTROPIC MEDIUM WITHOUT HYSTERESIS: THEORY AND PRACTICE OF APPLICATION

The construction of the correct vector material equations for nonlinear anisotropic soft magnetic materials remains one of the main reserves for increasing the accuracy of mathematical models in solving magnetostatic problems in the field formulation. The aim of the work is to establish asymptotic expressions for the reciprocity principle, which is a fundamental property of reversible magnetization processes of nonlinear anisotropic media, and to use the obtained results to optimize the computational process when constructing the vector magnetization characteristic and differential permeability tensor. The potentiality property of the magnetic flux density vector B in H -space is used. The main result of the paper is an illustration, using concrete examples, of an alternative method for calculating vector magnetization characteristics for one of the orthogonal families. In order to eliminate the instrumental error and ensure maximum accuracy and reliability of the obtained results, the exact characteristics for the components of the vector magnetization characteristic obtained by differentiating a special analytical expression for the potential were used as initial ones. The principle of reciprocity, by virtue of its universal nature, makes a significant contribution to the theory of nonlinear anisotropic media in the hysteresis-free approximation. Asymptotic expressions for the reciprocity principle are obtained for the first time. The performed computational experiments on the construction of vector characteristics based on the known magnetization characteristics in one of the directions confirm almost complete coincidence with the exact values obtained analytically. The use of asymptotic expressions for the reciprocity principle not only greatly simplifies computational processes for determining the orthogonal magnetization characteristics, but also implements the calculation of differential permeability tensors for arbitrary field values. The proposed method can be implemented in applications for calculating the magnetic field in devices with nonlinear anisotropic magnetically soft materials, primarily with cold rolled sheet electrical steels, which are most used in electrical engineering. References 12, figures 5.

Key words: nonlinear anisotropic medium, vector magnetization characteristics, energy potential, reciprocity principle, asymptotic expressions, magnetic permeability tensor.

Розглянуто теоретичні та практичні аспекти побудови векторних матеріальних рівнянь нелінійних анізотропних середовищ. Показано, що існуючі методи обліку магнітних властивостей навіть в безгістерезисному наближенні не завжди задовольняють вимогам повноти й математичної строгості. Підтверджено ефективність енергетичного підходу до побудови векторних характеристик магнітного стану таких середовищ. Особливу увагу приділено принципу взаємності як фундаментальній властивості оборотних процесів намагнічування. Встановлено нові асимптотичні вирази для принципу взаємності і на численних прикладах показана їх ефективність при побудові векторної моделі магнітного середовища без використання енергетичного потенціалу. Бібл. 12, рис. 5.

Ключові слова: нелінійне анізотропне середовище, векторні характеристики намагнічування, енергетичний потенціал, принцип взаємності, асимптотичні вирази, тензор магнітної проникності.

Рассмотрены теоретические и практические аспекты построения векторных материальных уравнений нелинейных анизотропных сред. Показано, что используемые методы учета магнитных свойств даже в безгистерезисном приближении не всегда удовлетворяют требованиям полноты и математической строгости. Подтверждена эффективность энергетического подхода к построению векторных характеристик магнитного состояния таких сред. Особое внимание уделено принципу взаимности как фундаментальному свойству обратимых процессов намагничивания. Установлены новые асимптотические выражения для принципа взаимности и на численных примерах показана их эффективность при построении векторной модели магнитной среды без использования энергетического потенциала. Библ. 12, рис. 5.

Ключевые слова: нелинейная анизотропная среда, векторные характеристики намагничивания, энергетический потенциал, принцип взаимности, асимптотические выражения, тензор магнитной проницаемости.

Introduction. Advances in information technology in recent decades have stimulated the development of methods for mathematical modelling of magnetic fields in various electrophysical devices [1-7]. One of the important stages of the practical implementation of problems in the field formulation is the formation of the material equations of the magnetic medium, which in most cases has nonlinear anisotropy. The completeness of the taking into account of magnetic properties of such a medium requires the construction of a vector characteristic $B(H)$. The construction of vector models based on the scalar dependencies $B_i(H_i)$ for the principal axes of anisotropy [3, 4], the taking into account of magnetic anisotropy in the framework of «elliptic models» [4, 5], and other simplified approaches are more likely forced than constructive solution and, as shown in

[8], inevitably lead to a loss of information and an almost uncontrolled calculation error.

Some progress in taking into account of the nonlinear anisotropy of the vector models $B(H)$ in the hysteresis-free approximation is associated with the energy approach [1, 6-10]. The basic relation of this approach is the expression [11]

$$\oint_{L_H} \mathbf{B} \, d\mathbf{H} = 0, \quad (1)$$

where L_H is the arbitrary closed contour in H -space, i.e. in space, on the axes of which the quantities H_1 and H_2 are plotted and which in essence is the hodograph of the vector H with an arbitrary cyclic magnetization reversal of the medium. With such a definition of H -space,

relation (1) formally coincides with the classical condition of potentiality, since an expression under the sign of the integral is the total differential of the potential $\Psi(\mathbf{H})$.

The above definition of \mathbf{H} -space indicates the independence of the potential $\Psi(\mathbf{H})$ from the integration path in \mathbf{H} -space, the eddy-free character of the magnetic flux density field \mathbf{B} , which is the force vector of the field in this space:

$$\mathbf{B} = -\frac{d\Psi}{d\mathbf{H}} = \text{grad}_{\mathbf{H}} \Psi(\mathbf{H}) = i_1 B_1(H_1, H_2) + i_2 B_2(H_1, H_2). \quad (2)$$

In addition, we note an important consequence of relations (1) and (2) – the symmetry of the differential magnetic permeability tensor $\mu_d(\mathbf{H})$:

$$\mu_d = \frac{d\mathbf{B}}{d\mathbf{H}}; \quad \mu_{dij} = \frac{\partial^2 \Psi}{\partial H_i \cdot \partial H_j} = \frac{\partial^2 \Psi}{\partial H_j \cdot \partial H_i} = \mu_{dji}. \quad (3)$$

In formulas (2), (3), we use the notation associated with the concepts of the derivative of a scalar and a vector function with respect to the vector argument used in vector algebra [12, items 6.2, 6.3].

Energy potentials cannot be measured directly; therefore, their construction is a difficult problem even in the two-dimensional case [7]. The basic information for construction of the potential is a certain set of experimentally measured magnetization characteristics, which are used either by their direct integration, or by selecting the coefficients of some analytical dependence [7, 8]. Leaving beyond the scope of this paper the known problems with the accuracy of measuring the magnetic characteristics of anisotropic materials, we note the obvious problems with the numerical differentiation of the potential $\Psi(\mathbf{H})$: direct – to obtain the vector dependence $\mathbf{B}(\mathbf{H})$ and repeated – for the differential magnetic permeability tensor $\mu_d(\mathbf{H})$.

An alternative way to determine the magnetization characteristics in mutually orthogonal directions without explicitly defining the potential $\Psi(\mathbf{H})$ is the reciprocity principle, first formulated in [9] and developed in a number of subsequent publications (see, for example, [8, 10]). The reciprocity principle is a fundamental property of an anisotropic medium without hysteresis and is based on the independence of the potential $\Psi(\mathbf{H})$ from the integration path in \mathbf{H} -space.

Let $H_1' \leq H_1 \leq H_1''$ and $H_2' \leq H_2 \leq H_2''$. Equation (1) implies the equality of the integrals S_1 and S_2 :

$$\begin{aligned} S_1 &= \int_{H_1'}^{H_1''} [B_1(H_1, H_2') - B_1(H_1, H_2'')] \cdot dH_1; \\ S_2 &= \int_{H_2'}^{H_2''} [B_2(H_1', H_2) - B_2(H_1'', H_2)] \cdot dH_2. \end{aligned} \quad (4)$$

Energy relations (4) have a simple geometric meaning: the areas of the corresponding curved quadrangles S_1 and S_2 are the same. Visually, relations (4) at $H_1' = H_2' = 0$ and $H_1'' = H_1^*$, $H_2'' = H_2^*$ are shown in Fig. 1.

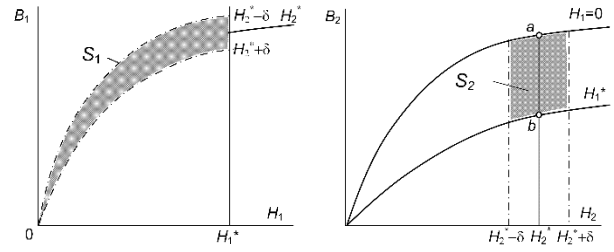


Fig. 1. Geometric meaning of the principle of reciprocity

In practical terms, the importance of the reciprocity principle lies in the possibility of constructing a vector magnetization characteristic $\mathbf{B}(\mathbf{H})$ from partially given information about the magnetic properties of a nonlinear anisotropic medium.

The goal of this paper is further generalization of the reciprocity principle (4), in particular, obtaining its asymptotic expressions and using them to optimize the computational process when constructing the vector characteristic $\mathbf{B}(\mathbf{H})$ and the differential magnetic permeability tensor $\mu_d(\mathbf{H})$. As we know, it is this information about the magnetic properties of the medium that is used in various computational schemes.

Asymptotic expressions for the principle of reciprocity.

A. The case of Cartesian coordinates. We write relations (4) in relation to Fig. 1:

$$\begin{aligned} S_1 &= \int_0^{H_1^*} [B_1(H_1, H_2^* + \delta) - B_1(H_1, H_2^* - \delta)] \cdot dH_1; \\ S_2 &= \int_{H_2^* - \delta}^{H_2^* + \delta} [B_2(0, H_2) - B_2(H_1^*, H_2)] \cdot dH_2. \end{aligned} \quad (5)$$

Since relations (5) are valid for arbitrary values of δ , we consider the limiting expressions for the integrals $R_1^* = R_2^*$:

$$\begin{aligned} R_1^* &= \lim_{\delta \rightarrow 0} \int_0^{H_1^*} \frac{1}{2\delta} [B_1(H_1, H_2^* + \delta) - B_1(H_1, H_2^* - \delta)] \cdot dH_1; \\ R_2^* &= \lim_{\delta \rightarrow 0} \int_{H_2^* - \delta}^{H_2^* + \delta} \frac{1}{2\delta} [B_2(0, H_2) - B_2(H_1^*, H_2)] \cdot dH_2. \end{aligned} \quad (6)$$

For small values of δ , the integrand in the first integral (6) can be expressed in terms of differential magnetic permeability μ_{d12} :

$$\lim_{\delta \rightarrow 0} [\Delta B_1(H_1, H_2^*) / \Delta H_2] \approx \mu_{d12}(H_1, H_2^*),$$

therefore, the integral R_1^* becomes curved and takes the form

$$R_1^* = \int_0^{H_1^*} \mu_{d12}(H_1, H_2^*) \cdot dH_1. \quad (7)$$

As for the integral R_2^* , as can be seen from Fig. 1, at $\delta \rightarrow 0$, the area S_2 degenerates into a line ab , which corresponds to the increment of the magnetic flux density component B_2 at $H_2 = H_2^*$ and $0 \leq H_1 \leq H_1^*$. Therefore

$$R_2^* \rightarrow ab = \int_0^{H_1^*} \mu_{d12}(H_1, H_2^*) \cdot dH_1. \quad (8)$$

Obviously, when the integration limits are compressed to a point, we obtain the symmetry of the differential magnetic permeability tensor $\mu_d(\mathbf{H})$ established previously by relation (3). Thus, the reciprocity principle has three possible representations: point one (at each «point» \mathbf{H}) – (3) and two integral ones – respectively (4) and (7), (8).

We note the important practical significance of the obtained asymptotic expressions. It was shown in [8] that the restoration of potential Ψ is possible from a family of magnetization characteristics in one direction, for example, $B_1(H_1, H_2)$ and one orthogonal characteristic, for example, $B_2(0, H_2)$. As will be shown below, the missing array of points of characteristics $B_2(H_1, H_2)$ can be obtained without calculating the potential Ψ using expression (8).

Note that by rearranging the indices, we can obtain relations similar to (7), (8) for other initial data, for example, $B_2(H_1, H_2)$ and $B_1(H_1, 0)$:

$$R_2^* = \int_0^{H_2^*} \mu_{d21}(H_2, H_1^*) \cdot dH_2; \quad (9)$$

$$R_1^* \rightarrow cd = \int_0^{H_2^*} \mu_{d12}(H_2, H_1^*) \cdot dH_2, \quad (10)$$

and $R_1^* = R_2^*$.

B. The case of polar coordinates. Relations (1), (2) are invariant with respect to the coordinate system. We assume that the family of «longitudinal» magnetization characteristics $B_{||}(H, \alpha)$, where $B_{||}$ is the projection of the vector \mathbf{B} onto the vector \mathbf{H} , and α is the angle defining the direction of the vector \mathbf{H} is specified (basic) information. For the vector \mathbf{B} , we use the decomposition $\mathbf{B} = \mathbf{B}_{||}(H, \alpha) + \mathbf{B}_{\perp}(H, \alpha)$, where $\mathbf{B}_{\perp}(H, \alpha)$ is the family of characteristics of «transverse» magnetization orthogonal to $\mathbf{B}_{||}(H, \alpha)$.

In view of the above, formula (2) takes the form

$$\mathbf{B} = \frac{d\Psi}{d\mathbf{H}} = \text{grad}_{\mathbf{H}} \Psi(\mathbf{H}) = \mathbf{r}^0 \frac{\partial \Psi}{\partial H} + \boldsymbol{\alpha}^0 \frac{1}{H} \cdot \frac{\partial \Psi}{\partial \alpha}, \quad (11)$$

where \mathbf{r}^0 , $\boldsymbol{\alpha}^0$ are the unit vectors of the polar coordinate system.

We note the possibility of reconstructing the potential from a given family of characteristics $\mathbf{B}_{||}(H, \alpha)$. So, taking $\Psi(0) = 0$, for an arbitrary point $\mathbf{H} = (H, \alpha^*)$ we obtain

$$\Psi(\mathbf{H}) = \int_0^H B_{||}(H, \alpha) \cdot dH$$

and $B_{\perp}(H, \alpha) = \frac{1}{H} \cdot \frac{\partial \Psi}{\partial \alpha}$.

As in the case of Cartesian coordinates, to calculate the orthogonal characteristics $B_{\perp}(H, \alpha)$ without calculating the potential, we use the reciprocity principle.

Let $H' \leq H \leq H''$ and $\alpha' \leq \alpha \leq \alpha''$. We have the equality of integrals S_1 and S_2 :

$$S_1 = \int_{H'}^{H''} [B_{||}(H, \alpha') - B_{||}(H, \alpha'')] \cdot dH; \quad (12)$$

$$S_2 = \int_{\alpha'}^{\alpha''} [H' \cdot B_{\perp}(H', \alpha) - H'' \cdot B_{\perp}(H'', \alpha)] \cdot d\alpha.$$

The proof and illustration of relations (12) are given in [9]. We establish the asymptotic properties of the reduced integral reciprocity principle, similar to relations (9) and (10). Let $\mathbf{H}^* = (H^*, \alpha^*)$ be given – some point in the intervals $H' \leq H^* \leq H''$, $\alpha' \leq \alpha^* \leq \alpha''$ and δ_α – the deviation of the angle α from this point. Then, by analogy with (5) for $H' = 0$ and $H'' = H^*$ (Fig. 2)

$$S_1^* = \int_0^{H^*} [B_{||}(H, \alpha^* + \delta_\alpha) - B_{||}(H, \alpha^* - \delta_\alpha)] \cdot dH; \quad (13)$$

$$S_2^* = \int_{\alpha^* - \delta_\alpha}^{\alpha^* + \delta_\alpha} -H^* \cdot B_{\perp}(H^*, \alpha) \cdot d\alpha.$$

Limit expressions for these relations

$$R_1^* = \lim_{\delta_\alpha \rightarrow 0} \int_0^{H^*} \frac{1}{2\delta_\alpha} [B_{||}(H, \alpha^* + \delta_\alpha) - B_{||}(H, \alpha^* - \delta_\alpha)] \cdot dH; \quad (14)$$

$$R_2^* = \lim_{\delta_\alpha \rightarrow 0} \int_{\alpha^* - \delta_\alpha}^{\alpha^* + \delta_\alpha} \frac{-1}{2\delta_\alpha} H^* \cdot B_{\perp}(H^*, \alpha) \cdot d\alpha.$$

The first integral in (14) can be expressed in terms of the differential magnetic permeability $\mu_{dH\alpha}$. The integral R_2^* , as can be seen from Fig. 2, for $\delta_\alpha \rightarrow 0$, by analogy with (7), (8), degenerates into the line cd :

$$R_1^* \rightarrow cd = \int_0^{H_1^*} \mu_{dH\alpha}(H, \alpha^*) \cdot dH. \quad (15)$$

Since for $H = 0$ $H \cdot B_{\perp} = 0$ for all α , the value of the segment cd determines the value of $H^* \cdot B_{\perp}(H^*)$ and, therefore, $B_{\perp}(H^*)$. Similarly, we can calculate the remaining components of the array $B_{\perp}(\mathbf{H})$.

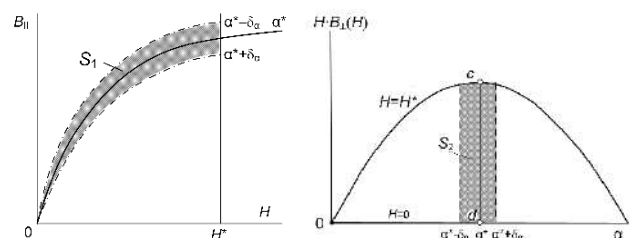


Fig. 2. Geometric meaning of the principle of reciprocity for polar coordinates

Computational experiments and discussion. In order to eliminate the instrumental error and ensure maximum accuracy and reliability of the results, we use the exact magnetization characteristics $B_1(H_1, H_2)$ and

$B_2(H_1, H_2)$ obtained by differentiating the potential given in [8] (Fig. 3,a,b).

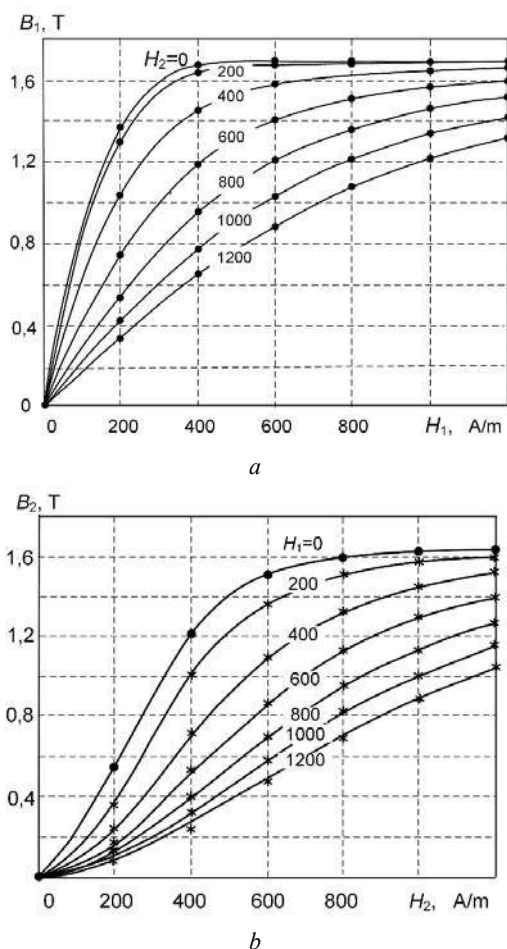


Fig. 3. Nonlinear anisotropic medium magnetization characteristics obtained by differentiation of the potential [8]

It follows from the reciprocity principle that the family of characteristics $B_2(H_1, H_2)$ can be calculated from the characteristics $B_1(H_1, H_2)$ and one of the characteristics $B_2(H_1, H_2)$, for example, $B_2(0, H_2)$. This information is reflected in Fig. 3,a,b by the symbols «•» for nodes in which the values of magnetic flux density will be considered known. The symbols «*» correspond to the calculated values obtained by using expression (8) for the missing mesh nodes. From Fig. 3,b, one can see almost complete coincidence with the calculated dependences $B_2(\mathbf{H})$ (solid lines).

The algorithm of «filling» information on the magnetic properties of a nonlinear anisotropic medium is as follows. Using the known array of characteristics $B_1(\mathbf{H})$, by differentiation we obtain three components of the tensor $\mu_d(\mathbf{H})$: $\mu_{d11}(\mathbf{H}) = \partial B_1(\mathbf{H}) / \partial H_1$; $\mu_{d12}(\mathbf{H}) = \partial B_1(\mathbf{H}) / \partial H_2 = \mu_{d21}(\mathbf{H})$. Then, using expression (8), we find the corresponding values of the integrals ab , the subtraction of which from the values of the given characteristic $B_2(0, H_2)$ determines the family of characteristics $B_2(\mathbf{H})$ and, finally, $\mu_{d22}(\mathbf{H}) = \partial B_2(\mathbf{H}) / \partial H_2$.

To confirm, we give some numerical examples. We choose two arbitrary vectors of magnetic field strength \mathbf{H} ,

for example, $\mathbf{H}^{(1)} = (450, 600)$ A/m and $\mathbf{H}^{(2)} = (1120, 375)$ A/m. The calculated values of the corresponding magnetic flux density vectors $\mathbf{B}^{(1)} = (1.259, 1.005)$ T and $\mathbf{B}^{(2)} = (1.669, 0.275)$ T. And here, if the values of the B_1 components (1.259 T and 1.669 T, respectively) are obtained by spline interpolation of a given array of nodal values of the magnetic flux density $B_1(H_1, H_2)$ (see Fig. 3,a), then the corresponding values of the B_2 components are calculated by the above technique without calculating the potential Ψ . The exact values of the magnetic flux density vectors obtained by using the analytical expressions from [8]: $\mathbf{B}^{(1)*} = (1.259, 1.022)$ T, $\mathbf{B}^{(2)*} = (1.670, 0.257)$ T. The mismatch angles between the vectors \mathbf{B} and \mathbf{H} are respectively equal 9.75° and 14.07° .

We also give the calculated and exact (*) values of the differential absolute magnetic permeability tensors for given values $\mathbf{H}^{(1)}$ and $\mathbf{H}^{(2)}$:

- for $\mathbf{H} = \mathbf{H}^{(1)}$

$$\mu_d^{(1)} = \begin{vmatrix} \mu_{d11} & \mu_{d12} \\ \mu_{d21} & \mu_{d22} \end{vmatrix} = 10^{-3} \cdot \begin{vmatrix} 1.28247 & -1.25014 \\ -1.25014 & 1.54950 \end{vmatrix}$$

$$\mu_d^{(1)*} = 10^{-3} \cdot \begin{vmatrix} 1.26986 & -1.23883 \\ -1.23883 & 1.56906 \end{vmatrix}$$

- for $\mathbf{H} = \mathbf{H}^{(2)}$

$$\mu_d^{(2)} = 10^{-4} \cdot \begin{vmatrix} 0.53929 & -2.19504 \\ -2.19504 & 10.7357 \end{vmatrix}$$

$$\mu_d^{(2)*} = 10^{-4} \cdot \begin{vmatrix} 0.53756 & -2.21087 \\ -2.21087 & 11.2446 \end{vmatrix}$$

We note that the given values of the tensors $\mu_d(\mathbf{H})$ are local, therefore, from the fact that for the selected values of the field strength vectors $\mu_{d22} > \mu_{d11}$, it cannot be concluded that the H_2 axis is the direction of easy magnetization. As will be illustrated in Fig. 4, this direction is the axis H_1 .

We also note one of the useful consequences of the integral reciprocity principle: at the same scales for the corresponding components of the vectors \mathbf{B} and \mathbf{H} , the areas bounded by the limiting magnetization curves are the same, since according to (4) the areas of all the corresponding curved quadrangles are the same. For shown in Fig. 3,a,b boundary characteristics $B_1(H_1, 0)$ and $B_1(H_1, 1200)$, $B_2(0, H_2)$ and $B_2(1200, H_2)$, by integration almost identical values were obtained: 880.4670 J and 880.4688 J. This property can be useful in conditions of limited information on the magnetic properties of an anisotropic medium, when only two characteristics are specified in orthogonal directions.

To further illustrate the anisotropic properties of the considered medium, Fig. 4 shows the hodographs of the vector \mathbf{H} (semicircles of radii of 1200, 600, and 300 A/m) and the corresponding hodographs of the magnetic flux density vector \mathbf{B} . The anisotropy of the medium is manifested by a pronounced nonlinear dependence of magnetic flux density on the field strength, more «easy» magnetization in the direction of the H_1 axis, and significant mismatch between vectors \mathbf{B} and \mathbf{H} in almost the entire range of field changes.

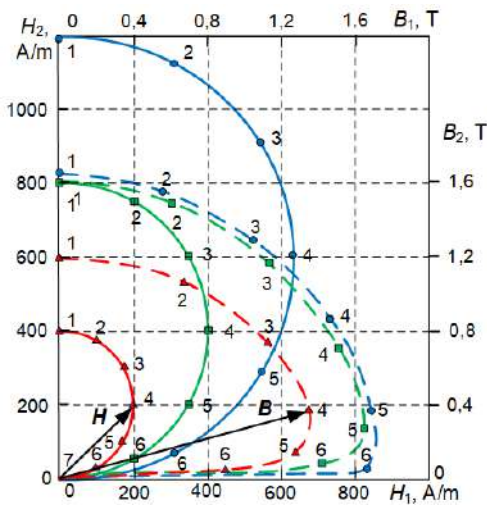


Fig. 4. Hodographs of the change of vectors \mathbf{B} and \mathbf{H} of a nonlinear anisotropic medium

Figures 5, *a, b* show the magnetization characteristics for the polar coordinate system (H, α) , which are obtained by recalculating characteristics presented in Fig. 3, *a, b*. As in Fig. 3, the symbols « \bullet » mark the nodes of the «longitudinal» magnetization characteristics with known magnetic flux density values at $H = 0:200:1200$ A/m, $\alpha = 0:\pi/12:\pi/2$, and the symbols « $*$ » correspond to the calculated values obtained using the expression (15) for nodes of the «transverse» magnetization characteristics $B_{\perp}(H, \alpha)$.

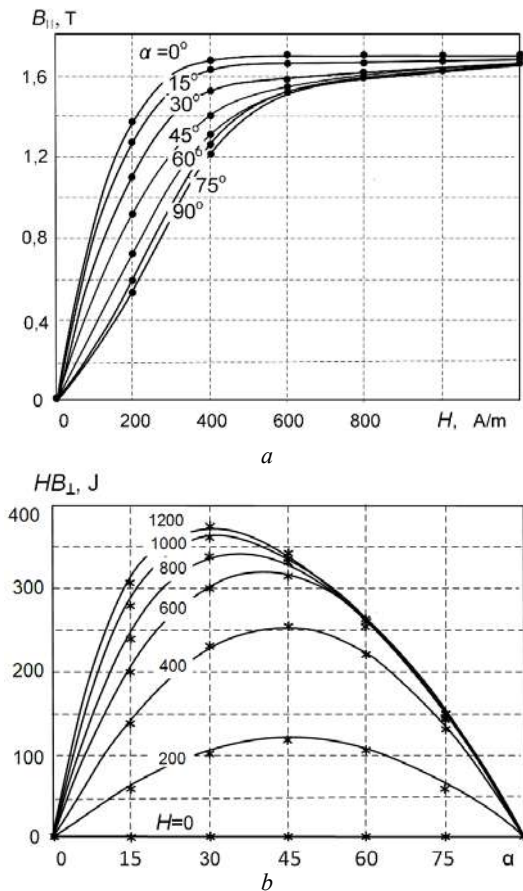


Fig. 5. «Longitudinal» – *a* and «transverse» – *b* characteristics of magnetization of an anisotropic medium obtained by recalculation of characteristics in Fig. 3

The calculation algorithm for the given characteristics $B_{\parallel}(H, \alpha)$ of the magnetization in the orthogonal direction $B_{\perp}(H, \alpha)$ and the differential magnetic permeability tensor $\mu_d(\mathbf{H})$ remains almost the same as in the case of Cartesian coordinates described above: according to the characteristics $B_{\parallel}(H, \alpha)$, we first determine the three components of the tensor $\mu_d(\mathbf{H})$: $\mu_{dHH} = \partial B_{\parallel} / \partial H$, $\mu_{dH\alpha} = \frac{1}{H} \partial B_{\parallel} / \partial \alpha = \mu_{d\alpha H} = \frac{1}{H} \partial (H \cdot B_{\perp}) / \partial H$. Then, by integration according to expression (15), we find the values $H \cdot B_{\perp}(H, \alpha)$ for all $H = \text{const}$ and, finally, the values of the missing component $\mu_{d\alpha\alpha} = \frac{1}{H} \partial B_{\perp} / \partial \alpha$.

The validity of the obtained results is confirmed by numerical calculations. For previously accepted values of the magnetic field strength vector $\mathbf{H}^{(1)} = (450, 600)$ A/m = $(H, \alpha) = (750$ A/m, $39.06^\circ)$ and $\mathbf{H}^{(2)} = (1120, 375)$ A/m = $(1181$ A/m, $8.758^\circ)$ calculated values of the corresponding magnetic flux density vectors $\mathbf{B}^{(1)} = (B_{\parallel}, B_{\perp}) = (1.574, 0.392)$ T and $\mathbf{B}^{(2)} = (1.666, 0.283)$ T. Exact values of magnetic flux density vectors obtained using analytical formulas from [8]: $\mathbf{B}^{(1)*} = (1.573, 0.394)$ T, $\mathbf{B}^{(2)*} = (1.666, 0.286)$ T.

In conclusion, we note that the integrand in the integral (1) characterizes the change in the density of the co-energy of the magnetic field spent on the cyclic magnetization of the medium. The results obtained can easily be transferred to a similar integral for the energy density $H d\mathbf{B}$, the use of which leads to the vector dependencies $\mathbf{H}(\mathbf{B})$, namely $H_{\parallel}(B_{\parallel}, B_{\perp})$ and $H_{\perp}(B_{\parallel}, B_{\perp})$ or $H_{\parallel}(B, \alpha)$ and $H_{\perp}(B, \alpha)$ depending on the selected coordinate system.

Examples of the use of the results obtained in relation to anisotropic electrical steels will be the subject of special consideration.

Conclusions.

1. The task of constructing the correct vector material equations for nonlinear anisotropic soft magnetic materials remains one of the main reserves for increasing the accuracy of mathematical models in solving magnetostatic problems in the field formulation.

2. An effective direction for solving this problem, which has been actively developing in recent years, is to use the energy approach to constructing the vector characteristics of magnetization. However, the impossibility of directly measuring energy potentials, the complexity of the analytical description and ensuring accuracy with double differentiation to determine the differential magnetic permeability tensor make the task of constructing them quite time-consuming.

3. An alternative technique of constructing the vector characteristics of magnetization is to use the reciprocity principle, which is valid for media with reversible magnetization processes. Its main advantage is the ability to directly recalculate the magnetization characteristics in one of the directions according to the specified magnetization characteristics in the orthogonal direction without calculating the energy potential.

4. The asymptotic expressions for the reciprocity principle established in this paper, which are universal in character for arbitrary magnetic media in the hysteresis-free approximation, open up additional possibilities for optimizing computational processes and increasing the accuracy of numerical methods for solving magnetostatic problems in the field formulation.

REFERENCES

1. Silvester P.P., Gupta R.P. Effective computational models for anisotropic soft B-H curves. *IEEE Transactions on Magnetism*, 1991, vol. 27, no. 5, pp. 3804-3807. doi: **10.1109/20.104930**.
2. Liu J., Basak A., Moses A.J., Shirkoobi G.H. A method of anisotropic steel modelling using finite element method with confirmation by experimental results. *IEEE Transactions on Magnetism*, 1994, vol. 30, no. 5, pp. 3391-3394. doi: **10.1109/20.312666**.
3. Lin D., Zhou P., Badics Z., Fu W.N., Chen Q.M., Cendes Z.J. A new nonlinear anisotropic model for soft magnetic materials. *IEEE Transactions on Magnetism*, 2006, vol. 42, no. 4, pp. 963-966. doi: **10.1109/TMAG.2006.871380**.
4. Sabonnadiere J.C., Meunier G. Modelling nonlinear magnetic materials for field computation. *Journal of Electromagnetic Waves and Applications*, 1990, no. 4, pp. 1027-1054.
5. Bíró O., Außerhofer S., Preis K., Chen Y. A modified elliptic model of anisotropy in nonlinear magnetic materials. *COMPEL - The international journal for computation and mathematics in electrical and electronic engineering*, 2010, vol. 29, no. 6, pp. 1482-1492. doi: **10.1108/03321641011078553**.
6. Higuchi S., Nakao T., Takahashi Y., Tokumasu T., Fujiwara K., Ishihara Y. Modeling of two-dimensional magnetic properties based on one-dimensional magnetic measurements. *IEEE Transactions on Magnetism*, 2012, vol. 48, no. 11, pp. 3486-3489. doi: **10.1109/TMAG.2012.2198878**.
7. Martin F., Singh D., Belahcen A., Rasilo P., Haavisto A., Arkkio A. Analytical model for magnetic anisotropy of non-oriented steel sheets. *COMPEL - The international journal for computation and mathematics in electrical and electronic engineering*, 2015, vol. 34, no. 5, pp. 1475-1488. doi: **10.1108/compel-02-2015-0076**.
8. Tolmachev S., Il'chenko O. Mathematical modelling of magnetic properties of non-linear anisotropic medium in anhysteretic approximation. *Proc. of International Conference Modern electrical and energy systems (MEES 2017)*, November 15-17, 2017, Kremenchuk, Ukraine, pp. 316-319. doi: **10.1109/MEES.2017.8248920**.
9. Tolmachev S.T., Rozhnenko Z.G. The reciprocity principle for a magnetic medium without hysteresis. *Elektrichestvo*, 1992, no. 12, pp. 51-53. (Rus).
10. Tolmachev S., Rozhnenko Z. The theory of the defining equations for nonlinear anisotropic materials. *Proc. of the XIII International Symposium on Theoretical Electrical Engineering ISTE'05*, Ukraine, Lviv, 2005, pp. 97-100.
11. Maergoiz I.D. *Iteratsionnyye metody rascheta staticheskikh poley v neodno-rodnykh, anizotropnykh i nelineynykh sredakh*. [Iterative methods for calculating static fields in inhomogeneous anisotropic and nonlinear media]. Kiev, Naukova Dumka Publ., 1979. 210 p. (Rus).
12. Bortakovskiy A.S., Panteleev A.V. *Lineynaya algebra v primerakh i zadachakh: Uchebnoye posobiye*. [Linear algebra in examples and tasks]. Moscow, Vysshaya shkola Publ., 2005. 509 p. (Rus).

Received 29.10.2019

S.T. Tolmachev¹, Doctor of Technical Science, Professor,
A.V. Il'chenko¹, Candidate of Technical Science, Associate
Professor,

¹ Kryvyi Rih National University,
11, Vitaly Matusevich Str., Kryvyi Rih, Dnipropetrovsk Region,
50027, Ukraine,
e-mail: kafem.knu@gmail.com

How to cite this article:

Tolmachev S.T., Il'chenko A.V. The reciprocity principle for a nonlinear anisotropic medium without hysteresis: theory and practice of application. *Electrical engineering & electromechanics*, 2020, no.2, pp. 40-45. doi: **10.20998/2074-272X.2020.2.06**.

Yu.V. Batygin, E.A. Chaplygin, S.A. Shinderuk

EXPERIMENTAL INVESTIGATION OF THE CURRENT DISTRIBUTION ON THE SHEET BLANK SURFACE IN LINEAR TOOLS OF MAGNETIC-PULSED ATTRACTION

Purpose. The purpose of the present work consists in the characteristics experimental determination of the pulsed current transverse distribution on the surface of a sheet non-magnetic metal between the point contacts of the power source with different geometry of their connection under operating frequencies variation. *Methodology.* The measurements were carried out using methods based on the known positions of electromagnetism. The simulating low-voltage equipment was used, as well as high-voltage power sources with a high level of the stored energy. *Numerical processing of the measurement results was carried out using standard programs from the «Wolfram Mathematica» package.* *Results.* The space-temporal shapes of the pulsed current density transverse distribution on the surface of the sheet blank were obtained and analyzed. It is established that the degree of transverse current concentration in sheet metal relative to the center of the system in the operating frequency range of $\sim 1.8...22$ kHz depends very little on its temporal characteristics. It was found that the level of the transverse current concentration in the conditionally allocated band connecting the contacts of connection depends significantly on the ratio of the width of this band and the transverse dimensions of the contact connection. Moreover, the smallest current is concentrated in a strip whose width is much less than the distance between the contacts ($\leq 11...16$ %). *Originality.* For the first time, the numerical estimates degree of the current transverse concentration are obtained and the dependence of this parameter on the temporal characteristics of the current, as well as on the method of connecting the power source contacts, is established. *Practical value.* The research results will allow creating the new more efficient linear tools of magnetic-pulsed attraction of sheet metals, based on the force interaction of conductors with unidirectional currents. References 10, tables 1, figures 7.

Key words: measurement of the current space-temporal distribution, sheet metal, linear tool, magnetic-pulsed attraction, Rogowski coil.

Метою роботи є експериментальне визначення характеристик поперечного розподілу щільності імпульсних струмів різної частоти на поверхні листового немагнітного металу між точковими контактами джерела потужності при різній геометрії їх підключення. Методика. Виміри проводилися за допомогою методів, заснованих на відомих положеннях електромагнетизму. Використовувалося модельне низьковольтне обладнання, а також високовольтні джерела потужності з високим рівнем енергії, що запасасться. Чисельна обробка результатів вимірювань проводилася за допомогою стандартних програм з пакету «Wolfram Mathematica». *Результати.* Отримано і проаналізовано просторово-часові форми поперечного розподілу щільності імпульсного струму на поверхні листової заготовки. *Наукова новизна.* Вперше отримано чисельні оцінки ступеня поперечної концентрації струму і встановлено залежність даного параметру від часових характеристик струму, а також від способу підключення контактів джерела потужності. *Практичне значення.* Результати досліджень дозволяють створювати нові більш ефективні лінійні інструменти магнітно-імпульсного притягання листових металів, що засновані на силовій взаємодії провідників з односпрямованими струмами. Бібл. 10, табл. 1, рис. 7.

Ключові слова: вимірювання просторово-часового розподілу струмів, листовий метал, лінійний інструмент, магнітно-імпульсне притягання, пояс Роговського.

Целью работы является экспериментальное определение характеристик поперечного распределения плотности импульсных токов разной частоты на поверхности листового немагнитного металла между точечными контактами источника мощности при различной геометрии их подключения. Методика. Измерения проводились с помощью методов, основанных на известных положениях электромагнетизма. Использовалось модельное низковольтное оборудование, а также высоковольтные источники мощности с высоким уровнем запасаемой энергии. *Численная обработка результатов измерений проводилась с помощью стандартных программ из пакета «Wolfram Mathematica».* *Результаты.* Получены и проанализированы пространственно-временные формы поперечного распределения плотности импульсного тока на поверхности листовой заготовки. *Научная новизна.* Впервые получены численные оценки степени поперечной концентрации тока и установлена зависимость данного параметра от временных характеристик тока, а также от способа подключения контактов источника мощности. *Практическое значение.* Результаты исследований позволяют создавать новые более эффективные линейные инструменты магнитно-импульсного притяжения листовых металлов, основанные на силовом взаимодействии проводников с однонаправленными токами. Библ. 10, табл. 1, рис. 7.

Ключевые слова: измерение пространственно-временного распределения токов, листовой металл, линейный инструмент, магнитно-импульсное притяжение, пояс Роговского.

Introduction. The technique of high pulsed currents and their magnetic fields is increasingly used in modern industrial technologies for metal forming [1]. This fact is due to the appearance of new alloys with high strength characteristics and low density. As follows from production practice, the established traditional schemes

and the corresponding equipment do not allow, for example, the molding of products from many aluminum-based alloys. An obstacle to the successful implementation of traditional technology is the destruction of the formed samples, since the required

forces significantly exceed the yield strength of their materials. The use of magnetic pulse metal processing (MPMP) methods solves this problem, since with a short-term force action the allowable relative deformations increase significantly [1, 2]. Tools of technologies of this type make it possible to practically realize efficient stamping of products from flat sheet conductors. Obviously, the amplitudes of the excited electrodynamic forces substantially depend on the spatio-temporal distribution of currents flowing in the metal of the object being processed [1]. This fact determines the relevance of the research topic.

A brief review of the literature. Separate attempts at practical testing of linear tools of magnetic-pulsed attraction of specified sections of sheet metals to remove dents in car body covers were first presented by the authors of publications [2, 3]. Continuation of work in this direction is described in research publication [4-6]. Here, for the first time, the theoretical foundations of the effectiveness of tools of this type [4] and technical solutions protected by patents for their design [5] were laid. The authors of [6] performed numerical estimates of the characteristics of magnetic-pulse attraction of metals with low electrical conductivity.

For clarity of the further discussion, we should dwell on the physics of processes in linear tools of magnetic-pulsed attraction, the principle of which is based on the force interaction of conductors with unidirectional currents [7]. Structurally, instruments of this type contain two geometrically parallel conductors connected to the discharge circuit of a high-voltage power source. One of the conductors is the main current lead (an analogue of the inductor in magnetic pulse processing of metals [1, 4]), the second one is the section of sheet metal to be deformed. According to Ampere law, electrodynamic attraction forces arise between parallel conductors with unidirectional currents [7]. With hard mechanical fixation of the main current lead, the dent metal will be attracted to its working surface [2, 3].

A distinctive feature of the presented instruments of attraction is the presence of contact electrical connection of the sheet metal section to be deformed directly to the discharge circuit of a high-voltage power source. In this regard, the issue of the transverse distribution of currents flowing between the contacts of the connection on the surface of the object of power exposure is of particular importance.

The first quantitative estimates of the characteristics of the current density distribution function on the surface of a sheet metal sample between the connection contacts of a high-voltage power source were described in the author's patents [5]. The results of studies of similar issues aimed at creating effective tools for progressive magnetic-pulse technologies for the force processing of metals with different electrophysical characteristics are also presented in [8, 9].

In general, an analysis of well-known publications shows that the results of all previous works require further development.

We concretize the research task. So, the main indicator determining the effectiveness of the force interaction of parallel currents (one in the main current lead, the second on in the metal with a dent) is the degree of their «spreading» in the transverse direction. Obviously, if «spreading» is absent, there is a maximum force of attraction. Otherwise, its integral value decreases. In this regard, the solution of the problem of assessing the characteristics of the spatio-temporal distribution of currents in conductors is necessary to determine, first of all, the capabilities of the method proper, based on the force interaction of magnetic fields of unidirectional parallel currents.

The solution to this problem is possible by experimental evaluation using two different approaches. The first one involves the direct measurement of the surface distribution of the linear current density flowing between the contacts of the connected source. The second one is the measurement of currents flowing in the selected zones of the transverse distribution. The totality of the results of the first and second experimental approaches allows to establish the level of reliability of theoretical estimates.

The goal of the work is the experimental determination of the characteristics of the transverse distribution of the density of pulsed currents of different frequencies on the surface of a sheet of non-magnetic metal between the point contacts of a power source with different connection geometry.

Note that the methodology for conducting these experiments, measurement methods, and numerical processing of the obtained results using the Wolfram Mathematica standard software package were performed in accordance with the methodology and calculation algorithms described in [2, 3, 7, 10].

The equipment and the object of study are shown in Fig. 1:

1. The power source is a low voltage current pulse generator.

2. Digital oscilloscope – PV6501.

3. The matching device is of cylindrical type, providing a decrease in the operating frequencies of the exciting current to values of $\sim 1.5...2$ kHz.

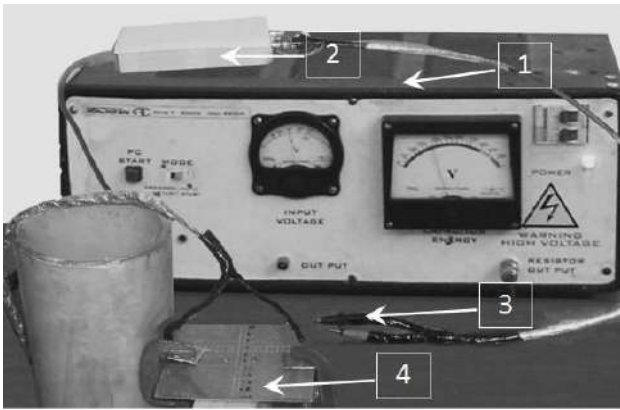
4. The object of study is a sample of sheet non-magnetic steel $\sim (150 \times 150) \cdot 10^{-3}$ m, thickness $\sim 2 \cdot 10^{-3}$ m.

The transverse distribution of the linear current density was measured in the central part of the sheet metal by varying the operating frequencies of the flowing current and various distances between the source connection contacts.

Option No. 1, high-frequency signal. The operating frequency in pulse is ~ 20 kHz. The distance between the contacts is $2H = 0.1$ m and $2H = 0.02$ m.

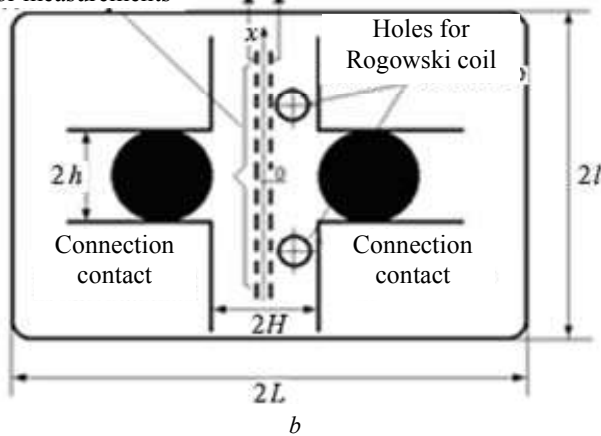
Option No. 2, low-frequency signal. The operating frequency in pulse is $\sim 1.5...2$ kHz. The distance between the contacts is $2H = 0.1$ m and $2H = 0.02$ m. The diameter of the connection contacts is $\sim \varnothing 0.005$ m.

The measurement results are oscillograms of current pulses (Fig. 2).



a

Electrical terminals To meter for measurements

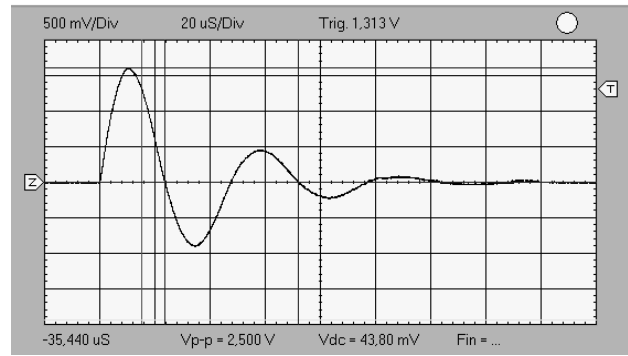


b

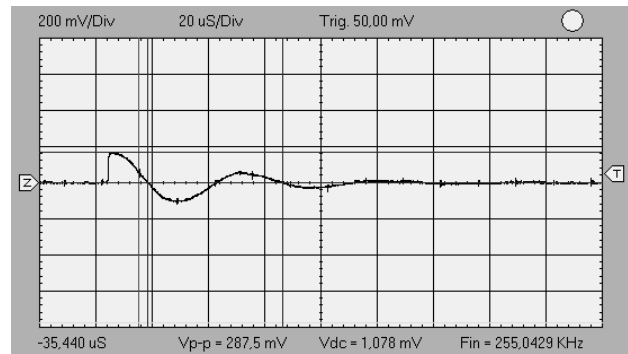
Fig. 1. Experimental equipment and the object of study: *a* – complex for modelling of electromagnetic processes in MPMP: 1 – low-voltage current pulse generator, 2 – oscilloscope, 3 – measuring probes, 4 – sample of sheet non-magnetic steel; *b* – steel sample as an object of study in the adopted experimental scheme

The first thing that should be noted as a feature in the implementation of the experiment is a change in the temporal shape of the current pulse with a decrease in the operating frequency (~ 1.8 kHz, Fig. 2,*c*) in comparison with the signal frequency directly from the source (~ 21.1 kHz, Fig. 2,*a*). This circumstance is due to the influence of the matching device, which, in fact, is a pulse transformer with a primary multi-turn wire winding and a secondary single-turn winding in the form of a thin-walled aluminum cylinder with a longitudinal section. The current induced in a thin-walled metal, as shown by the authors [4], has the form of the time derivative of the current in the primary winding, which is actually illustrated by the oscillograms in Fig. 2,*a* and Fig. 2,*c*.

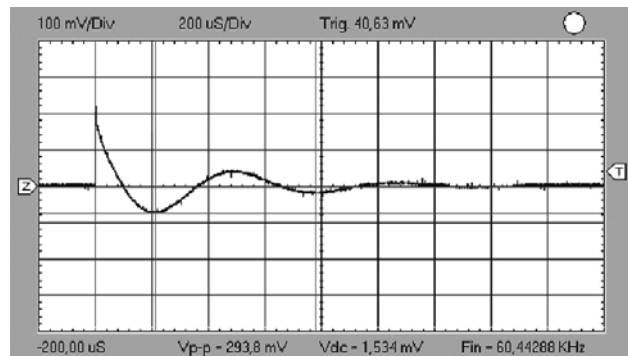
We add that the measurement of the current supplied to the contacts was carried out by voltage oscillography on a low-inductance ohmic shunt connected in series in the source circuit with a load in the form of a sheet metal sample. Here there was an active, that is, directly proportional, connection between the voltage and the flowing current.



a



b



c

Fig. 2. Oscillograms of current pulses in the experiment: *a* – signal supplied to the contacts, frequency ~ 21.1 kHz; *b* – signal taken from electrical terminals, frequency ~ 21.1 kHz; *c* – signal supplied to the contacts, frequency ~ 1.8 kHz

Transverse distribution of linear current density.

The measured signal was taken from the electrical terminals soldered into the sheet metal according to the geometry in Fig. 2,*b*. The results of measurements at various points were normalized to the central maximum. The final experimental data are presented in relative units (ordinate axis) and are presented as graphical dependencies along the axial line between the source connection contacts (abscissa axis). The absolute abscissa coordinate – $\langle X \rangle$ is normalized to the distance between the source connection contacts, the relative abscissa coordinate – $x_0 = (x / 2H)$ (Fig. 3-6).

Option No. 1, high-frequency signal, $f = 21.1$ kHz.

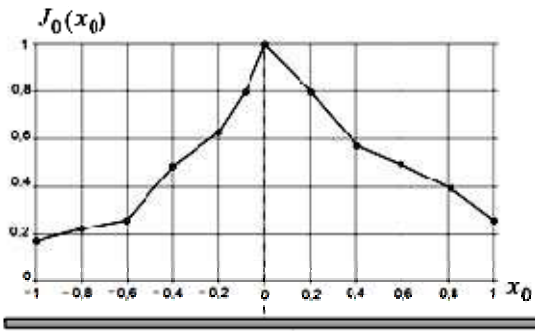


Fig. 3. Linear current density distribution in relative units (normalization to maximum) at $f = 21.1$ kHz, $2H = 0.1$ m

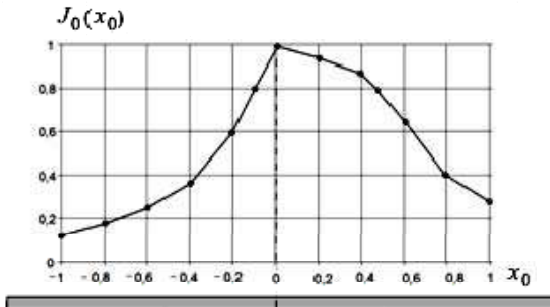


Fig. 4. Linear current density distribution in relative units (normalization to maximum) at $f = 21.1$ kHz, $2H = 0.02$ m

Option No. 2, low-frequency signal, $f = 1.8$ kHz.

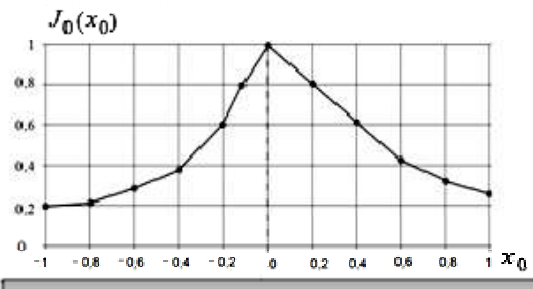


Fig. 5. Linear current density distribution in relative units (normalization to maximum) at $f = 1.8$ kHz, $2H = 0.1$ m

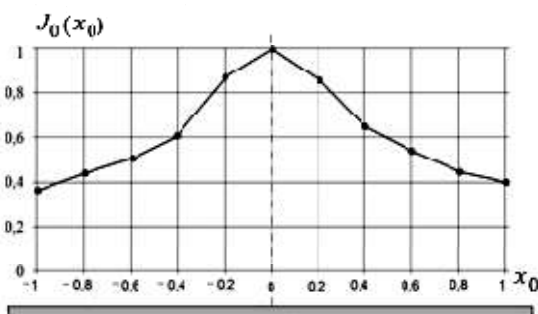


Fig. 6. Linear current density distribution in relative units (normalization to maximum) at $f = 1.8$ kHz, $2H = 0.02$ m

Graphic illustrations of the investigated electromagnetic processes should be supplemented by numerical estimates of the degree of current concentration in the transverse dimension. We denote this indicator by η

and define it as the ratio of the corresponding areas of curvilinear trapezoids (certain integrals)

$$\eta = \frac{S_l}{S_L} \cdot 100\%, \quad (1)$$

where S_l is the area of the curved trapezoid with the base equal to l (l is the length of the selected zone where the current concentration is determined), S_L is the area of the curved trapezoid with the largest base $L = 2H$.

The calculation results are summarized in Table 1.

Table 1

		Degree of current concentration in the selected zone			
No.	Process characteristics	Frequency $f = 21$ kHz		Frequency $f = 1.8$ kHz	
		Dedicated zone $0.1(2H)$	Dedicated zone $0.5(2H)$	Dedicated zone $0.1(2H)$	Dedicated zone $0.5(2H)$
1	$2H = 0.1$ m	$\eta = 11\%$	$\eta = 65\%$	$\eta = 12\%$	$\eta = 56\%$
2	$2H = 0.02$ m	$\eta = 9\%$	$\eta = 71\%$	$\eta = 8\%$	$\eta = 63\%$

A dedicated zone is a section whose center coincides with the reference point on the abscissa axis in the graph of the transverse distribution of the linear current density.

The generalization of the data given in Table 1 shows that in the studied system the degree of transverse concentration of current is determined mainly by the length of the dedicated zone l . For example, in the zone with $l = 0.1$ ($2H$), which, to a first approximation, is much less than the distance between the contacts, on average and regardless of the frequency, $\sim 10\%$ of the flowing current is concentrated. In the zone with $l = 1.0$ ($2H$) equal to the distance between the contacts, again, on average and regardless of the frequency, $\sim 60\text{...}65\%$ of the flowing current is concentrated, $30\text{...}35\%$ of its integral value flows outside this zone.

In general, the analysis of the results of measurements of the transverse distribution of current density revealed the following patterns:

1. Regardless of the temporal parameters of electromagnetic processes, the distance between the contacts has a significant effect on the shape of the transverse distribution of the linear current density flowing between them.

2. As the distance decreases, the distribution becomes more «gentle» (closer to «rectangular»), the maximum value in the center is not pronounced.

3. With an increase in the distance between the contacts, the distribution takes on a «triangular» shape with a pronounced central maximum.

4. When lowering the frequency of the signal in the pulse (regardless of the distance between the contacts of the power supply connection), there is a more intense current spreading across the width of the sheet sample. This fact can be explained by comparing the current distribution over the cross section of the conductor in two limiting physical idealizations. In the case of the skin

effect (ultrahigh frequencies), the current tends to stretch out in a line between the contacts. For direct current (ultra-low frequencies) there is a uniform distribution over the entire volume of the conductor.

5. The degree of concentration of the flowing current relative to the center of the system weakly depends on its temporal characteristics and is determined mainly by the transverse dimensions of the zone where its concentration is considered. Out of the zone with a length equal to the distance between the source connection contacts, about a third of the total current coming into the system flows.

We supplement the obtained results with measurements of the integrated characteristics of current distribution under conditions of connecting a real power source – a high-voltage magnetic-pulse installation.

Model measurements of the linear current density on the surface of the sheet sample illustrated the functional relationships of the degree of concentration of the flowing current and the size of the zone on the transverse axis between the contacts. However, the final quantitative estimates obtained by numerical processing of the results of model experiments require confirmation in real-life conditions of the operation of the tool of magnetic-pulse attraction, when the working currents are tens of thousands of Amperes.

Measuring complex and its features:

1. The measurements were carried out using a Rogowski coil, covering a conductor (sheet sample) with a measured current.

2. The main characteristic of the Rogowski coil is its so-called constant (allows to recalculate the EMF induced in the turns of the coil into a real current flowing through the conductor) – it was $G = 13 \text{ kA/V}$.

3. Through the integrating chain (integrator), the Rogowski coil is connected to a pulsed oscilloscope. Schematically, the measurements are illustrated by the graphics in Fig. 7.

4. According to the oscillograms, the EMF was measured in the Rogowski coil, after which the current in the conductor was determined using the coil's constant.

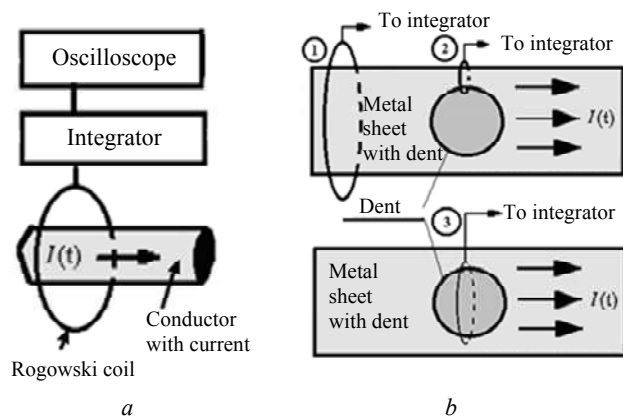


Fig. 7. Schemes for measurement of currents in the experiment: a – current measurement in an arbitrary conductor using the Rogowski coil; b – measurement of currents in sheet metal with a dent

The experiments were conducted on the basis of the power equipment of the Department of Engineering Electrophysics of National Technical University «Kharkiv

Polytechnic Institute» (NTU «KhPI») under the agreement on scientific and technical cooperation between the Department of Physics of Kharkiv National Automobile and Highway University and the Department of Engineering Electrophysics of NTU «KhPI».

Measurements. Results:

1. The measurements were carried out in the operating mode of a magnetic pulse installation with stored energy of 10 kJ – MIU-10 (developed by NTU «KhPI») with working voltage on a capacitive storage $U = 5.5 \text{ kV}$ and operating frequency of the current in the pulse of $\sim 6.75 \text{ kHz}$.

2. The distance between the contacts of the power source connection to the sheet sample was $\sim 0.1 \text{ m}$.

3. The sheet sample in the transverse direction is divided into sections of equal width: 1 – the whole sample, 2 – sections outside the dent ($\sim 1/3$ of the sample width), 3 – section with the dent ($\sim 1/3$ of the sample width).

4. Currents in sheet metal (in sections) – I_1, I_2, I_3 were measured using the Rogowski coil according to the diagram in Fig. 7,a.

Measurement results. According to the dedicated zones on sheet metal – $I_1 = 32.5 \text{ kA}$, $I_2 = 14.3 \text{ kA}$, $I_3 = 7.8 \text{ kA}$.

Total current in a sheet sample:

– summation of measurement results:

$$I_{1\text{-calc}} = 2I_2 + I_3 = 36.4 \text{ kA};$$

– direct measurement:

$$I_{1\text{-meas}} \approx 32.5 \text{ kA}.$$

The reliability level of the measurement results, determined by the discrepancy between the calculation and measurement data ($I_{1\text{-calc}}$ and $I_{1\text{-meas}}$), does not exceed $\sim 12\%$, which is quite acceptable for the practice of MPMP [1, 4].

The ratio of currents in the dent and in the blank (concentration index): $\eta = I_3/I_1 = 7.8/32.5 = 24 \%$.

Note that a similar value in model experiments, averaged over frequencies, does not exceed 30 %.

In general, measurements of current distribution on the surface of a sheet sample, carried out under real conditions of connection to a high-voltage power source, did not reveal significant deviations in the assessment of the degree of concentration of the flowing current as a function of the dedicated size of the zone along the transverse axis between the contacts from the results of model experiments.

Conclusions.

1. It is found that the degree of transverse concentration of current in sheet metal relative to the center of the system in the range of operating frequencies $\sim 1.8...22 \text{ kHz}$ very weakly depends on its temporal characteristics.

2. It is substantiated that the level of the transverse concentration of current in a conventionally allocated strip connecting the connection contacts substantially depends on the ratio of the width of this strip and the transverse dimensions of the contact connection. The smallest current is concentrated in a strip whose width is much less than the distance between the contacts ($\leq 11...16 \%$).

3. It is shown that when the distance between the contacts connecting the source decreases, the degree of concentration of the transverse current flow increases. With a sufficiently small distance (approximately equal to the width of the actual contacts), the concentration level can reach values of ~ 65...80 %.

4. For the first time, experimentally substantiated results of a numerical estimation of the degree of transverse concentration of current on the surface of a sheet blank in linear tools of magnetic pulse attraction are obtained, the dependence of this parameter on the temporal characteristics of the current, as well as on the method of connecting the contacts of the power source is determined, which allows to create new, more efficient linear tools of magnetic-pulse attraction of sheet metals, based on the force interaction of conductors with unidirectional currents.

REFERENCES

1. Psyk V., Risch D., Kinsey B.L., Tekkaya A.E., Kleiner M. Electromagnetic forming – A review. *Journal of Materials Processing Technology*, 2011, vol. 211, no. 5, pp. 787-829. doi: **10.1016/j.jmatprotec.2010.12.012**.
2. Bondarenko A.Y., Finkelshtein V.B., Stepanov A.A. Experimental approbation of an electrodynamic direct electric system for external automobile body repair. *Electrical engineering & electromechanics*, 2014, no. 4, pp. 50-52. (Rus). doi: **10.20998/2074-272X.2014.4.09**.
3. Bondarenko A.Yu., Finkelshteyn V.B., Gavrilova T.V. External straightening basket of the motor transport by means of electro dynamic of the systems at direct drive pulsed current. *Bulletin of NTU «KhPI». Series: Car- and tractorbuilding*, 2014, no. 9 (1052), pp. 66-72. (Rus).
4. Batygin Yu., Barbashova M., Sabokar O. *Electromagnetic metal forming for advanced processing technologies*. Springer International Publ. AG, 2018. 93 p. doi: **10.1007/978-3-319-74570-1**.
5. Batygin Yu.V., Chaplygin E.A., Shinderuk S.A., Strelnikova V.A. The main inventions for technologies of the magnetic-pulsed attraction of the sheet metals. A brief review. *Electrical engineering & electromechanics*, 2018, no. 3, pp. 43-52. doi: **10.20998/2074-272X.2018.3.06**.
6. Batygin Yu.V., Chaplygin E.A., Shinderuk S.A., Strelnikova V.A. Numerical estimates of currents and forces in linear tools of the magnetic-pulse attraction of metals. Part 1: Low electrical conductance metals. *Electrical engineering & electromechanics*, 2019, no. 5, pp. 40-44. doi: **10.20998/2074-272X.2019.5.07**.
7. Griffiths D.J. *Introduction to Electrodynamics. 4th Edition*. Cambridge University Press. United Kingdom, 2017. 620 p.
8. Batygin Yu.V., Chaplygin E.A., Shinderuk S.A. Calculation of fields and currents in the induction system with the attractive screen and the additional coil as a tool for the straightening. *Electrical engineering & electromechanics*, 2015, no. 1, pp. 57-62. (Rus). doi: **10.20998/2074-272X.2015.1.11**.
9. Imbert J.M., Winkler S.L., Worswick M.J., Olivera D.A., Golovashchenko S. The effect of tool-sheet interaction on damage evolution in electromagnetic forming of aluminum alloy sheet. *Journal of Engineering Materials and Technology*, 2005, vol. 127, no.1, pp. 145-153. doi: **10.1115/1.1839212**.
10. Gnatov A., Argun S., Ulyanets O. Joint innovative double degree master program «Energy-saving technologies in transport». *2017 IEEE First Ukraine Conference on Electrical and Computer Engineering (UKRCON)*, May 2017. doi: **10.1109/ukrcon.2017.8100442**.

Received 04.07.2019

Yu.V. Batygin¹, Doctor of Technical Science, Professor,
E.A. Chaplygin¹, Candidate of Technical Science, Associate Professor,
S.A. Shinderuk¹, Candidate of Technical Science, Associate Professor,
¹ Kharkiv National Automobile and Highway University,
25, Yaroslava Mudrogo Str., Kharkov, 61002, Ukraine,
phone +380 57 7003852,
e-mail: yu.v.batygin@gmail.com; chaplygin.e.a@gmail.com;
s.shinderuk.2016102@ukr.net

How to cite this article:

Batygin Yu.V., Chaplygin E.A., Shinderuk S.A. Experimental investigation of the current distribution on the sheet blank surface in linear tools of magnetic-pulsed attraction. *Electrical engineering & electromechanics*, 2020, no.2, pp. 46-51. doi: **10.20998/2074-272X.2020.2.07**.

G.V. Bezprozvannykh, I.A. Kostiukov

A METHOD OF WAVELET ANALYSIS OF TIME SERIES OF PARAMETERS OF DIELECTRIC ABSORPTION OF ELECTRICAL INSULATING STRUCTURES

Introduction. In the objects of control there are always a number of interfaces, for example, solid insulation – electrode. On contacting surfaces, free surface charges are transferred. Surface conductivity leads to fluctuations in the measured values of the capacitance and the tangent of the dielectric loss angle of solid insulation, the state of which is determined. The drain off of the surface charge does not lead to a decrease in the scatter of the measured dielectric absorption parameters. One of the main reasons for the significant time spread of the dielectric absorption parameters, and to a large extent (three orders of magnitude) of the dielectric loss tangent are tribo charges caused by triboelectrification of cable structural elements. Tribo charges cause internal noise in electrical insulating structures, masking processes in the polymer insulation itself. *Purpose.* Substantiation of a method for analyzing the time series of dielectric absorption parameters, which provides increased accuracy of control and diagnostics of solid polymer insulation of electrical insulating structures based on filtering experimental data using wavelet transform. *Methodology.* The inefficiency of filtering the spectra of time series using a low filter based on the direct Fourier transform is shown. Multilevel wavelet decomposition of the time series of parameters is presented, and the efficiency of applying wavelet transforms to identify high-frequency and low-frequency components in the measured values. *Practical value.* The method of analyzing the time series of dielectric absorption parameters using the wavelet transform, proposed for the first time, makes it possible to increase the accuracy of monitoring and diagnostics of solid polymer insulation both at the manufacturing stage and in the operation of electrical insulating structures. This method is the basis for creating a database of control results for assessing the state of solid polymer insulation of electrical insulation structures, in particular, power and information cables. References 17, figures 8.

Key words: dielectric absorption parameters, capacitance, dielectric loss tangent, spectrum of time series, low-pass filter, decomposition levels, approximation and detail, wavelet transform.

Встановлено вплив поверхневих і трібозарядов на результати контролю ємності і тангенса кута діелектричних втрат екранованих і неекранованих кабелів з полімерною ізоляцією. Показана неефективність фільтрації спектрів часових рядів за допомогою фільтра низьких частот на основі прямого перетворення Фур'є. На прикладі неекранованого кабелю представлено багаторівневе вейвлет розкладання часових рядів параметрів і показана ефективність застосування вейвлет перетворення для виявлення високочастотних і низькочастотних компонент у виміряних значеннях. Обґрунтовано оптимальний рівень розкладання параметрів діелектричної абсорбції неекранованого і екранованого кабелів за допомогою вейвлета Добішиї 12 порядку. Доведено ефективність методу вейвлет аналізу часових рядів параметрів діелектричної абсорбції щодо підвищення точності контролю та діагностики твердої полімерної ізоляції електроізоляційних конструкцій. Бібл. 17, рис. 8.

Ключові слова: параметри діелектричної абсорбції, ємність, тангенс кута діелектричних втрат, спектр часових рядів, фільтр низьких частот, рівні розкладання, апроксимація та деталізація, вейвлет перетворення.

Установлено влияние поверхностных и трибозарядов на результаты контроля емкости и тангенса угла диэлектрических потерь экранированных и неэкранированных кабелей с полимерной изоляцией. Показана неэффективность фильтрации спектров временных рядов с помощью фильтра низких частот на основе прямого преобразования Фурье. На примере неэкранированного кабеля представлено многоуровневое вейвлет разложение временных рядов параметров и показана эффективность применения вейвлет преобразования для выявления высокочастотных и низкочастотных компонент в измеренных значениях. Обоснован оптимальный уровень разложения параметров диэлектрической абсорбции неэкранированного и экранированного кабелей с помощью вейвлета Добышии 12 порядка. Показана эффективность метода вейвлет анализа временных рядов параметров диэлектрической абсорбции, обеспечивающего повышение точности контроля и диагностики твердой полимерной изоляции электроизоляционных конструкций. Библ. 17, рис. 8.

Ключевые слова: параметры диэлектрической абсорбции, емкость, тангенс угла диэлектрических потерь, спектр временных рядов, фильтр низких частот, уровни разложения, аппроксимация и детализация, вейвлет преобразование.

Introduction. Monitoring and diagnostics of electrical insulating structures with high-quality solid polymer insulation according to dielectric absorption parameters requires equipment with increased sensitivity and high selectivity of measurements [1-4]. In the objects of control there are always a number of interfaces, for example, insulation – electrode, insulation – insulation. On contacting surfaces, free surface charges are transferred. Surface conductivity leads to fluctuations in the measured values of the capacitance and the tangent of

the dielectric loss angle of solid insulation, the state of which is determined. Surface conductivity causes its own internal noise, significantly affecting the control results [4]. To reduce the effect of surface charges, all current-carrying parts of the structure are grounded before measurements. The time required for the surface charge to drain off is commensurate with the self-discharge time constant of the insulation [4].

Problem definition. The drain of the surface charge does not lead to a decrease in the scatter of the measured dielectric absorption parameters (Fig. 1). Figure 1 shows the results of measurements of the electric capacitance (Fig. 1,*a*) and the dielectric loss tangent (Fig. 1,*b*) of a shielded single-core power high-voltage cable: curves 1 correspond to measurements without draining surface charges; curves 2 – with a charge drain. The measurements were performed at frequency of 120 Hz, for which the effect of free charge carriers on the measurement results is most pronounced in comparison with the data obtained at frequency of 1 kHz [4].

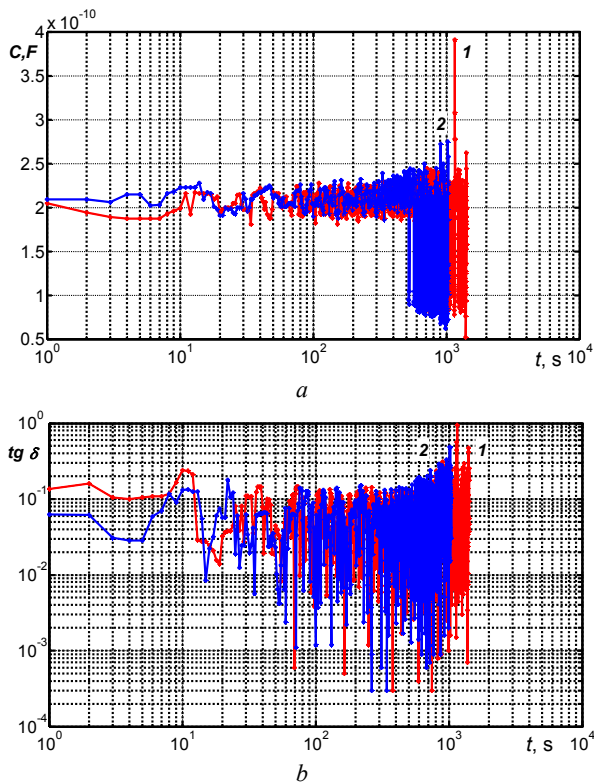


Fig. 1. The effect of drain off of surface charges on dielectric absorption parameters in the power cable

Obviously, one of the main reasons for the significant time spread of the dielectric absorption parameters, and to a large extent (three orders of magnitude) of the dielectric loss tangent (see Fig. 1,*b*), are tribo charges caused by triboelectrification of cable structural elements [5, 6] which is confirmed by the results of measurements of the contact potential difference (Fig. 2) [5-7]. The registration of the contact potential difference is the base of the diagnostics of surface properties of polymer solid insulation of cables [4-7].

Due to the presence of tribo charges, a double electric layer arises [8], and hence an additional electric capacitance. The value of the additional capacity is determined by the electrophysical properties of the solid insulation, the state of its surface, the presence of impurities, etc. [8]. Tribo charges cause internal noise in electrical insulating structures, masking processes in the polymer insulation itself (see Fig. 3).

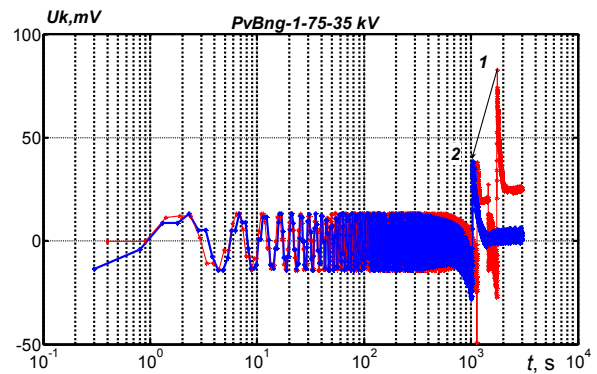


Fig. 2. Contact potential difference in the power cable with cross-linked polyethylene insulation before drain off (curve 1) and after drain off (curve 2) of surface charges

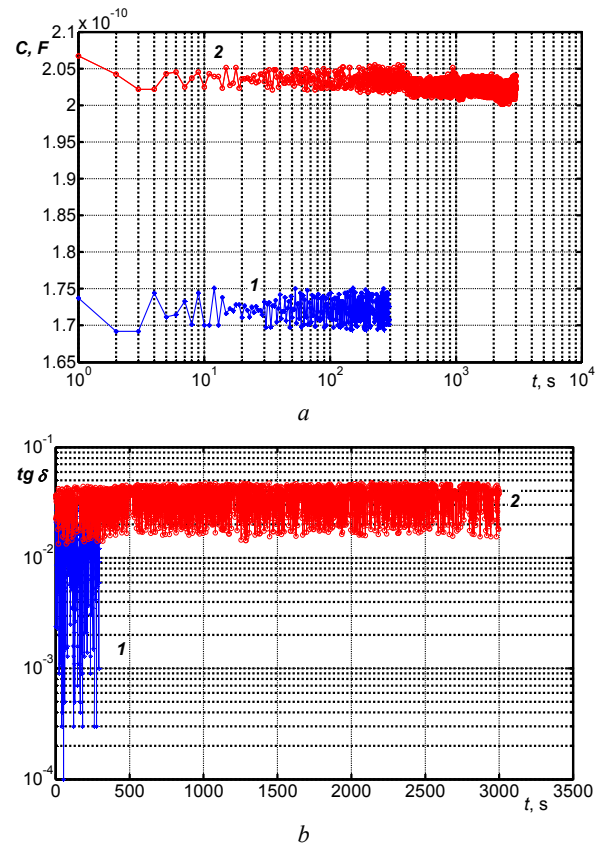


Fig. 3. The effect of tribo charges on the results of the control of polyethylene insulation by the electric capacity (a) and the dielectric loss tangent (b) in the initial state (curve 1) and after thermal radiation aging (curve 2) of the power cable

On the other hand, during long-term measurements, slow fluctuations of the results of measurements of the dielectric absorption parameters, i.e. flicker noise (Fig. 4), the more noticeable, the longer the observation interval [4, 6] are manifested. The regularity of such noise is the increase in amplitude inversely with the frequency (harmonic number K) (see Fig. 4). There is also thermal noise (Johnson noise) due to the thermal motion of charge carriers in the conductors of electrical insulating structures, resulting in a fluctuating potential difference at its ends [4].

The goal of the paper is substantiation of a method for analyzing the time series of dielectric absorption

parameters, which provides increased accuracy of control and diagnostics of solid polymer insulation of electrical insulation structures based on filtering experimental data using wavelet transform.

Filtering the time series of dielectric absorption parameters using the Fourier transform. The presence of noise in the results of measurements of dielectric absorption parameters predetermines the mathematical processing of data using the direct and inverse Fourier transform [9-14].

The direct Fourier transform results in a spectral function (Fig. 4, 5). The Fourier transform is aimed at identifying the harmonic components of the time series, while the time series is decomposed into components in the form of sines and cosines. Then, a comparison is made of the studied sample and its response to the harmonic function by calculating the correlation. If, as a result of the comparison, it was found that there is a correlation, this means that the process contains components of the selected frequency. Then the frequency of the harmonic function changes, and the comparison procedure is repeated.

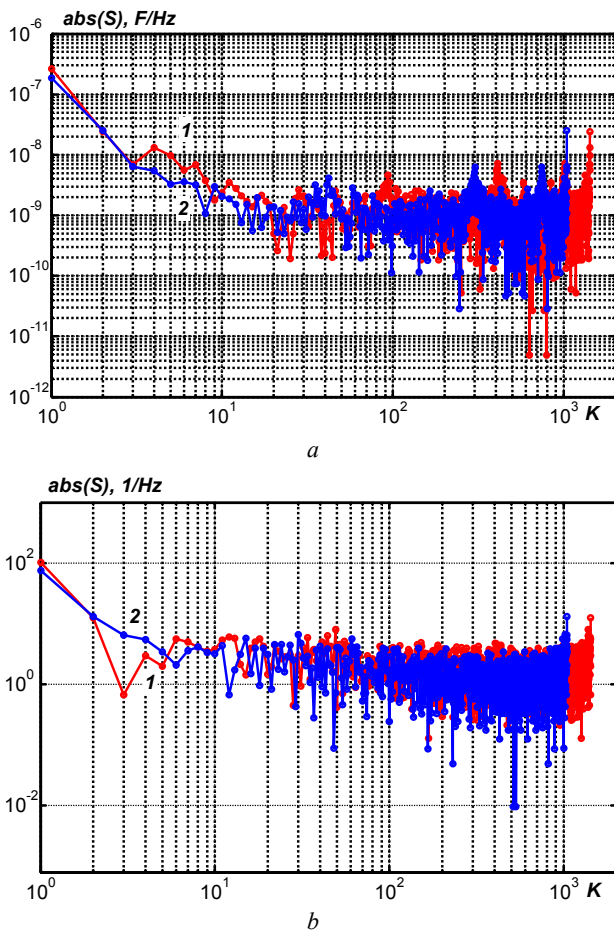


Fig. 4. Spectra of the electric capacitance (a) and the dielectric loss tangent (b) of the power cable with polyethylene cross-linked insulation before drain off (curve 1) and after drain off (curve 2) of surface charges

Figure 5 shows the time series of the dielectric absorption parameters of twisted pairs of unshielded

(Fig. 5,a) and shielded (Fig. 5,b) cables of category 5e. The spectra of the time series of the capacitance are presented in Fig. 6,a,c – curves 1 for unshielded (Fig. 6,a) and shielded (Fig. 6,c) cables, respectively. The spectra of the time series of the dielectric loss tangent are shown in Fig. 6,b,d – curves 1 for unshielded (Fig. 6,b) and shielded (Fig. 6,d) cables, respectively. Filtering the spectra of the time series of the dielectric absorption parameters using a low-pass filter of the 8th (curves 2), the 12th (curves 3) and 24th (curves 4) orders leads to a decrease in noise in the measurement results, but does not exclude the flicker component of noise and distorts the results, especially in the high-frequency region (see curves 1-4 in Fig. 6).

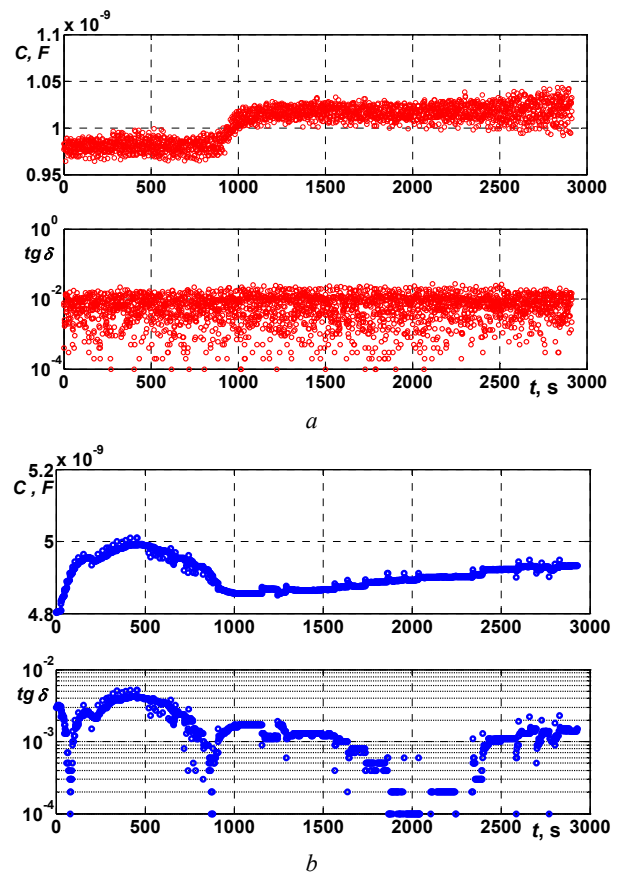


Fig. 5. Time series of parameters of dielectric absorption of twisted pairs of unshielded (a) and shielded (b) cables

Accurate restoration of the time series of dielectric absorption parameters after the direct and inverse Fourier transforms is practically impossible, in particular due to the appearance of the Gibbs effect – spreading of the spectrum [11-13]. The reason for the spreading of the spectrum is the lack of time localization of the sine and cosine functions used in the Fourier series.

To improve localization in time, for example, the window Fourier transform method is used. As the window functions, the Hanning, Blackman, Bartlett-Hann, Gaussian functions (S-transform or Stockwell transform) are widely used [11-13]. But it is not possible to achieve at the same time high frequency and time resolution due to the Heisenberg uncertainty principle.

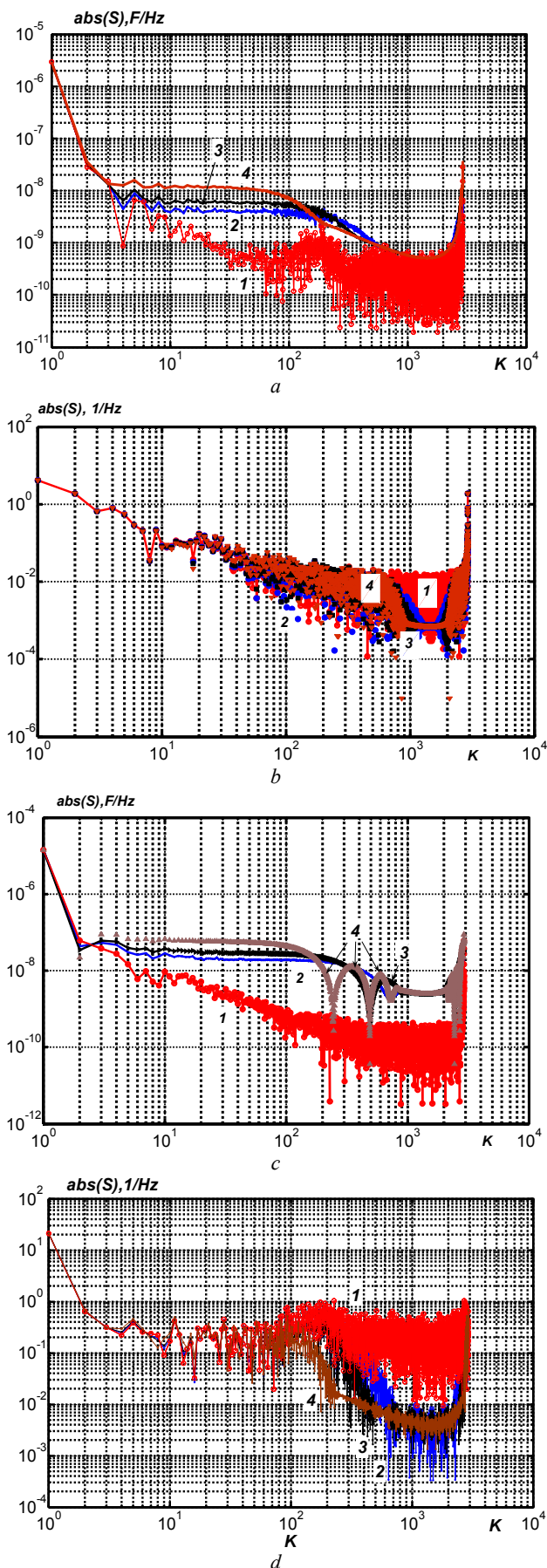


Fig. 6. On the efficiency of measured parameters filtration based on the direct Fourier transform

Approximation and detailing of time series of dielectric absorption parameters using wavelet transform. Considering that at certain points in time, the measured parameters (see Fig. 1, Fig. 3, 4) change stepwise, which leads to poor approximation by trigonometric functions, it becomes necessary to use other transforms, for example, wavelet transform [14, 15].

Figure 7 shows the process of a multi-level wavelet decomposition of time series of a capacitance (Fig. 7,a,b for 4-level and 6-level decomposition, respectively) and the dielectric loss tangent (Fig. 7,c,d for 4-level and 6-level decomposition, respectively) of unshielded cable based on twisted pairs (Fig. 5,a).

Such a decomposition process is a multiple alternation of subband filtering and a decrease in the number of samples. A halving of the number of samples means a halving of the quantization frequency, that is, a halving of the frequency scale (see Fig. 7). This is a common requirement for filters used in wavelet decomposition. On the left, approximations of time series (low-frequency components) are shown. On the right are the details (high-frequency). In MATLAB, a vector with approximation coefficients is denoted by cA_j , and a vector with detail coefficient is denoted by cD_j [13]. The first part of the output vector is a set of half-sums of paired samples of time series and is a coarsened version of the original time series, which are “thinned out” twice in frequency, i.e. this is an approximation of the original time series. The second part is the half-differences of paired samples and is a set of complementary (detailing) information that is necessary to restore the original time series, i.e. detailing.

When restoring time series, first in the sequence of approximating and detailing coefficients zero elements are added, and then for each consequence its own filter is used to reconstruct the measured values.

Wavelet analysis of time series of dielectric absorption parameters of electrical insulating structures. The detection of local features or the allocation of individual sections in the experimental data is necessary at the stage of analysis. The wavelet transform provides extended information about the measurement results, which is achieved by filtering the initial data from random interferences, noise, outliers, non-linear distortions (see Fig. 7).

For a complete reconstruction of the time series of dielectric absorption parameters, only orthogonal wavelets with a compact carrier can be applied, for example, Daubechies family wavelets [16]. The advantage of this type of wavelets over others is that their use does not introduce additional redundancy in the initial data, and time series can be completely restored using quadrature mirror filters.

This type of wavelets is calculated using iterative expressions, and the form depends on the degree of the polynomial and the number of calculated coefficients [14, 15].

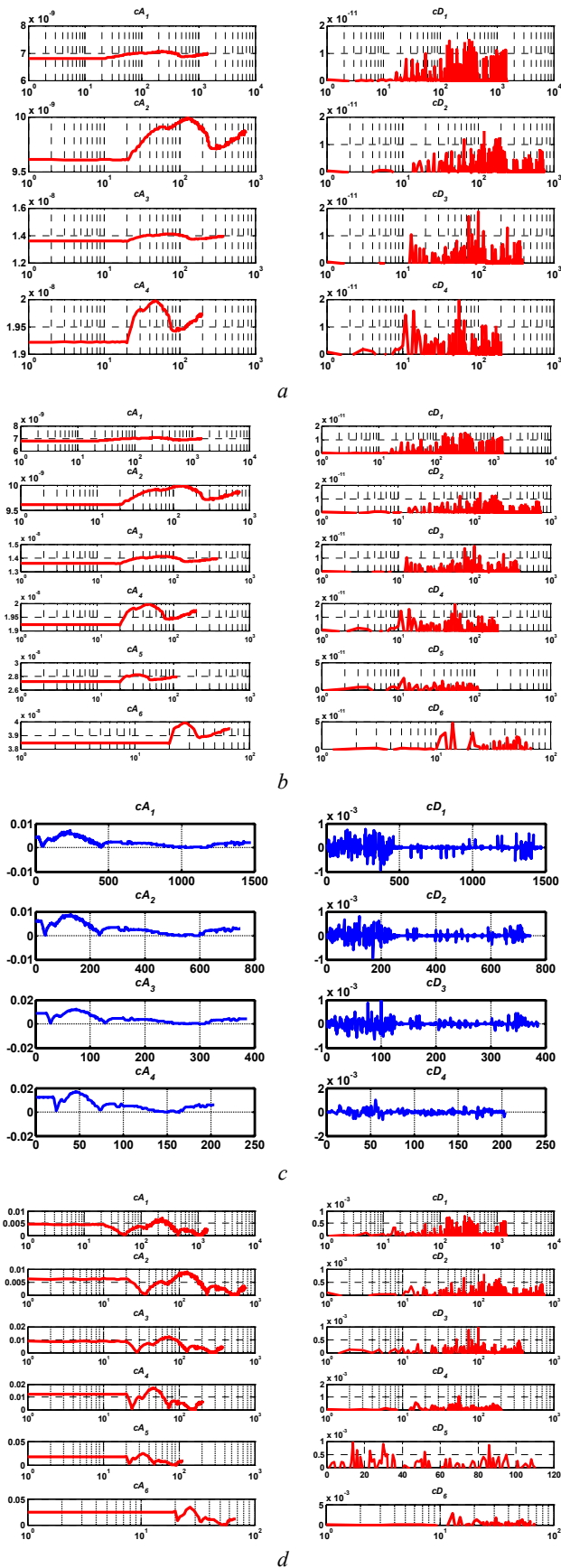


Fig. 7. Multilevel expansion using the Daubechies wavelet of the 12th orders of the time series of dielectric absorption parameters

At high wavelet orders, the filter granularity increases, thereby filtering quality increases due to a steeper amplitude-frequency characteristic, but the computational volume at the transform also increases.

With a decrease in the order (window width) of the wavelet, the transform selects more and more high-frequency components, but the amplitude-frequency characteristic is more gentle (compare Fig. 7,c and Fig. 7,d).

Figure 8 shows the results of filtering the time series of the dielectric absorption parameters of twisted pairs of unshielded (Fig. 8,a,b) and shielded (Fig. 8,c,d) cables using a 12-order Daubechies wavelet with different levels of decomposition. Here, each level of decomposition is a filter that covers a certain range, regardless of the type of data being analyzed.

For an unshielded cable, the time series of the capacitance are presented in Fig. 8; of the dielectric loss tangent – in Fig. 8,b. The curves correspond to: 1 – initial data; 2 – decomposition using the Daubechies wavelet of the 12th order with decomposition level of 4; 3 – decomposition level is 10; 4 – decomposition level is 14.

For a shielded cable, the time series of the capacitance are shown in Fig. 8,c; of the dielectric loss tangent – in Fig. 8,d. The curves correspond to: 1 – initial data; 2 – decomposition using the Daubechies wavelet of the 12th order with decomposition level of 4; 3 – decomposition level is 8.

The presence of the shield causes less noise when measuring the dielectric absorption parameters of the shielded cable and, of course, with a lower value of the decomposition level, more efficient filtering is observed compared to unshielded cable (compare curves 4 and 2 in Fig. 8,a,b and Fig. 8,c,d, respectively).

The reconstructed time series of the dielectric absorption parameters of an unshielded cable (see Fig. 8,a,b) at a decomposition level of 14 are consistent with the average capacitances of $4.909 \cdot 10^{-9}$ F and the dielectric loss tangent of 0.001433 [17].

Conclusions.

Based on long-term measurements, the effect of surface and tribo charges on the results of monitoring the capacitance and the tangent of the dielectric loss angle of power and information cables with polyethylene insulation is established. The scatter of the measured values of the dielectric loss tangent due to the influence of tribo charges can reach three (for newly manufactured) – one (aged in operation ones) orders, which makes it difficult to control the state of polymer insulation.

The inefficiency of filtering the spectra of time series using a low-pass filter based on the direct Fourier transform is shown. Significant distortion of the results in the high-frequency region, especially when using high-order filters, has been established.

Using an unshielded cable as an example, a multilevel wavelet expansion of the time series of parameters is presented. The efficiency of applying the wavelet transform to identify high-frequency and low-frequency components in the measured values is shown.

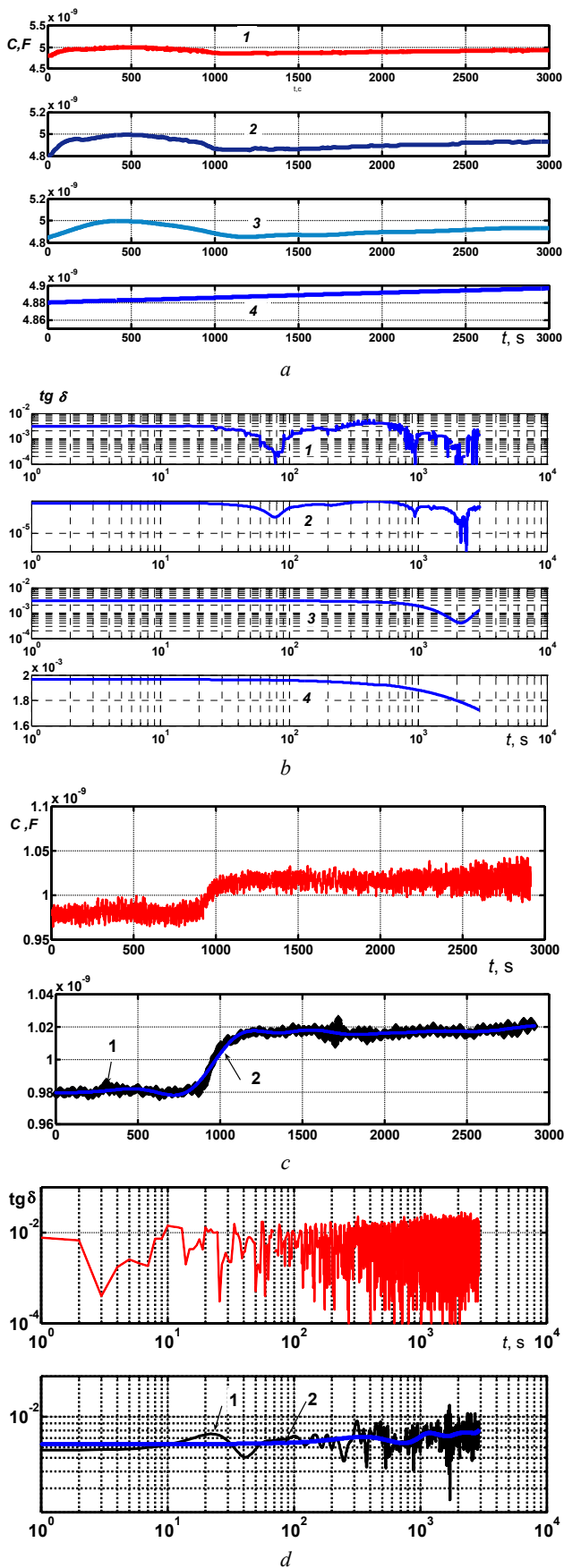


Fig. 8. On the selection of the optimal level of decomposition of the measured values of the dielectric absorption parameters of unshielded (a,b) and shielded (c,d) cables using a 12-order Daubechies wavelet

The optimal level of decomposition of the measured values of the dielectric absorption parameters of twisted-pair cable of unshielded and shielded cables using the 12-order Daubechies wavelet is substantiated.

The first proposed method for analyzing the time series of dielectric absorption parameters using wavelet transform allows to increase the accuracy of monitoring and diagnostics of solid polymer insulation, both at the manufacturing stage and in the operation of electrical insulating structures. This method is the basis for creating a database of control results for assessing the state of solid polymer insulation of electrical insulation structures, in particular, power and information cables.

REFERENCES

1. Kholodny S.D., Serebryannikov S.V., Boev M.A. *Metody ispytaniy i diagnostiki v elektroizolatsionnoi i kabel'noi tekhnike* [Testing and diagnostic methods in electrical insulation and cable technology]. Publishing House MEI, 2009. 232 p. (Rus).
2. Bezprozvannykh G.V., Roginskiy A.V. Dielectric spectroscopy of casing thermosetting composite electrical insulation system of induction traction electric machines. *Electrical engineering & electromechanics*, 2018, no.1, pp. 17-20. doi: 10.20998/2074-272X.2018.1.02.
3. Bezprozvannykh G.V., Kostyukov I.A., Roginsky A.V. Characteristics of cased electrical insulation system of asynchronous electrical machines at resonance frequency. *Technical electrodynamics*, 2019, no. 4. pp. 48-55. (Rus). doi: 10.15407/techned2019.04.048.
4. Bezprozvannykh G.V., Boyko A.N. Substantiation and guaranteeing of technological parameters of triboelectrical method of monitoring of cables with polymer insulation. *Electrical Engineering & electromechanics*, 2014, no. 6, pp. 56-60. (Rus). doi: 10.20998/2074-272x.2014.6.10.
5. Bezprozvannykh G.V., Boyko A.M. Electrostatic processes in power cables. *Electrical engineering & electromechanics*, 2013, no.4, pp. 27-31. (Ukr).
6. Bezprozvannykh G. V., Boyko A.M. Experimental determination of triboelectric potential in unshielded and shielded network cables. *Electrical engineering & electromechanics*, 2012, no. 3, pp. 56-60. (Ukr).
7. Bezprozvannykh G.V., Boyko A.N. Contact potential difference as a measure of power cable polymer insulation aging. *Electrical engineering & electromechanics*, 2014, no. 5, pp. 62-66. (Rus). doi: 10.20998/2074-272x.2014.5.12.
8. Bezprozvannykh G.V., Boyko A.N. Distribution of surface density of charges on the interface between contacting isolated conductors of the cables. *Technical Electrodynamic*, 2014, no.6. pp. 18-23. (Rus).
9. Ango A. *Matematika dlja elektro- i radioinzhenеров* [Mathematics for electro- and radioengineers]. Moscow, Nauka Publ., 1965. 780 p. (Rus).
10. Korn G., Korn T. *Spravochnik po matematike dlja nauchnykh rabotnikov i inzhenerov* [Mathematical handbook for scientists and engineers]. Moscow, Nauka Publ., 1977. 830 p. (Rus).
11. Sergienko A.B. *Tsifrovaia obrabotka signalov* [Digital signal processing]. St. Petersburg, BHV Publ., 2011. 768 p. (Rus).
12. Potemkin V.G. *Sistema MATLAB* [MATLAB System]. Moscow, DIALOG-MIFI Publ., 1998. 350 p. (Rus).

13. Dyakonov V.P. *MATLAB i SIMULINK dlia radioinzhenerov* [MATLAB and SIMULINK for radio engineers]. Moscow, DMK Press Publ., 2011. 976 p. (Rus).

14. Malla S. *Veivlety v obrabotke signalov* [Wavelets in signal processing]. Moscow, Mir Publ., 2005. 671 p. (Rus).

15. Fraser M. *Vvedenie v veivlety v svete lineinoi algebry* [Introduction to wavelets in the light of linear algebra]. Moscow, BINOM. Laboratory of Knowledge Publ., 2010. 487 p. (Rus).

16. Daubechies I. *Desiat' leksii po veivletam* [Ten lectures on wavelets]. Izhevsk, SIC «Regular and chaotic dynamics» Publ., 2001. 464 p. (Rus).

17. Bezprozvannyh G.V., Kostiukov I.A. Error of control of electrical insulation structures by dielectric absorption parameters according to the concept of uncertainty of measurements. *Electrical engineering & electromechanics*, 2020, no.1, pp. 47-51. doi: 10.20998/2074-272X.2020.1.07.

G.V. Bezprozvannyh¹, Doctor of Technical Science, Professor,
I.A. Kostiukov¹, Candidate of Technical Science,

¹National Technical University «Kharkiv Polytechnic Institute»,
2, Kyrpychova Str., Kharkiv, 61002, Ukraine,
phone +380 57 7076010,
e-mail: bezprozvannyh@kpi.kharkov.ua,
iakostiukow@gmail.com

Received 12.12.2019

How to cite this article:

Bezprozvannyh G.V., Kostiukov I.A. A method of wavelet analysis of time series of parameters of dielectric absorption of electrical insulating structures. *Electrical engineering & electromechanics*, 2020, no.2, pp. 52-58. doi: 10.20998/2074-272X.2020.2.08.

O.O. Palchykov

DETERMINATION OF THE EFFECTIVE PERMITTIVITY OF A HETEROGENEOUS MATERIAL

Purpose. To develop a two-dimensional numerical-field model for determining the effective permittivity of a multicomponent material represented by a system of homogeneous volumes with known physical characteristics. *Methodology.* The model is based on the solution by the finite element method of an electrostatic problem with the subsequent determination of the energy contained in the volume under consideration. Then we have compared this result with the energy of a flat capacitor with a rectangular cross-section of the plates and determined the effective permittivity of test material. We also have used Rayleigh, Odelevsky and Lichtenecker models and the model with a perpendicular arrangement of layers relative to the main electric flux. *Results.* Based on the developed field model, the effective permittivities for dry, wet and transformer oil-soaked insulating papers of various grades, including taking into account ash, are determined. We have proved that a macroscopically homogeneous multicomponent material is well approximated by uniformly spaced cylindrical volumes with a substance of different nature in a matrix of another substance. We have showed a significant error of the layer model and the Rayleigh model relative to the proposed model. We have showed the equivalence of models with the location of inclusions in the nodes of a rectangular and parallelogram mesh. *Originality.* For the first time we have proposed wet paper models with an asymmetric arrangement of a cylindrical volume of water with a circular and segment cross-section in a cylindrical pore. For the first time we have proposed models of insulating paper with evenly spaced cylindrical inclusions of different volumes. *Practical value.* The proposed model allows to calculate the effective permittivity of an inhomogeneous material with a given accuracy without restricting the shape of the components. Based on the proposed field model, it is possible to determine the Lichtenecker index, which allows to calculate the effective permittivity for any ratio of the volumes of the components of a heterogeneous material. References 10, tables 3, figures 4.

Key words: effective permittivity, electrostatic field, energy, finite element method, cylindrical volumes.

Обґрунтовано застосування методу, заснованого на чисельному розрахунку електростатичного поля для визначення ефективної діелектричної проникності гетерогенного матеріалу, який заміняється системою однорідних об'ємів з відомими фізичними характеристиками. Для сухого, вологого і просоченого трансформаторним маслом ізоляційних паперів різних марок визначені діелектричні проникності. Результати розрахунку за запропонованими моделями зіставлялися з результатами, отриманими на основі шаруватої моделі, моделей Релея і Оделевського. Запропоновані апроксимаційні залежності на основі узагальненого виразу Ліхтенеккера для визначення діелектричної проникності ізоляційних паперів. Бібл. 10, табл. 3, рис. 4.

Ключові слова: ефективна діелектрична проникність, електростатичне поле, енергія, метод скінченних елементів, циліндричні об'єми.

Обосновано применение метода, основанного на численном расчете электростатического поля для определения эффективной диэлектрической проницаемости гетерогенного материала, который представляется системой однородных объемов с известными физическими характеристиками. Для сухой, влажной и пропитанной трансформаторным маслом изоляционных бумаг различных марок определены диэлектрические проницаемости. Результаты расчета по предложенным моделям сопоставлялись с результатами, полученными на основе слоистой модели, моделей Рэлея и Оделевского. Предложены аппроксимационные зависимости на основе обобщенного выражения Лихтенеккера для определения диэлектрической проницаемости изоляционных бумаг. Библ. 10, табл. 3, рис. 4.

Ключевые слова: эффективная диэлектрическая проницаемость, электростатическое поле, энергия, метод конечных элементов, цилиндрические объемы.

Introduction. In the manufacture of electrical machines, apparatus and power capacitors, various insulating materials are used, such as multicomponent (varnished fabrics and varnished paper, electrical insulating tapes, laminated plastics, electrical ceramics), and almost uniform ones, such as mica and cellulose papers. The latter, however, contain a large number of cavities that can be filled with atmospheric air and moisture or an impregnating dielectric. Therefore, the permittivity, conductivity and breakdown voltage of insulating materials is a complex function of the presence and placement of certain components in the volume of the dielectric. In this paper, we consider the effect of the composition of an insulating material on its effective permittivity.

Literature review. To calculate the effective permittivity (EP) ε_{eq} of two-component materials, the

formulas of Wiener, Rayleigh, Maxwell, generalized Lichtenecker formula for flat, cylindrical, spherical and granular inclusions [1, 2], as well as the Odelevsky formula for statistical mixtures can be used:

$$(\varepsilon_{\text{eq}} + k)^{-1} V_{\Sigma} = (\varepsilon_1 + k)^{-1} V_1 + (\varepsilon_2 + k)^{-1} V_2; \quad (1)$$

$$(\varepsilon_{\text{eq}} - \varepsilon_1) / (\varepsilon_{\text{eq}} + \varepsilon_2) = (\varepsilon_2 - \varepsilon_1) (\varepsilon_2 + \varepsilon_1)^{-1} V_2 V_{\Sigma}^{-1}; \quad (2)$$

$$\varepsilon_{\text{eq}} = \varepsilon_1 [1 + (3V_2(\varepsilon_2 - \varepsilon_1) / V_{\Sigma}) / (\varepsilon_2 + 2\varepsilon_1 - V_2(\varepsilon_2 - \varepsilon_1) / V_{\Sigma})]; \quad (3)$$

$$\varepsilon_{\text{eq}}^m V_{\Sigma} = \sum_{j=1}^n V_j \varepsilon_j^m; \quad (4)$$

$$\varepsilon_{\text{eq}} = A + \sqrt{A^2 + \varepsilon_1 \varepsilon_2 / 2}, \quad (5)$$

where $\varepsilon_1, \varepsilon_2$ are the permittivities of the components of the material; V_{Σ}, V_1, V_2 are the total volume and volumes of

the components of the material, respectively; k is the Wiener coefficient, $0 \leq k \leq \infty$; n is the number of components of the material; m is the Lichtenecker index, $-1 \leq m \leq 1$; A is the Odelevsky parameter

$$A = [(3V_1/V_\Sigma - 1)\varepsilon_1 + (3V_2/V_\Sigma - 1)\varepsilon_2]/4.$$

The use of formulas (1), (4) is difficult due to the unknown coefficients k and m . Formulas (2), (3) and (5) are derived on the basis of certain assumptions, the violation of which can lead to a significant error.

To determine the EP of impregnated paper, in [3] it is proposed to use a model of series-connected layers, which is a rather rough approximation.

In [4-6], using the double and triple-periodic Rayleigh model, effective material parameters are calculated based on the solution of the static field problem by the method of summing multipole interactions. The field models in these works for reducing infinite sums of interactions to their finite sum are limited only by the nearest neighbors with respect to the chosen inclusion.

Calculation of the EP can be based on the polarization mechanism [7]. This approach is mainly applied only for pure substances with consideration of processes at the ionic and molecular levels. In [8], based on field models, the electrophysical properties of a cement-based composite were explained.

Therefore, a sufficiently accurate determination of the averaged characteristics of the material is based on the solution of the corresponding field model of the system of solid substances located in the volume of the material in accordance with the technology of its manufacture.

The goal of the work is the development of a two-dimensional numerical-field model for determining the EP of a multicomponent material represented by a system of homogeneous volumes with known physical characteristics.

Object of study. A rectangular parallelepiped made of capacitor paper with the following dimensions: length $l = 100 \mu\text{m}$; width $b = 200 \mu\text{m}$; height $h = 14 \mu\text{m}$ for papers KOH 0,8; KOH 2; MKOH 1 or height $h = 12 \mu\text{m}$ for paper CKOH 3,5. Humidity, composition and density of the selected paper grades correspond to [9].

Mathematical model. The main physical properties of the materials needed to build mathematical models for determining the EP of a particular paper are given in Table 1. The temperature of the insulating paper is taken 60°C .

Table 1
Physical properties of dielectric materials

Name	Density, kg/m^3	ε_{20}	$\alpha, 1/^\circ\text{C}$
Cellulose	1530	6.5	$0.5 \cdot 10^{-3}$
Air	1,06	1.00058	$-1.5 \cdot 10^{-6}$
Water	983	80.2	$-4.02 \cdot 10^{-3}$
Transformer oil	856	2.25	$-0.5 \cdot 10^{-3}$

The permittivity of the material at an arbitrary temperature t is determined as

$$\varepsilon = \varepsilon_{20} [1 + \alpha(t - 20)]. \quad (6)$$

The veracity of expression (6) is confirmed by the graphical dependencies shown in Fig. 1 for dry air and water, recommendations in [3] for cellulose and the linear

dependence of the permittivity of transformer oil on temperature within $20 \dots 90^\circ\text{C}$. The assumption of the absence of thermal aging of the material also applies.

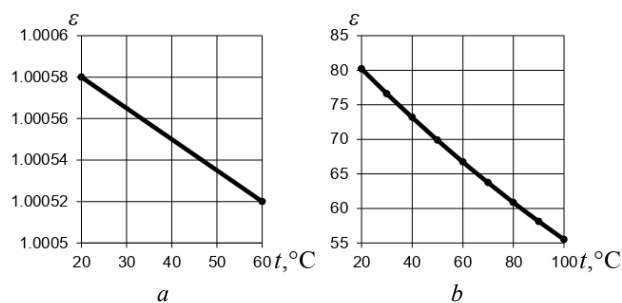


Fig. 1. Dependence of the permittivity of dry air (a) and water (b) on temperature

Real insulating paper is presented as cellulose with cylindrical pores uniformly spaced in its volume. Cross sections of pores are in planes perpendicular to the length of the volume under consideration. Depending on the model formulation, air, air and water, transformer oil may be in the pores.

The volumes of cellulose and pores are found by solving the system of equations:

$$\begin{cases} V_p \rho_p (1 - y) = V_c \rho_c + V_a \rho_a; \\ V_w \rho_w = V_p \rho_p y; \\ V_p = V_c + V_a + V_w, \end{cases}$$

where V_p , V_c , V_a and V_w are the volumes of paper, cellulose, air and water, respectively; ρ_p , ρ_c , ρ_a and ρ_w are the densities of paper, cellulose, air and water, respectively; y is the relative mass content of water in the insulating paper [9].

The electric field in cross section relative to the length of the considered volume of insulating paper is described by the following differential equations [10]:

$$\begin{cases} \varepsilon \nabla^2 \varphi = -\rho; \\ \mathbf{E} = -\nabla \varphi; \\ \mathbf{D} = \varepsilon \mathbf{E}, \end{cases} \quad (7)$$

where φ is the scalar electrostatic potential; ρ is the volume charge density of the domain; \mathbf{E} is the electric field vector; \mathbf{D} is the electric induction vector.

At the interface, the following conditions are satisfied [10]:

$$\begin{cases} \mathbf{n}_{12} \times [\nabla \varphi_1 - \nabla \varphi_2] = 0; \\ \mathbf{n}_{12} \cdot (\varepsilon_1 \nabla \varphi_1 - \varepsilon_2 \nabla \varphi_2) = \sigma; \\ \varphi_1 = \varphi_2; \\ \varepsilon_1 \frac{\partial \varphi_1}{\partial \mathbf{n}_{12}} - \varepsilon_2 \frac{\partial \varphi_2}{\partial \mathbf{n}_{12}} = \sigma, \end{cases} \quad (8)$$

where \mathbf{n}_{12} is the normal from the first to the second medium; σ is the surface charge at the interface between two media.

Equation (7) in a piecewise homogeneous dielectric medium is reduced in each homogeneous region to the Laplace equation, and the permittivities of the regions is included in the solution of the problem only by means of conditions (8).

The second equation of condition (8) at the interfaces between two dielectrics, as well as a dielectric and a conductor, respectively, takes the form:

$$\varepsilon_1 \frac{\partial \varphi_1}{\partial \mathbf{n}_{12}} - \varepsilon_2 \frac{\partial \varphi_2}{\partial \mathbf{n}_{12}} = 0; \quad \varepsilon_1 \frac{\partial \varphi_1}{\partial \mathbf{n}_{12}} = \sigma.$$

On the upper and lower planes perpendicular to the height of the volume under consideration, Dirichlet conditions respectively $\varphi_{d1} = 1.9$ V; $\varphi_{d2} = -1.9$ V are set. The solution domain is limited to a cylindrical surface with a radius of 200 μm , a length of 100 μm , and zero potential on its surface.

After the numerical calculation of the electric field the energy enclosed in the volume of insulating paper is found

$$W = \int_V \frac{1}{2} \mathbf{E} \cdot \mathbf{D} dv = \frac{1}{2} \int_V \varepsilon (\nabla \varphi)^2 dv,$$

where V is the volume over which the integration is performed; v is the elementary volume.

By comparing the calculated energy with the energy of a flat capacitor, we find the EP

$$\varepsilon_{\text{eq}} = \frac{2Wh}{lb(\varphi_{d1} - \varphi_{d2})^2}.$$

The numerical calculation of the electrostatic field by the finite element method is implemented in the FEMM code.

The main assumptions of the model: dielectric materials do not have conductivity; there are no charges at their interfaces; space charges in dielectric materials are

absent, and their volumes do not change under the influence of an electrostatic field; ideal conductors with infinitesimal height are sources of an electrostatic field.

The significant width of the investigated dielectric is explained by the desire to reduce the edge effect. The model was tested by comparing capacitor capacities with sizes 100x200x14 μm and the same thickness of cellulose and air obtained on the basis of the equations of the electrostatic field by the finite element method and on the basis of the analytical expression without taking into account the edge effect. The error in this case was 0.23 %.

The results of the study. To calculate the EP of dry and transformer oil-soaked insulating papers, we used models of uniformly distributed cylindrical volumes filled with air and transformer oil, respectively, in cellulose matrices.

To calculate the EP of wet paper, a model of uniformly distributed cylindrical volumes filled with air and water was proposed, and in this total volume the volume of water was represented as cylindrical with a circular cross section in a cellulose matrix. When determining the volume content of a particular component, the author was based on the structure of wet paper (that is, paper with normal water content [9]), therefore, the pore volume (the sum of the volume of air and water for wet paper) in the models of dry and impregnated paper did not change. The calculated EPs for the indicated models, as well as for the layered model, Rayleigh and Odelevsky models are given in Table 2.

Table 2

Simulation results

Paper grade	Proposed model			Layer model		Rayleigh model	Odelevsky model	Approximation dependence
	Number of pores	Number of model nodes	ε_{eq}	Number of model nodes	ε_{eq}	ε_{eq}	ε_{eq}	ε_{eq}
dry paper								
Paper KOH 0,8	248	662632	3.052	4607	1.682	4.500	2.860	3.052
Paper KOH 2	248	702562	4.370	4749	2.543	5.300	4.456	4.507
Paper MKOH 1	248	693639	3.674	4920	2.048	4.895	3.667	3.783
Paper CKOH 3,5	248	750148	4.966	4872	3.150	5.665	5.114	5.123
wet paper								
Paper KOH 0,8	248	4462060	3.403	5566	1.912	–	–	2.740
Paper KOH 2	248	4877348	5.185	5652	3.503	–	–	5.185
Paper MKOH 1	248	4744585	4.130	5509	2.448	–	–	3.634
Paper CKOH 3,5	248	3782978	6.262	6711	5.095	–	–	6.808
impregnated paper								
Paper KOH 0,8	248	662632	3.949	4607	3.233	4.789	3.914	3.949
Paper KOH 2	248	702562	5.000	4749	4.212	5.525	5.068	5.06
Paper MKOH 1	248	693639	4.453	4920	3.686	5.155	4.503	4.516
Paper CKOH 3,5	248	750148	5.448	4872	4.755	5.835	5.540	5.525

The decrease in the EP values according to the layered model relative to the proposed one is explained by

the need for the entire electric flux to pass through the region with low dielectric constant. The Rayleigh model

also cannot claim to be a good description of the change in the EP when the volumes and properties of the components of the material change and gives overestimated values. The Odelevsky model determines the EP with an accuracy of $-2.98...6.3\%$ and $-1.7...0.9\%$ for dry and impregnated paper, respectively. On the basis of field models and the generalized Lichtenecker formula, approximation dependences are proposed for calculating the EP of insulating papers. The approximation dependences indexes for dry, wet and transformer oil-soaked papers amounted to 0.495; -0.283 and 0.391 , respectively. The EPs calculated by this method are given in Table 2.

The effect of the number of inclusions on the EP value of KOH 2 dry paper is shown in Fig. 2, from which it can be seen that with an increase in the number of uniformly distributed volumes of inclusions, the accuracy of the model increases until it begins to be limited by the accuracy of displaying the boundaries of these volumes.

Consequently, the proposed models for the specified in Table 2 numbers of pores accurately enough allow to determine the EP.

In addition to the above wet paper models, models with a cylindrical volume of water and a sector section, as well as with a cylindrical volume of water, in the cavity of which a cylindrical air volume is coaxially located are considered.

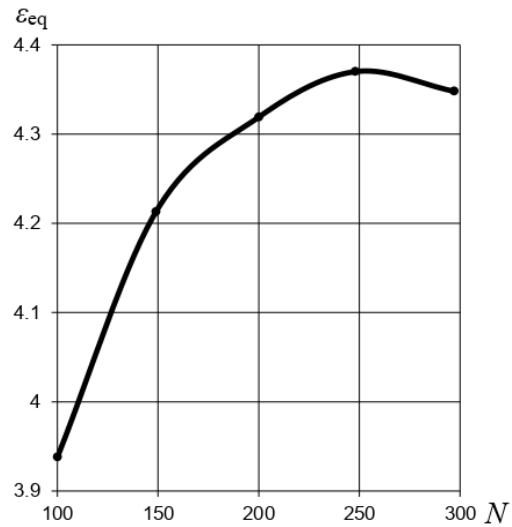


Fig. 2. Dependence of the permittivity on the number of pores of the model of dry paper grade KOH 2

The maximum discrepancy between the EPs calculated for models with a circular and sector section of the water volume was 2.9% , therefore, these models are equivalent. Examples of the distribution of the electrostatic field in these models are shown in Fig. 3, 4.

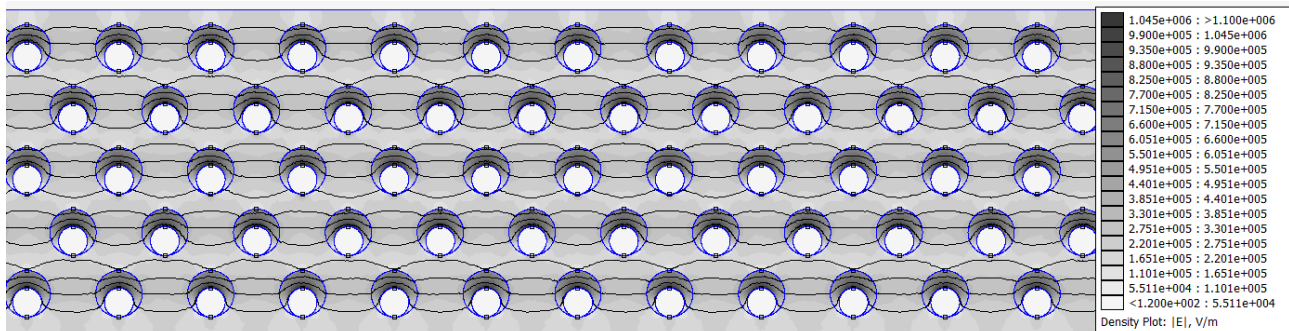


Fig. 3. Distribution of the electrostatic field in the model of wet paper brand KOH 2 with a circular cross section of the volume of water

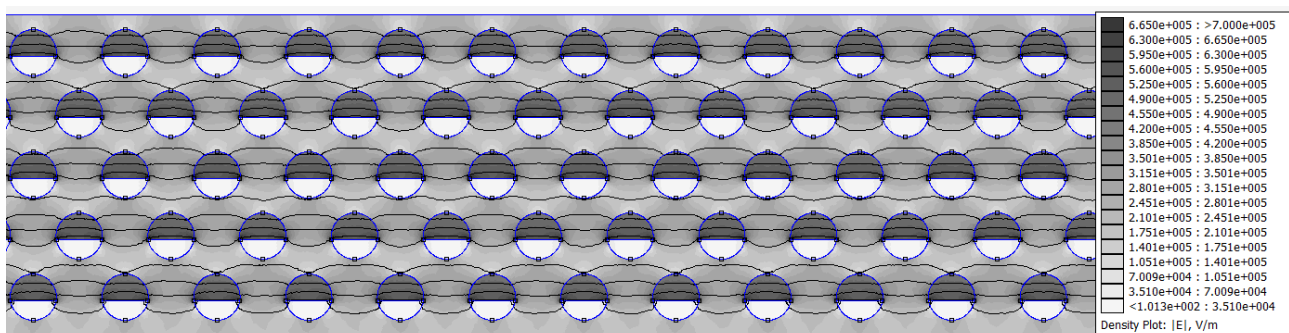


Fig. 4. Distribution of the electrostatic field in the model of wet paper brand KOH 2 with a sector cross-section of the volume of water

As can be seen from Fig. 3, 4, with almost identical EPs, the electric field strength modulus in the air in the first model is greater than in the second one. The EP values determined for models with a hollow cylindrical volume of water are 1.36...1.8 times greater than for a model with a cylindrical volume of circular cross section, which is explained by the formation of a path with an increased permittivity. This model was discarded due to

the presence of a local extremum of the EP value when changing paper grades.

For the KOH 2 dry paper model and pore number 100, the effect of the location of pores at the nodes of a rectangular and parallelogram mesh on the final result was studied. The maximum discrepancy was 0.8% .

It is known that CKOH paper is characterized by a significant, up to 1% , ash content. In the manufacture of

paper calcium sulfate can be considered as ash. The calculated values of the EP of CKOH insulating paper, taking into account ash, are given in Table 3. The error of not accounting of ash was 0.8...1.3 %.

Table 3

CKOH 3,5 paper simulation results
with ash inclusions 1 %

Paper type	Number of pores	Number of inclusions of ash	Number of model nodes	ϵ_{eq}
Dry	248	49	843735	4.925
Wet	248	49	3997067	6.182
Impregnated	248	49	843735	5.415

Conclusions.

1. The principal possibility of describing the permittivity of a mixture of components on the basis of field models with the known permittivity of each component, their volumetric content and the features of their location is shown. Field models have been developed for determining the EP of dry, wet, and transformer oil-soaked insulating papers.

2. The adequacy of the developed models is confirmed by the following: with an increase in the number of cylindrical volumes inside the matrix, the EP asymptotically tends to a certain finite value.

3. The layered model and the Rayleigh model give, respectively, underestimated and overestimated values of the EP relative to the proposed field model. These alternative models suitably describe only a mixture of components with close permittivities.

4. Approximate dependencies of the behavior of the EP of component mixtures with a change in their volume content, constructed on the basis of the generalized Lichtenecker model and the proposed field models, have comparable accuracy with the Odelevsky model for two-component materials and a 2-fold reduced error relative to the layered model for three-component materials.

5. Models with the arrangement of cylindrical volumes in the nodes of a rectangular and parallelogram mesh give the same result when calculating the EP of a macroscopically homogeneous heterogeneous material.

How to cite this article:

Palchykov O.O. Determination of the effective permittivity of a heterogeneous material. *Electrical engineering & electromechanics*, 2020, no.2, pp. 59-63. doi: 10.20998/2074-272X.2020.2.09.

REFERENCES

1. Raju G. G. *Dielectrics in electric fields*. New York, Marcel Dekker, 2003. 578 p.
2. Moulson A.J., Herbert J.M. *Electroceramics: materials, properties, applications*. Chichester, John Wiley & Sons Ltd, 2006. 557 p.
3. Shcheglov N.V. *Sovremennye vidy izolyatsii. Izolyatsiia silovykh kondensatorov* [Modern types of isolation. Power capacitor isolation]. Novosibirsk, NSTU Publ., 2016. 116 p. (Rus).
4. Balagurov B.Ya., Kashin V.A. Electrophysical properties of the Rayleigh three-dimensional model. *Technical Physics*, 2007, vol. 52, no. 2, pp. 216-225. doi: 10.1134/s1063784207020119.
5. Emets Yu.P. Electrical characteristics of three-component dielectric composites with close-packed inclusions. *Journal of Applied Mechanics and Technical Physics*, 2001, vol. 42, iss. 4, pp. 704-713. doi: 10.1023/A:1019272201997.
6. Tolmachev S.T., Yukhymovych D.L. The problem of reducing the hollow circular cylinders with arbitrary grating of periods for regular system. *Technical Electrodynamics*, 2011, no. 2, pp. 11-17. (Rus).
7. He T. Effects of impurities on silicon dioxide dielectric properties. *Advanced Materials Research*, 2014, vol. 1022, pp. 56-59. doi: 10.4028/www.scientific.net/AMR.1022.56.
8. Chen R.J., Zhang Y., Wang B. Numerical simulation study on the cement-based absorbing material. *Advanced Materials Research*, 2013, vol. 853, pp. 169-173. doi: 10.4028/www.scientific.net/AMR.853.169.
9. DSTU 3467-96. *Papir kondensatornyj. Zagal'ni tehnicni umovy*. [DSTU 3467-96. State standard of Ukraine. Capacitor paper. General technical conditions]. Kyiv, Derzhstandart of Ukraine Publ., 1996. 34 p. (Ukr).
10. Stratton J.A. *Electromagnetic theory*. Hoboken, IEEE Press, 2007. 630 p.

Received 17.01.2020

O.O. Palchykov, Candidate of Technical Science, Associate Professor,

Admiral Makarov National University of Shipbuilding,
9, Heroyiv Ukraine Ave, Mykolaiv, Ukraine, 54025,
tel/phone +380 95 8934509;
e-mail: ole2012hulk@gmail.com

V.Ya. Romashko, L.M. Batrak, O.O. Abakumova

REGULATORY CHARACTERISTICS OF THE STEP-DOWN SWITCHING REGULATOR WHICH CHARGES THE BATTERY FROM THE SOLAR BATTERY

Problem. An important element of autonomous power sources, built on the basis of solar batteries, is a battery, operating in a buffer mode. To extend the period of its use, it is necessary to ensure the appropriate modes of its charging and discharging, by regulating the charging and discharge currents. To ensure that maximum power can be transferred to the load in various operating modes, a matching switching regulator is included between the solar battery and the load. In the case of its application, it becomes possible to simultaneously regulate the charging current of the battery. For the most effective regulation of this current, it is necessary to know the regulatory characteristics of the regulator. *Goal.* The aim of the work is to determine and analyze the regulatory characteristics of the switching voltage regulator step-down type, which charges the battery from the solar battery. *Methodology.* Using the theory of switching voltage regulators, a relationship between the output characteristic of the source and the regulatory characteristic of the regulator are established. The graphs of the regulatory characteristics are carried out by the graphoanalytical method. *Results.* The dependence of the output current of the solar battery, from well as the current of the charged battery, on the relative time of the closed state of the key of the switching regulator are analyzed. A technique for constructing the regulatory characteristics of a switching regulator for a given type of output characteristic of a power source and operating voltage of a battery is proposed. For typical output characteristics of the solar battery, graphs of the regulatory characteristics of the switching regulator for various levels of illumination of the solar battery are constructed. When constructing the regulatory characteristics, the possibility of an intermittent current mode in the inductance of the switching regulator is taken into account. *Originality.* The results obtained make it possible to take into account the influence of the internal resistance of the power supply, in particular, substantially nonlinear, on the regulatory characteristics of the switching regulator. *Practical value.* The proposed technique can be used to determine the regulatory characteristics of other types of regulators, the power source of which has a non-linear output characteristic. Using the obtained regulatory characteristics, it is possible to determine the conditions under which maximum power will be transmitted from the solar battery to the battery. These characteristics can be used in the elaboration of solar battery charge controllers. References 8, figures 4.

Key words: switching regulator, regulatory characteristic, solar battery, battery, internal resistance.

Розглянуто підходи до визначення регулювальних характеристик імпульсного регулятора напруги понижувального типу, джерелом живлення якого є сонячна батарея, а навантаженням – акумулятор. Проаналізовано залежність регулювальних характеристик регулятора від типу вихідної характеристики джерела електроживлення з урахуванням нелінійності його внутрішнього опору. Запропоновано методику визначення регулювальної характеристики регулятора для заданого виду вихідної характеристики джерела, з урахуванням можливості виникнення режиму переривчастого струму в його індуктивності. Розроблено рекомендації щодо забезпечення можливості передавання максимально можливої потужності від сонячної батареї до акумулятора. Бібл. 8, рис. 4.

Ключові слова: імпульсний регулятор, регулювальна характеристика, сонячна батарея, акумулятор, внутрішній опір.

Рассмотрены подходы к определению регулировочных характеристик импульсного регулятора напряжения понижающего типа, источником питания которого является солнечная батарея, а нагрузкой – аккумулятор. Проанализирована зависимость регулировочных характеристик регулятора от типа выходной характеристики источника электропитания с учетом нелинейности его внутреннего сопротивления. Предложена методика определения регулировочной характеристики регулятора для заданного вида выходной характеристики источника, с учетом возможности возникновения режима прерывистого тока в его индуктивности. Разработаны рекомендации по обеспечению возможности передачи максимально возможной мощности от солнечной батареи к аккумулятору. Библ. 8, рис. 4.

Ключевые слова: импульсный регулятор, регулировочная характеристика, солнечная батарея, аккумулятор, внутреннее сопротивление.

Introduction. The scope of non-traditional and renewable sources of electricity is expanding every year. The peculiarity of such sources is the dependence of the amount of electricity produced by them on external conditions. Therefore, using similar sources, intermediate storage energy is used. As a storage device, batteries are often used [1, 2]. Rechargeable batteries have a limited life, which depends on the provision of appropriate charging and discharging modes [3, 4]. Battery life can be extended, if not rechargeable, as well as do not permit its deep discharge. In the process of charging the battery, it is desirable to be able to regulate the charge current according to a certain law [1, 2]. To provide these functions special devices – battery charge controllers are used [1, 4]. One of the components of such devices is the

battery charge current regulator. As such a regulator it is advisable to use voltage switching regulators (SRs) [1, 5, 6]. As is known [7] in the case of operation of such a regulator on the battery, it will operate in the mode of regulation of the output current. In connection with this, such a regulator can be used to regulate the charging current of the battery. If necessary, maximum power output from the source can be provided.

The most important characteristic of any regulator is its regulatory characteristic. In the case of power from traditional electricity sources, it is often assumed that the load resistance is much greater than the internal resistance of the source. Therefore, when determining the regulatory characteristics, it is not taken into account, considering it

to be zero [8]. Non-traditional and renewable energy sources often have limited power. Their internal resistance and load resistance are of one order of magnitude. In such cases, the internal resistance of the source will significantly affect the regulatory characteristics and must be taken into account.

In [7] the regulatory characteristics of a SR operation on the battery for cases where the power source is traditional and its internal resistance is close to linear are analyzed. However, the internal resistance of non-traditional and renewable electricity sources is often substantially non-linear. When using SR as a battery charging current regulator, it is important to know its regulatory characteristics.

The goal of the work is to develop a method for determining the regulatory characteristics of the switching voltage regulators for the case where the internal resistance of the power source is substantially nonlinear and the battery is connected at the output. Let's analyze the regulatory characteristics of the SR step-down type for the case when the power source is a solar battery (SB) and the battery is connected at its output.

The method of determining the regulatory characteristics. If the DC step-down SR (Fig. 1) operates in the continuous inductance L current mode, the average values of its input and output voltage are connected by the relation [8]

$$U_{out} = U_{in} t^*, \quad (1)$$

where $t^* = t_{cl} / T$ is the relative time of the lock state of the switch S .

In the case where the internal resistance of the battery is much less than the internal resistance of the power source, it can be assumed that the output voltage of the SR coincides with the voltage of the battery, i.e. $U_{out} = E_a$.

Under these conditions, the input voltage of the SR will depend on the relative time t^*

$$U_{in} = U_{out} / t^* = E_a / t^*. \quad (2)$$

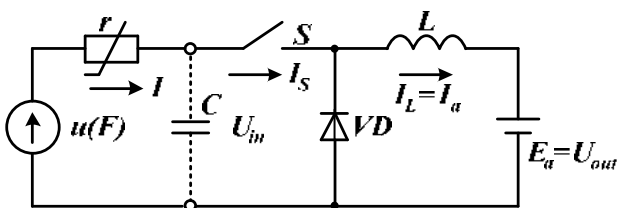


Fig. 1. Step-down switching regulator that charges the battery from the solar battery

If the input voltage source is considered perfect ($U_{in} = E$; $r = 0$), steady-state operation mode of the SR will be possible only at a fixed value t^*

$$t^* = E_a / E, \quad (3)$$

and the output current of the SR is uncertain and depends on the previous mode of operation of the SR.

For $t^* > E_a / E$ the output current will increase indefinitely, and for $t^* < E_a / E$ the SR goes into the mode of intermittent current of the inductance L .

In real power supply sources that have a certain internal resistance r , the output voltage does not remain constant and varies according to their load characteristics.

In such cases, the system will be in equilibrium at a given t^* only at a certain value of the current I consumed from the source.

Linear internal resistance of the source. Let the internal resistance r of the source E be linear. Then its output voltage will be determined by the known relationship [8]

$$U = U_{in} = E - I \cdot r. \quad (4)$$

Therefore, the average value of current consumed from source E can be determined by equating (2) and (4)

$$E - I \cdot r = E_a / t^*,$$

wherefrom

$$I = \frac{E - E_a / t^*}{r} = \frac{E \cdot t^* - E_a}{r \cdot t^*}. \quad (5)$$

If the capacitor C is absent ($C = 0$) at the SR input, a pulsed current will be consumed from the source E , the average value of which at the interval t^* will coincide with the average value at the period of the charging current of the battery $I_a = I_L$. Therefore, in this case, the regulatory characteristic for the battery charging current will look like

$$I_a = \frac{E \cdot t^* - E_a}{r \cdot t^*}. \quad (6)$$

However, if a capacitor C of sufficient capacitance ($C \neq 0$) is placed at the input of the SR, the output current of source I becomes continuous. In such cases, the average values of the currents I and I_a will be related by the relationship [7]

$$I_a = I / t^*. \quad (7)$$

Therefore, in the presence of capacitor C , the regulatory characteristic of the SR (Fig. 1) will look like

$$I_a = \frac{E \cdot t^* - E_a}{r \cdot t^{*2}}. \quad (8)$$

The obtained regulatory characteristics (6) and (8) coincide with the characteristics obtained in [8] otherwise by other considerations.

Nonlinear internal resistance of the source. The solar battery, as a power source, is characterized by a substantially nonlinear internal resistance. Its output voltage will depend on the external conditions as well as on the output current. In the presence of an E_a battery at the output of the SR operation in the of continuous-current mode of the reactor L , the condition of equilibrium must necessarily be satisfied

$$U_{SB} = E_a / t^*. \quad (9)$$

The voltage value of the selected battery E_a will determine the minimum possible voltage at which it is still possible to transfer energy from the SB to the battery

$$U_{SB \min} = E_a. \quad (10)$$

According to (9), the SR in this mode of operation will operate with $t^* = 1$. In case of decrease in $t^* < 1$, the output voltage of the SB must increase, which, under the existing external conditions, may result from a decrease in its output current. Therefore, in the case of a given illumination of the SB F , the maximum current will be taken away from it provided that $t^* = 1$. If $t^* < 1$ decreases, the output voltage of the SB will increase and the output current will decrease. At a certain value of

$t^* = t_{\min}^*$ the output current of the SB becomes zero, and output voltage becomes the idle voltage U_{oc} . Since condition (9) is required for the system under consideration, it is possible to determine a minimum relative switch-locking time t_{\min}^* that will correspond to the SB operation in the idle mode at maximum illumination

$$t_{\min}^* = E_a / U_{oc\max} = E_a^* \quad (11)$$

We draw the voltage of the selected battery E_a^* on the voltage axis of the typical normalized output characteristics of the SB (Fig. 2). This voltage will determine the minimum possible voltage at the output of the SB. According to the presented characteristics, the maximum possible output voltage of the SB corresponds to the voltage of the SB in the idle mode with maximum illumination F_1 . For the selected battery with voltage E_a , from (11) we determine the relative time t_{\min}^* that will correspond to the specified mode of operation. If, now, parallel to the voltage axis, the axis of relative time t^* is drawn and to point on it the obtained values $t_{\max}^* = 1$ corresponding to the voltage $U_{SB\min} = E_a$, and t_{\min}^* , and corresponding to the voltage of the SB $U_{oc\max}$, we obtain the dependence of the output current of the SB on the relative time of the closed state of the switch t^* .

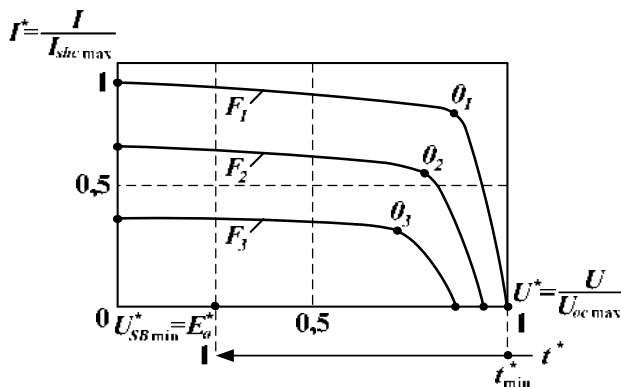


Fig. 2. Typical normalized output characteristics of the SB

It is obvious that in these graphs the directions of growth of the parameters t^* and U^* are opposite.

For greater clarity and ease of use, in Fig. 3 for the case $E_a^* = 0,4$ the same graphs are constructed with the conventional axis direction of the coordinate system.

Figure 3,a presents the dependence of the average value of the SB current on the relative time t^* , and Fig. 3,b shows the regulatory characteristics $I_a^* = f(t^*)$ for the absence ($C = 0$) and the presence ($C \neq 0$) of the capacitor C at the output of the SB.

If the capacitor C is absent ($C = 0$), the SB will operate in the pulsed mode in which the average value of the current of the SB at the interval t^* coincides with the average value of the charging current of the battery I_a at the period T . Therefore, for this mode the regulatory characteristics for the current of the SB I (Fig. 3,a) and the charging current of the battery I_a (Fig. 3,b) will

coincide. However, in this operation mode, the maximum possible amount of electricity cannot be drawn from the SB. Therefore, it is not appropriate to use this mode of operation to charge batteries from the SB.

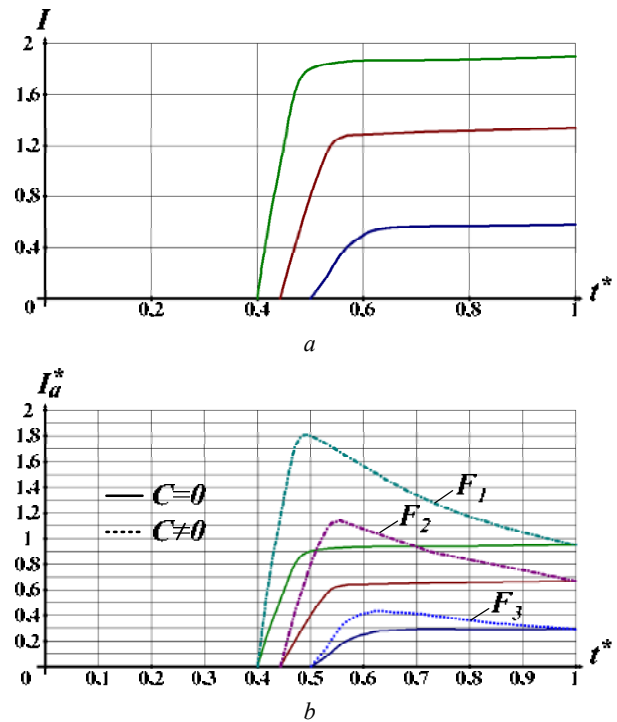


Fig. 3. Regulatory characteristics: a) of the current of the solar battery; b) of the battery charging current

If a capacitor C of sufficiently large capacitance ($C \neq 0$) is placed at the output of the SB, the current of the SB becomes continuous and its average value is related to the average value of the battery charging current by the relationship (7). Under such conditions, the maximum possible power will be transmitted from the SB operating at the maximum power point (MP) to the E_a battery (Fig. 3,b).

If $t^* < t_{MP}^*$ decreases, the charging current of the battery I_a will drop rapidly and at $t^* = t_{\min}^*$ it should be zero. However, in the real world, at a certain value of $t^* = t_{cr}^* > t_{\min}^*$, the SR goes into the intermittent-current reactor L mode, in which with decreasing t^* in the range ($t_{cr}^* \dots 0$), the average charging current of the battery I_a will gradually drop from the initial value $I_{acr}^* = I_a^*(t_{cr}^*)$ to zero. To determine the numerical values of t_{cr}^* , we can use the methodology discussed in [7]. For example, in the case of $E_a^* = 0,4$ at the maximum illumination F_1 , depending on the inductance of the reactor L , the numerical value of t_{cr}^* lies in the range (0.406 ... 0.41).

Figure 4 is a graph of the regulatory characteristic $I_a^* = f(t^*)$ taking into account the possibility of the mode of intermittent current of the reactor L . The regulatory characteristics for other (smaller) levels of illumination F will have the similar character.

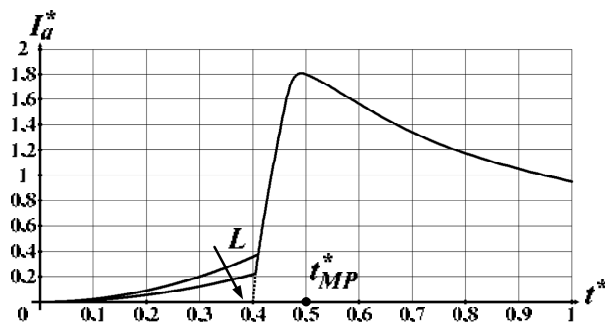


Fig. 4. Regulatory characteristic of the battery charging current taking into account the occurrence of the mode of intermittent current of inductance L

The analysis of the obtained regulatory characteristics shows the following:

1) in case of charging of the battery from the SB with the use of the step-down voltage SR, in order to allow the maximum amount of energy to be drawn from the SB, a capacitor C of a sufficiently large capacitance must be installed at its output;

2) the regulatory characteristics for the battery charging current are substantially nonlinear;

3) with a change in t^* in the range from t_{MP}^* to 0, the charging current of the battery I_a decreases rapidly, and in a large part of this range the SR will operate in the mode of intermittent current of the reactor L ;

4) with a change in t^* in the range from t_{MP}^* to 1, the current I_a will decrease more smoothly. The SR will operate in continuous current mode of the reactor L . However, in this case the range of current regulation is limited.

Conclusions. A developed technique for determining the regulatory characteristics of switching voltage regulators for the case when the power source is a solar battery and the battery connected at the output can be used for other types of renewable and non-traditional sources with nonlinear internal resistance.

REFERENCES

1. Osaretin C.A., Edeko F.O. Design and implementation of a solar charge controller with variable output. *Electrical and electronic engineering*, 2015, vol. 12, no. 2, pp. 40-50.

How to cite this article:

Romashko V.Ya., Batrak L.M., Abakumova O.O. Regulatory characteristics of the step-down switching regulator which charges the battery from the solar battery. *Electrical engineering & electromechanics*, 2020, no.2, pp. 64-67. doi: 10.20998/2074-272X.2020.2.10.

2. Haq I.N., Leksono E., Iqbal M., Sodami F.X.N., Nugraha, Kurniadi D., Yulianto B. Development of battery management system for cell monitoring and protection. *2014 International Conference on Electrical Engineering and Computer Science (ICEECS)*, Kuta, Nov. 2014, pp. 203-208. doi: 10.1109/ICEECS.2014.7045246.

3. Krieger E.M., Arnold C.B. Effects of undercharge and internal loss on the rate dependence of battery charge storage efficiency. *Journal of Power Sources*, 2012, vol. 210, pp. 286-291. doi: 10.1016/j.jpowsour.2012.03.029.

4. Ashiquzzaman M., Afroze N., Hossain J.M., Zobayer U., Hossain M.M. Cost effective solar charge controller using microcontroller. *Canadian Journal on Electrical and Electronics Engineering*, 2011, vol. 2, no. 12, pp. 572-576.

5. Romashko V.Y., Matching device load from the source of electrical energy. *Energy saving. Power engineering. Energy audit*, 2013, no. 8 (114), vol. 1, pp. 67-74.

6. Vieira J.A.B., Mota A.M. Implementation of a stand-alone photovoltaic lighting system with MPPT battery charging and LED current control. *2010 IEEE International Conference on Control Applications*, Sep. 2010, pp. 185-190. doi: 10.1109/CCA.2010.5611257.

7. Romashko V., Batrak L. Regulation characteristics of the step-down switching regulator which operates on a rechargeable battery. *Bulletin of the National Technical University «KhPI» Series: New solutions in modern technologies*, 2019, no. 10 (1335), pp. 30-37. doi: 10.20998/2413-4295.2019.10.04.

8. Goncharov Y.P., Budonny O.V., Morozov V.G., Panasenko M.V., Romashko V.Y., Rudenko V.S. *Peretoviyuvalna technicala. Navchalnyi posibnyk. Ch. 2* [Power conversion equipment. Part 2]. Kharkiv, Folio Publ., 2000. 360 p.

Received 29.11.2019

V.Ya. Romashko¹, Doctor of Technical Science, Professor, L.M. Batrak¹, Candidate of Technical Science, Associate Professor,

O.O. Abakumova¹, Candidate of Technical Science, Associate Professor,

¹ National Technical University of Ukraine «Igor Sikorsky Kyiv Polytechnic Institute»,

37, Prospect Peremohy, Kyiv-56, 03056, Ukraine,

phone +380 44 4068234,

e-mail: volodymyr.romashko@gmail.com,

batrakln@gmail.com, e.o.abakumova@gmail.com

M. Regad, M. Helaimi, R. Taleb, H. Gabbar, A. Othman

OPTIMAL FREQUENCY CONTROL IN MICROGRID SYSTEM USING FRACTIONAL ORDER PID CONTROLLER USING KRILL HERD ALGORITHM

Abstract. This paper investigates the use of fractional order Proportional, Integral and Derivative (FOPID) controllers for the frequency and power regulation in a microgrid power system. The proposed microgrid system composes of renewable energy resources such as solar and wind generators, diesel engine generators as a secondary source to support the principle generators, and along with different energy storage devices like fuel cell, battery and flywheel. Due to the intermittent nature of integrated renewable energy like wind turbine and photovoltaic generators, which depend on the weather conditions and climate change this affects the microgrid stability by considered fluctuation in frequency and power deviations which can be improved using the selected controller. The fractional-order controller has five parameters in comparison with the classical PID controller, and that makes it more flexible and robust against the microgrid perturbation. The Fractional Order PID controller parameters are optimized using a new optimization technique called Krill Herd which selected as a suitable optimization method in comparison with other techniques like Particle Swarm Optimization. The results show better performance of this system using the fractional order PID controller-based Krill Herd algorithm by eliminates the fluctuations in frequency and power deviation in comparison with the classical PID controller. The obtained results are compared with the fractional order PID controller optimized using Particle Swarm Optimization. The proposed system is simulated under nominal conditions and using the disconnecting of storage devices like battery and Flywheel system in order to test the robustness of the proposed methods and the obtained results are compared. References 18, figures 8.

Key words: microgrid, frequency control, FOPID controller, Krill Herd, particle swarm optimization.

Анотація. У статті досліджено використання регуляторів пропорційного, інтегрального та похідного дробового порядку (FOPID) для регулювання частоти та потужності в електромережі. Запропонована мікромережева система складається з поновлюваних джерел енергії, таких як сонячні та вітрогенератори, дизельних генераторів як вторинного джерела для підтримки основних генераторів, а також з різних пристроїв для накопичування енергії, таких як паливна батарея, акумулятор і маховик. Через переривчасту природу інтегрованої відновлювальної енергії, наприклад, вітрогенераторів та фотоелектричних генераторів, які залежать від погодних умов та зміни клімату, це впливає на стабільність мікромережі, враховуючи коливання частоти та відхилення потужності, які можна поліпшити за допомогою вибраного контролера. Контролер дробового порядку має п'ять параметрів порівняно з класичним PID-контролером, що робить його більш гнучким та надійним щодо збурень мікромережі. Параметри PID-контролера дробового порядку оптимізовані за допомогою нової методики оптимізації під назвою «зграя криля», яка обрана як підходящий метод оптимізації порівняно з іншими методами, такими як оптимізація методом рою частинок. Результати показують кращі показники роботи цієї системи за допомогою алгоритму «зграя криля», заснованого на PID-контролері дробового порядку, виключаючи коливання частоти та відхилення потужності порівняно з класичним PID-контролером. Отримані результати порівнюються з PID-контролером дробового порядку, оптимізованим за допомогою оптимізації методом рою частинок. Запропонована система моделюється в номінальному режимі роботи та використовує відключення накопичувальних пристроїв, таких як акумулятор та маховик, щоб перевірити надійність запропонованих методів та порівняти отримані результати. Бібл. 18, рис. 8.

Ключові слова: мікромережа, регулювання частоти, FOPID-контролер, метод «зграя криля», оптимізація методом рою частинок.

Introduction. The increase in energy demand, the technologies evolution and the depletion of fossil fuel lead towards the use of renewable energy generation. As energy production moving to the renewable, photovoltaic system and wind generators appear to be the fastest technologies in the power system. This attention for saving climate against greenhouse gas emission has made researchers study various non-polling sources such as solar and wind system which are considered the most used renewable energy generation [1]. All this has given rise to the integration of renewable energy resources like wind and solar with distributed energy resources and energy storage systems such as batteries, flywheels and ultra-capacitor [2]. The intermittent nature of solar radiations, and wind speed, is resulted in the dependence of these resources on the weather conditions at any time [3]. This can result in an unbalance between electrical load and generation and

sometimes result in unstable operation of the microgrid. This unbalance improved by the use of storage energy devices and conventional sources in hybrid power system based renewable energy generation. These storage systems store the surplus power from the renewable energy sources overly the demanded power in order to rid it later when the generated power is insufficient to feed the load demand. Many kinds of research investigate to study of power generation system based renewable generation systems such as wind and thermal solar in a hybrid system with a storage system and diesel generator [4, 5]. The importance of storage energy systems such as batteries, aqua electrolyser, fuel cell, ultracapacitor, and super magnetic energy storage (SMES) lead to analysis and control of various hybrid system configurations as in [6-9]. However, the use of conventional sources such as diesel generator and

energy storage devices control the mismatches in frequency and power deviations and assure the operation of the hybrid energy system in isolated areas independently of the main grid. These fluctuations in microgrid power and frequency must be controlled due to the intermittent and stochastic nature of renewable energy resources.

The control of frequency and power fluctuation is a big challenge faced by the use of the hybrid system over the wide domain. Even though many studies interest the control of hybrid energy systems using deferent strategies control among this PID controller, Fuzzy logic controller, and fractional PID controller etc. These studies show the high robustness of these proposed control schemes and enhance the performance of the hybrid energy system [6]. The fractional-order controller is widely considered the best controller for frequency and power fluctuations in the hybrid power system, in some cases, the FOPID and PID classic are integrated into hybridizing with other controllers like fuzzy logic which can give better performance of the system but with complexity in design and implementation.

The fractional controller is defined as the generality of the classical PID controller with the addition of two parameters in order to give more flexibility to the robustness of this controller. It has found suitable applications in microgrid frequency and hybrid energy systems [5].

In this paper, the fractional PID controller is used to control the frequency and power deviations for its robustness shown by the previous studies as in [8]. Many evolutionary optimization methods have been employed for tuning the controller parameters and given more improvement to the control strategies. Among these methods are widely used the Evolutionary Algorithm (EA), Genetic Algorithm (GA), and Particle Swarm Optimization (PSO) and so one [3, 7, 17]. Recently a new optimization technique called Krill Herd (KH) algorithm has been invented based on the behaviour of Krill in the research of food [13]. This technique is used to optimize the PID controller parameters in [16]. In our study, the Krill Herd is employed to optimize the two proposed controller and compared with PSO. The rest of this paper is summarized as fellow: the microgrid model is presented in section 2; the controller scheme is presented in section 3; in section 4 optimization technique and objective function are reported; in section 5 the results are analyzed and compared. This paper is ended by a conclusion in section 6 followed by a reference.

Microgrid concept. The proposed microgrid consists of two renewable energy resources like wind turbine generators and photovoltaic systems with diesel engine generator and fuel cell system as secondary sources along with energy storage systems like batteries and flywheel for store the surplus of generated power in order to release them later [1]. For small-signal analysis, the wind turbine generator (WTG), photovoltaic (PV), fuel cell (FC), and diesel energy generator (DEG) are modeled by a transfer function in the first order as showed in Fig. 1 [5].

Modeling of different generation components. For small-signal analysis, the dynamics of the WTG, PV, FC, and DEG can be modeled by the first-order transfer function. The model has been considered for analysis and demonstration of frequency behaviour in different cases [1]

$$G_{WTG} = \frac{K_{WTG}}{1+T_{WTG}} = \frac{\Delta P_{WTG}}{\Delta P_W}; \quad (1)$$

$$G_{PV} = \frac{K_{PV}}{1+T_{PV}} = \frac{\Delta P_{PV}}{\Delta \phi}; \quad (2)$$

$$G_{FC} = \frac{K_{FC}}{1+T_{FC}} = \frac{\Delta P_{FC}}{\Delta u}; \quad (3)$$

$$G_{DEG} = \frac{K_{DEG}}{1+T_{DEG}} = \frac{\Delta P_{DEG}}{\Delta u}. \quad (4)$$

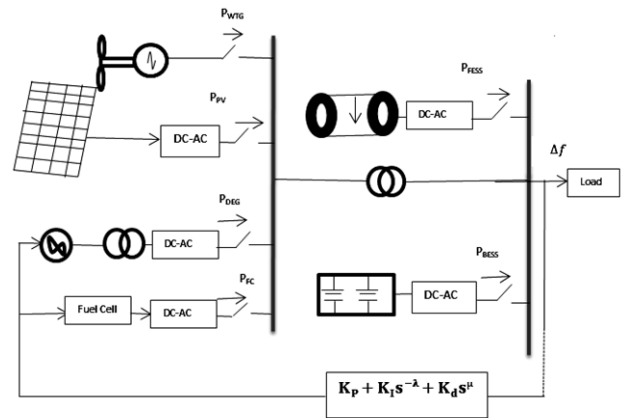


Fig. 1. Schematic of the hybrid system with energy storage and regeneration compounds

Models of energy storage systems. Energy storage plays an important role in the hybrid energy system in order to absorb the surplus power from renewable energy sources and release to loads if a deficit amount of power. The battery energy storage system (BESS) is slower to charge and discharge; its time constant is limited. On the other hand flywheel energy storage system (FESS) stores mechanical energy in a rotating flywheel rotor and retrieves it later as an electrical output. It can supply high power in a short time. The transfer functions of the BESS and FESS can be presented by a first-order transfer function as given next [1, 5, 8]

$$G_{BESS} = \frac{K_{BESS}}{1+T_{BESS}}; \quad (5)$$

$$G_{FESS} = \frac{K_{FESS}}{1+T_{FESS}}; \quad (6)$$

where K_{BESS} and K_{FESS} are the gain constants, T_{BESS} and T_{FESS} are time constants, of BESS and FESS respectively.

Power generation characteristics with loads power. Small stochastic power fluctuation and large deterministic drift reckoning for solar power generation, wind power generation and load demand power can be modeled as [5]

$$P = \left(\frac{\phi \cdot \eta \cdot \sqrt{\beta} \cdot (1 - G(s)) + \beta}{\beta} \right) \cdot \Gamma = \Gamma \cdot X, \quad (7)$$

where ϕ is the stochastic component of the power, P represents the wind or solar and load powers, β presents the mean value of the power, η is a constant normalizes the generated or demand powers (X) constant to correspondence per unit (p.u.) level, and Γ is time-dependent switching signal with a gain causes sudden fluctuation of the average value for stochastic power [5, 8]. For the wind power generation the parameters of (7) are

$$\phi \sim U(1,1), \eta = 0.8, \beta = 10, G(s) = \frac{1}{10^4 + 1}$$

and

$$\Gamma = 0.24 \cdot h(t) - 0.04 \cdot h(t - 140), \quad (8)$$

where $h(t)$ is the Heaviside step function.

For the solar power generation the parameters of (7) are

$$\phi \sim U(1,1), \eta = 0.9, \beta = 10, G(s) = \frac{1}{10^4 + 1}$$

and

$$\Gamma = 0.05 \cdot h(t) - 0.02 \cdot h(t - 180), \quad (9)$$

For the demand load the parameters of (7) are

$$\phi \sim U(1,1), \eta = 0.8, \beta = 10, G(s) = \frac{1}{300s + 1} + \frac{1}{1800s + 1}$$

and

$$\Gamma = \frac{1}{X} \left[\begin{array}{l} 0.9 \cdot h(t) + 0.03 \cdot h(t - 110) + 0.03 \cdot h(t - 130) + \\ + 0.03 \cdot h(t - 150) - 0.15 \cdot h(t - 170) + \\ + 0.1 \cdot h(t - 190) \end{array} \right] + 0.02h(t). \quad (10)$$

Fractional order PID controller. PID controller is a specific control loop feedback technic generally used in the industrial control system [6]. The PID controller consists to correct the error between a measured process variable and the desired set point. The $PI^\lambda D^\mu$ controller is defined as a generalization of classical PID controller, Since these fractional controllers have two parameters more than the conventional PID controller: the order of fractional integration λ and that of fractional derivative μ , two more specifications can be met, thus can enhance the performance of the system and could lead to more robust control performances, more adequate modeling and adds more flexibility to controller design. We can control our real-world processes more accurately [7]. The FOPID controller has three parameters similar to the PID controller along with the two additional parameters namely; the integral order λ , and the differential order μ . The transfer function of FOPID controller in Laplace domain is given as presented in Fig. 2 [8, 12]. At Fig. 2 $y(t)$ is controller output, k_p is proportional constant gain, k_i is integration constant gain, k_d is derivative constant gain, λ is order of integration, μ is the order of differentiators.

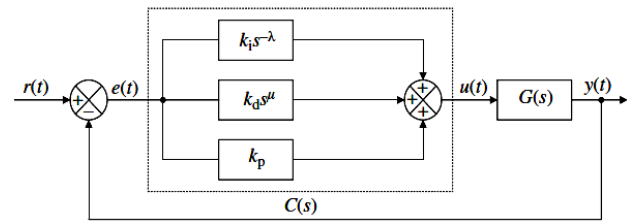


Fig. 2. Fractional order PID controller

When taking $\lambda = \mu = 1$ the result is the classical PID controller (Fig. 3).

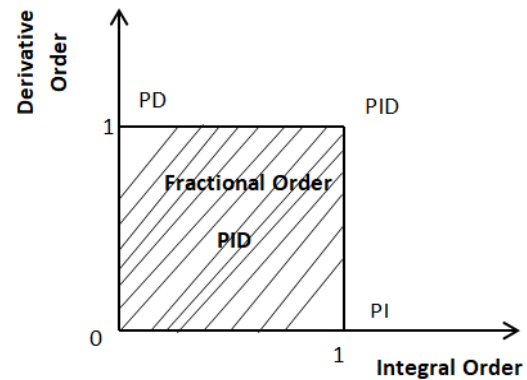


Fig. 3. Expanding from Point to Plane

Due to the presence of stochastic terms in generation and load, the optimization of the parameters controller leads to eliminate the frequency and power deviation.

We will design fractional-order PID controllers using the Krill Herd and display the advantages of the fractional-order controllers.

Objective function and optimization of FOPID controller. For the effective functioning of the hybrid system, the fractional PID controller parameters need to be determined. For this problem, the objective function in (11) is used to minimize the frequency deviation (as well as the control signal ISE (Integral of Squared Error) is used as a fitness function for the optimization of controller parameters). The fitness function has been defined as integration between the T_{min} and T_{max} simulation period, using the sum of square frequency deviation ΔF and the deviation of the control signal (Δu) [5]

$$J = \int_{T_{min}}^{T_{max}} \left[w \cdot \Delta F^2 + \left(\frac{1-w}{K_n} \right) \cdot \Delta u^2 \right] dt, \quad (11)$$

where w represents the Integral of Square Error (ISE) of frequency deviation and the Integral of Squared Deviation of Controller Output (ISDCO).

Overview of Krill Herd Algorithm. KH is a novel optimization technique for resolving the optimization problem [13]. This technique is inspired by the simulation of the herding of Krill swarm in the response of specific biological environment processes. It is characterized by three main actions described as follows [14, 15]:

1. Movement induced by other krill;
2. Foraging action;
3. Random diffusion.

In KH, the Lag radian model is used in d -dimensional decision space as shown in [16]

$$\frac{dX_i}{dt} = N_i + F_i + D_i, \quad (12)$$

where N_i is the motion induced by other Krill; F_i is the foraging motion, and D_i is the physical diffusion of the i th krill.

Krill Herd algorithm [16] is next:

Begin
 Step 1: initialization.
 Step 2: fitness evaluation.
 Step 3: While the termination criteria.
 Step 4: end while
 Step 5: post-processing the results and visualization
 End

Overview of Particle Swarm Optimization. Many problems have not an exact solution that gives the results in a reasonable time. For overcoming these problems some metaheuristics methods offer an approached solution after much iteration are recently proposed. Among these methods, the PSO algorithm has a general principle to be applied in many fields of optimization problems. PSO is a stochastic optimization algorithm developed by Eberhart and Kennedy, inspired by the social behaviour and fish schooling of bird flocking. Each particle in the swarm is a different possible set of the unknown parameters of the objective function to be optimized. The swarm consists of N particles moving around in a D -dimensional search space. Each particle is initialized with a random position and a random velocity [17, 18]. The new velocity can be calculated by the fellow formula.

$$V_{i+1} = w \cdot V_i + C_1 \cdot r_1 \cdot (P_{best} - X_{ik}) + C_2 \cdot r_2 \cdot (G_{best} - X_i), \quad (13)$$

$$X_{i+1} = X_i + V_{i+1}, \quad (14)$$

where V_i is the component in the dimension of the particle velocity in iteration, X_i is the component in the dimension of the particle position in iteration, C_1 and C_2 are constant weight factors, P_{best} is the best position achieved so far by particle, G_{best} is the best position found by the neighbours of particle, and are random factors in between 0 and 1 interval, and w is inertia weight which is started from a positive initial value (w_0) and decreases during the iterations by

$$W_{k+1} = \beta \cdot W_k.$$

The algorithms of PSO can be described as follows:

Step 1: Initialize a population of particles with random positions and velocities on D -dimensions in the problem space.

Step 2. Evaluation of desired optimization fitness function in D variables for each particle.

Step 3. Comparison of particle's fitness evaluated with its best previous position. If the current value is better, then set the best previous position equal to the current value, and p_i equals to the current location x_i in D dimensional space.

Step 4. Identifying the particle in the neighbourhood with the best fitness so far, and assign its index to the variable g .

Step 5. Change velocity and position of the particle according to Equation (13) and (14).

Step 6. Return to step 2 until a criterion is met or end of iterations.

Results and discussions. The proposed configuration of the microgrid system is executed using MATLAB/Simulink Sawford under different operating conditions in various power scales (Fig. 4). Per unit is considered as the principal unit of all power values.

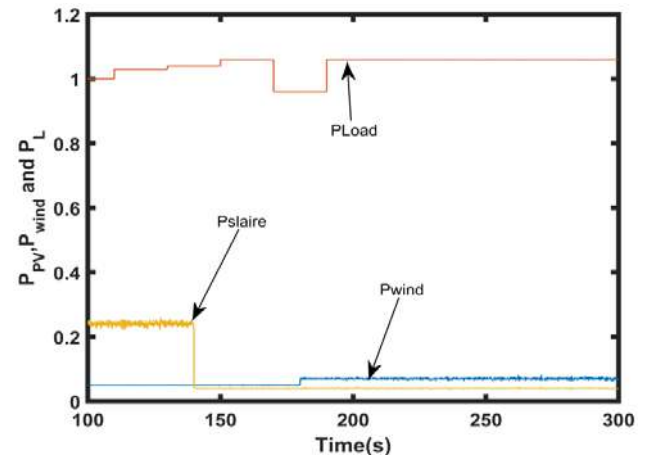


Fig. 4. Power generation from wind and solar system with demand load

Robustness of FOPID using KH and PSO under nominal conditions. In this subsection, the system is simulated under the nominal condition with the application of FOPID optimized using PSO and KH. A comparison between the two optimization techniques is represented on Fig. 5, 6.

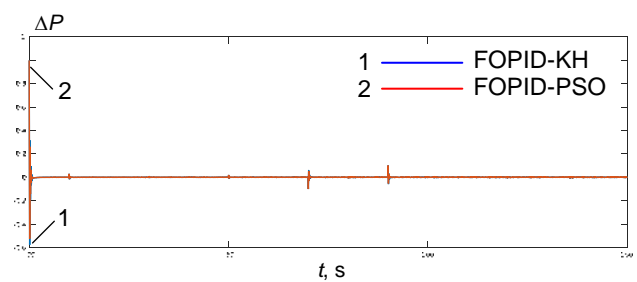
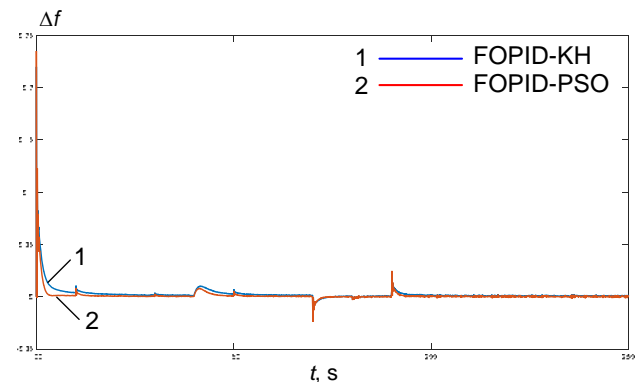


Fig. 5. Frequency and power deviation using best FOPID based KH and PSO

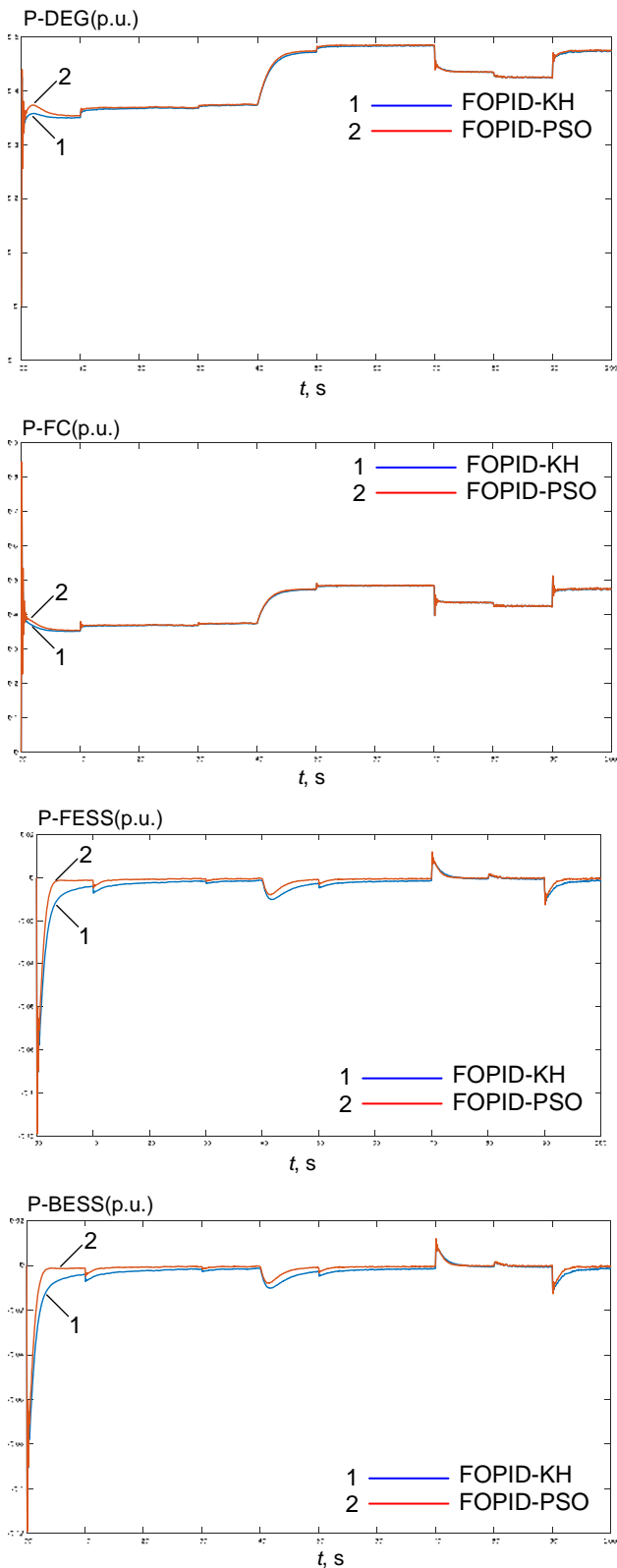


Fig. 6. The output power of different component of Microgrid using best FOPID

Robustness against Disconnecting of BESS and FESS using KH based FOPID. The system is simulated with and without FESS using the FOPID controller which optimized by KH. The obtained results are compared and shown the marked effect of the disconnecting flywheel energy storage system that required adequate control. This control necessity is achieved by applying FOPID. Fig.7

shows the frequency response of the system under FESS and BESS disconnecting.

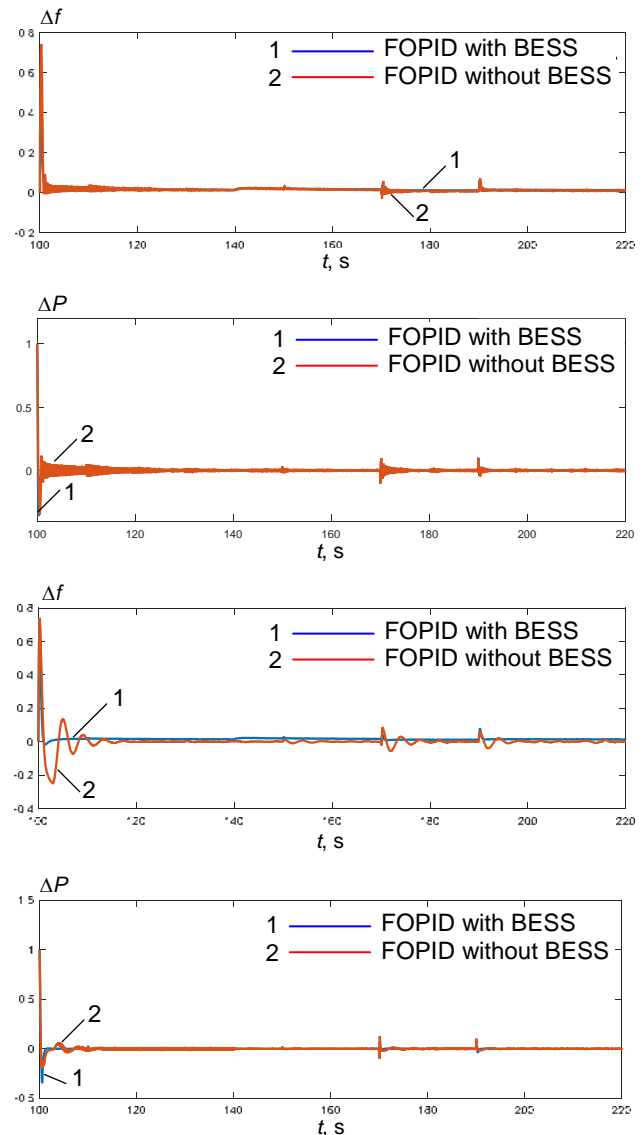


Fig. 7. Impact of BESS and FESS absence using KH with best FOPID

Comparison of PID and FOPID. The proposed system is simulated under nominal conditions using FOPID and PD controllers based on Krill Herd. A comparison is achieved between the two controllers and the results are shown in Fig. 8.

Discussions. The proposed controllers are tuned using Krill Herd and Particle Swarm Optimization in object to testing the system robustness. The system is simulated without the BESS, FESS, and DEG respectively and the effect of these components is tested using FOPID based KH and PSO. Then the obtained results are compared. The previous figures show different results. The result of the comparison of FOPID and PID is shown using KH running for 100 iterations. Though, the optimization method is a convenient technique that can be applied in this type of optimization issue.

Fig. 8 displays the obtained results of frequency and power response for FOPID and PID parameters. From these figures it can be easily observed that frequency

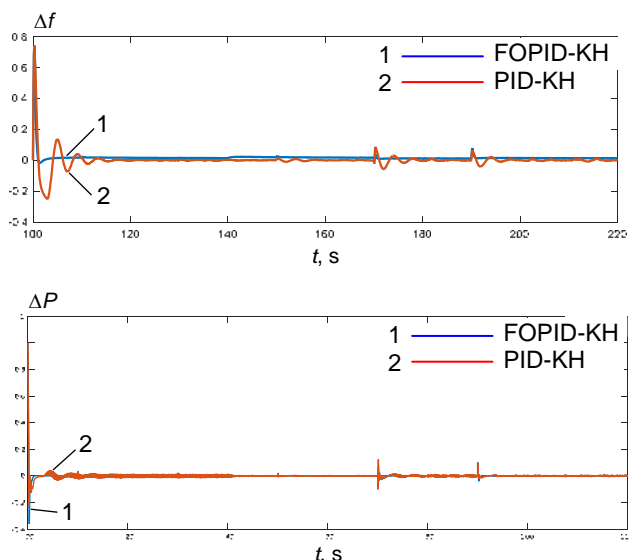


Fig. 8. Frequency and power variations using KH based the best FOPID and PID

deviation reaches zero in the face of disturbances in loads and generation units. These sudden changes in power generations and loads demand to have an important effect on frequency and power variations. The main objective of this letter was to analyze and improve the frequency control. A remarkable better performance of the system can be reached using FOPID controllers based on Krill Herd in comparison with FOPID based PSO. The obtained results present that KH-FOPID performed better than KH-PID due to its low-frequency variation and rapid transient variation. It is also shown that the frequency and power fluctuations in microgrid using FOPID-KH are small than with FOPID- PSO.

Conclusions.

This paper addresses the application of a fractional-order PID controller for microgrid frequency control using Krill Herd to eliminate the influence of the mismatches between the generation and loads which causes high fluctuation of frequency and power in microgrid system based on renewable energy generation. Various Microgrid components are modeled by a transfer function in the first order to simplify the simulation process. The simulation results showed that the Krill Herd based FOPID controller scheme is favourable to send away the frequency and power deviations under perturbation operation conditions in comparison with PSO based FOPID controller because the frequency deviation is small with FOPID-KH (around 0.218) than for FOPID-PSO (around 0.235) and the power deviation varies from 1 p.u to -0.5 p.u with FOPID-KH and from 1 p.u to -0.6 p.u with FOPID-PSO which signify the best performances with FOPID-KH. Furthermore, the proposed controller is suitable to control the perturbation string along with renewable energy sources intermittences and sudden variation in power load. The generated power from DEG is enhanced using the FOPID-KH than by FOPID-PSO as shown (P-DEG equal to 0.41 p.u for FOPID-KH and 0.426 p.u for FOPID-PSO). From the presented results it can be easily observed that the Krill

Herd is considered as the best optimization technique in terms of rapid response, good robustness to tuning the controller parameters and to improve the proposed system performance. In conclusion, the selected control strategy based optimization technique gives high suitability in microgrid frequency control.

REFERENCES

1. Lee D.-J., Wang L. Small-Signal Stability Analysis of an Autonomous Hybrid Renewable Energy Power Generation/Energy Storage System Part I: Time-Domain Simulations. *IEEE Transactions on Energy Conversion*, 2008, vol. 23, no. 1, pp. 311-320. doi: 10.1109/tec.2007.914309.
2. De Souza Ribeiro L.A., Saavedra O.R., De Lima S.L., De Matos J. Isolated Micro-Grids With Renewable Hybrid Generation: The Case of Lençóis Island. *IEEE Transactions on Sustainable Energy*, 2011, vol. 2, no. 1, pp. 1-11. doi: 10.1109/tste.2010.2073723.
3. Kouba N.E.L.Y., Mena M., Hasni M., Boussahoua B., Boudour M. Automatic generation control in interconnected power System with integration of wind power generation using PID based on particle swarm optimization. *International Conference on Renewable Energies and Power Quality (ICREPO'14)*, Cordoba (Spain), 8-10 April 2014.
4. Senjyu T., Nakaji T., Uezato K., Funabashi T. A hybrid power system using alternative energy facilities in isolated island. *IEEE Transactions on Energy Conversion*, 2005, vol. 20, no. 2, pp. 406-414. doi: 10.1109/tec.2004.837275.
5. Pan I., Das S. Kriging based surrogate modeling for fractional order control of microgrids. *IEEE Transactions on Smart Grid*, 2015, vol. 6, no. 1, pp. 36-44. doi: 10.1109/tsg.2014.2336771.
6. Pan I., Das S. Fractional order fuzzy control of hybrid power system with renewable generation using chaotic PSO. *ISA Transactions*, 2016, vol. 62, pp. 19-29. doi: 10.1016/j.isatra.2015.03.003.
7. Das D.Ch., Roy A.K., Sinha N. Genetic algorithm based PI controller for frequency control of an autonomous hybrid generation system. *Proceedings of the International MultiConference of Engineers and Computer Scientists (IMECS 2011)*, 2011, vol. 2, 16-18 March, 2011, Hong Kong.
8. Regad M., Helaimi M., Taleb R., Gabbar H.A., Othman A.M. Fractional Order PID Control of Hybrid Power System with Renewable Generation Using Genetic Algorithm. *2019 IEEE 7th International Conference on Smart Energy Grid Engineering (SEGE)*, Aug. 2019, Oshawa, ON, Canada, pp. 139-144. doi: 10.1109/sege.2019.8859970.
9. Pandey S.K., Mohanty S.R., Kishor N., Catalão J.P.S. Frequency regulation in hybrid power systems using particle swarm optimization and linear matrix inequalities based robust controller design. *International Journal of Electrical Power & Energy Systems*, 2014, vol. 63, pp. 887-900. doi: 10.1016/j.ijepes.2014.06.062.
10. Regad M., Helaimi M., Taleb R., Toubal Maamar A.E. Optimum Synthesis of the PID Controller Parameters for Frequency Control in Microgrid Based Renewable Generations. *Smart Energy Empowerment in Smart and Resilient Cities*, 2019, pp. 546-556. doi: 10.1007/978-3-030-37207-1_58.
11. Wang L., Lee D.-J., Lee W.-J., Chen Z. Analysis of a novel autonomous marine hybrid power generation/energy storage system with a high-voltage direct current link. *Journal of Power Sources*, 2008, vol. 185, no. 2, pp. 1284-1292. doi: 10.1016/j.jpowsour.2008.08.037.
12. Biswas A., Das S., Abraham A., Dasgupta S. Design of fractional-order $PI\lambda D\mu$ controllers with an improved differential

evolution. *Engineering Applications of Artificial Intelligence*, 2009, vol. 22, no. 2, pp. 343-350. doi: **10.1016/j.engappai.2008.06.003**.

13. Gandomi A.H., Alavi A.H. Krill herd: A new bio-inspired optimization algorithm. *Communications in Nonlinear Science and Numerical Simulation*, 2012, vol. 17, no. 12, pp. 4831-4845. doi: **10.1016/j.cnsns.2012.05.010**.

14. Gandomi A.H., Talatahari S., Tadbiri F., Alavi A.H. Krill herd algorithm for optimum design of truss structures. *International Journal of Bio-Inspired Computation*, 2013, vol. 5, no. 5, pp. 281-288. doi: **10.1504/ijbic.2013.057191**.

15. Yaghoobi S., Mojallali H. Tuning of a PID controller using improved chaotic Krill Herd algorithm. *Optik*, 2016, vol. 127, no. 11, pp. 4803-4807. doi: **10.1016/j.ijleo.2016.01.055**.

16. Alikhani A., Suratgar A.A., Nouri K., Nouredanesh M., Salimi S. Optimal PID tuning based on Krill Herd optimization algorithm. *The 3rd International Conference on Control, Instrumentation, and Automation*, Dec. 2013. doi: **10.1109/icciautom.2013.6912801**.

17. Regad M., Helaimi M., Taleb R., Othman A.M., Gabbar H.A. Frequency Control in Microgrid Power System with Renewable Power Generation Using PID Controller Based on Particle Swarm Optimization. *Smart Energy Empowerment in Smart and Resilient Cities*, 2019, pp. 3-13. doi: **10.1007/978-3-030-37207-1_1**.

18. Iruthayarajan M.W., Baskar S. Evolutionary algorithms based design of multivariable PID controller. *Expert Systems with Applications*, 2009, vol. 36, no. 5, pp. 9159-9167. doi: **10.1016/j.eswa.2008.12.033**.

Mohamed Regad¹, PhD student,
 M'hamed Helaimi¹, Doctor of Electrical Engineering,
 Rachid Taleb¹, Professor,
 Hossam Gabbar², Professor,
 Ahmed Othman³, Doctor of Electrical Engineering,
¹Electrical Engineering Department,
 Laboratoire Génie Electrique et Energies Renouvelables (LGEER),
 Hassiba Benbouali University, Chlef, Algeria,
 e-mail: mohd.regad@gmail.com,
 m.helaimi@univ-chlef.dz, rac.taleb@gmail.com
²Faculty of Energy Systems and Nuclear Science,
 University of Ontario Institute of Technology (UOIT),
 Oshawa, Canada,
 e-mail: hossam.Gaber@uoit.ca
³Electrical Power and Machine Department,
 Faculty of Engineering,
 Zagazig University, Zagazig, Egypt,
 e-mail: ahmed_othman80@yahoo.com

Received 22.01.2020

How to cite this article:

Regad M., Helaimi M., Taleb R., Gabbar H., Othman A. Optimal frequency control in microgrid system using fractional order PID controller using Krill Herd algorithm. *Electrical engineering & electromechanics*, 2020, no.2, pp. 68-74. doi: **10.20998/2074-272X.2020.2.11**.

Матеріали приймаються за адресою:

Кафедра "Електричні апарати", НТУ "ХПИ", вул. Кирпичова, 21, м. Харків, 61002, Україна

Електронні варіанти матеріалів по e-mail: a.m.grechko@gmail.com

Довідки за телефонами: +38 050 653 49 82 Клименко Борис Володимирович

+38 067 359 46 96 Гречко Олександр Михайлович

Передплатний індекс: 01216